CERN-SPSC-2007-035
SPSC-M-760
26.11.2007

NA62/P-326 Status Report

Birmingham, CERN, Dubna, Fairfax, Ferrara, Florence, Frascati, Mainz, Merced, Moscow, Naples, Perugia, Protvino, Pisa, Rome I, Rome II, Saclay, San Luis Potosí, Stanford, Sofia, Triumf, Turin

Contents

1 Executive Summary

After describing the status of the measurement of the ratio $\Gamma(K^{\pm}_{e2})/\Gamma(K^{\pm}_{\mu 2})$ in the light of the data taking performed at the SPS in 2007, we summarise the steps taken to optimise the $K^+ \to \pi^+\nu\bar{\nu}$ experiment and we report on the R&D. The updated base-line design of the experiment comprises the following principal changes with respect to the layout described in the Proposal, P-326:

1. The 75 GeV/c beam layout is modified to satisfy the conditions needed to suppress the positron component in the beam. This is achieved by the introduction of a (0.5 - 1) X_0 radiator of tungsten at a double focus in the front-end achromat.

2. The beam spectrometer and tracking system ('Gigatracker') is constituted by 3 similar stations, composed of silicon-pixel arrays, located in a rematched beam spectrometer stage.

3. A 'Single Spectrometer' configuration is adopted for the detection and measurement of charged decay products upstream of the RICH counter. It comprises 4 chambers of straw tubes arranged around a single, existing MNP33 spectrometer magnet. As a consequence, only one Intermediate Ring Calorimeter (IRC) is used to cover the dead-space around the central hole in the LKR calorimeter.

4. The 12 Large Angle Photon Veto stations (LAV) surrounding the decay and detector sections of the layout are constituted by radial arrays of lead-glass blocks, arranged in overlapping layers. These lead-glass blocks with their PMs are recuperated fom the OPAL 'Barrel' detector.

5. Hadron-muon identification downstream of the LKR calorimeter is provided by a separate-function sequence of: a Hadron Calorimeter (HAC) + iron wall + x-, y-segmented Muon Detector, followed by an existing IHEP MSP-12A dipole magnet to deflect the beam to the side of the final Small Angle Calorimeter (SAC).

6. The Multigap Glass RPC hodoscope is dropped from the layout as the timing of the pion from the kaon decay is performed by the RICH counter.

The principle of the experiment remains unchanged and the improvements to the layout are motivated by an optimisation of the resources allocation and by the results obtained during the R&D phase of 2006-2007. The beam and detector sections are updated according to the progress made over the past two years of R&D. Firm baseline choices were made where necessary and they are described in detail in this document. Preliminary estimations of the IT resources required for the $K^+ \to \pi^+\nu\bar{\nu}$ experiment were made. Possibilities to study pion rare decays were also investigated [1].
Concerning beam time in 2008, we wish to request two three-week sessions of P0 proton beam in order to:

- Collect data for systematic checks of $\Gamma(K^{\pm}_{e2})/\Gamma(K^{\pm}_{\mu 2})$ if needed.
- Measure the angular resolution of the RICH prototype equipped with 400 PMTs.
- Complete the investigations with the STRAW prototypes.
- Test a module of Large Angle Veto (LAV) and muon detector built according to the final specification.

2 Measurement of the ratio $\Gamma(K^{\pm}_{e2})/\Gamma(K^{\pm}_{\mu 2})$

2.1 Motivation

Despite the poor theoretical control on the meson decay constants, ratios of leptonic decay rates of pseudoscalar mesons, such as $R_K \equiv \Gamma(K_{e2})/\Gamma(K_{\mu 2})$, can be predicted with high accuracy within a given model, and have been traditionally (since the observation of the $\pi^+ \to e^+\nu$ decay at CERN in 1958) considered as tests of the $V-A$ structure of weak interactions and of lepton universality. By convention, the definition of R_K includes the inner bremsstrahlung (IB) part of the radiative $K_{\ell 2\gamma}$ processes, while the structure dependent

(SD) $K_{\ell 2\gamma}$ processes are considered as background. The SM prediction [2] is

$$R_K^{\rm SM} = \left(\frac{m_e}{m_\mu}\right)^2 \left(\frac{m_K^2 - m_e^2}{m_K^2 - m_\mu^2}\right)^2 (1 + \delta R_{\rm QED}) = (2.477 \pm 0.001) \times 10^{-5}, \quad (1)$$

where $\delta R_{\rm QED} = -3.6\%$ is a correction due to the $K_{\ell 2\gamma}(IB)$ and virtual photon processes.
A recent theoretical study [3] points out that lepton flavour violating effects arising in SUSY extensions of the SM can induce sizable violations of the $\mu - e$ universality, shifting R_K by a relative amount that can be as large as a few %, without contradicting any other presently known experimental constraints. It is the helicity suppression of the SM contribution that makes the K_{e2} decay rate sensitive to New physics.
The 2006 world average [4] determined by experiments performed in the 1970s is

$$R_K^{2006} = (2.45 \pm 0.11) \times 10^{-5}, \quad (2)$$

which, in terms of precision ($\delta R_K/R_K = 4.5\%$), is far from the level allowing SM tests. Consideration of the recent preliminary results from the NA48/2 [5, 6] and KLOE [7] collaborations leads to a world average of

$$R_K^{2007} = (2.433 \pm 0.036) \times 10^{-5}, \quad (3)$$

which has a precision of $\delta R_K/R_K = 1.5\%$.
The goal of the NA62 2007 physics run is a measurement reaching an accuracy better than $\delta R_K/R_K = 0.5\%$ in order to provide a stringent SM test. This requires 1) collection of a large data sample of the order of 10^5 K_{e2} candidates with sufficiently small background contamination (in our case below 10%); 2) data taking strategy allowing control over the systematic effects, in particular those due to background subtraction.

2.2 Data taking

The NA48 beamline and apparatus were used during the 2007 K_{e2} run. The following subdetectors located downstream a vacuum decay volume are required for the R_K measurement.

- A magnetic spectrometer composed of four drift chambers (DCHs) and a spectrometric magnet (MNP33). Each chamber is composed of eight planes of sense wires arranged in four pairs of staggered planes (so called "views") oriented horizontally, vertically, and along each of the two orthogonal 45° directions.

- A plastic scintillator hodoscope (HOD) used to produce fast trigger signals. The HOD consists of a plane of vertical and a plane of horizontal strip-shaped counters, each plane comprising 64 counters arranged in four quadrants.

- A liquid krypton (LKR) electromagnetic calorimeter, which is an almost homogeneous ionisation chamber with an active volume of 7 m^3 of krypton, $27X_0$ deep, segmented transversally into 13,248 projective cells ($\approx$2$\times$2 cm^2 each) by a system of ribbon electrodes, and with no longitudinal segmentation.

A beam pipe traversing the centres of the detectors allows the undecayed beam particles and the muon halo from decays of beam pions to continue their path in vacuum.
The 2007 running conditions were optimized for the K_{e2} measurement using the experience of the NA48/2 2003–04 data analysis, and taking into account that the two principal $K_{\ell 2}$ selection criteria applied to the 1-track events are the following.

- The $K_{\ell 2}$ candidates ($\ell = e, \mu$) are kinematically identified requiring that the reconstructed missing mass squared $M^2_{\rm miss} = (P_K - P_\ell)^2$ (where P_K and P_ℓ are kaon and lepton 4-momenta) is compatible with zero within its uncertainty, as expected for a neutrino. This imposes requirements to the kaon beams discussed in Section 2.2.1.

- Electron identification is used to select the K_{e2} candidates: $0.95 < E/p < 1.05$, where E is the energy deposited by the track in the LKR calorimeter, and p is its momentum measured by the spectrometer. Similarly, muon identification ($E/p < 0.2$) is used for the $K_{\mu 2}$ selection. The probability for a muon to fake an electron in terms of identification is a major issue for the analysis, as discussed in Section 2.2.2.

2.2.1 Kaon beams

The beam line is capable of delivering simultaneous narrow-band K^+ and K^- beams overlapping in space, with a nominal central momentum which was chosen to be 75 GeV/c. However, the performance of the muon sweeping system was such that the K^-_{e2} candidates are affected by a larger background from the beam halo muons decaying into electrons than the K^+_{e2} ones ($\sim$ 20% vs $\sim$ 1%). Therefore only the K^+ beam was used for most of the run. A running period of two weeks with the K^- beam only (with the K^+ beam dumped in the beamline achromat) and higher proton intensity was taken to measure the rate of this background for the K^+ candidates. In addition, a period with both beams was taken in the beginning of the run, before the properties of the muon halo background were established. While the K^- only data allow background subtraction in the K^+ sample with a 0.1% precision, the background subtraction uncertainties affecting the K^- sample are yet to be assessed.

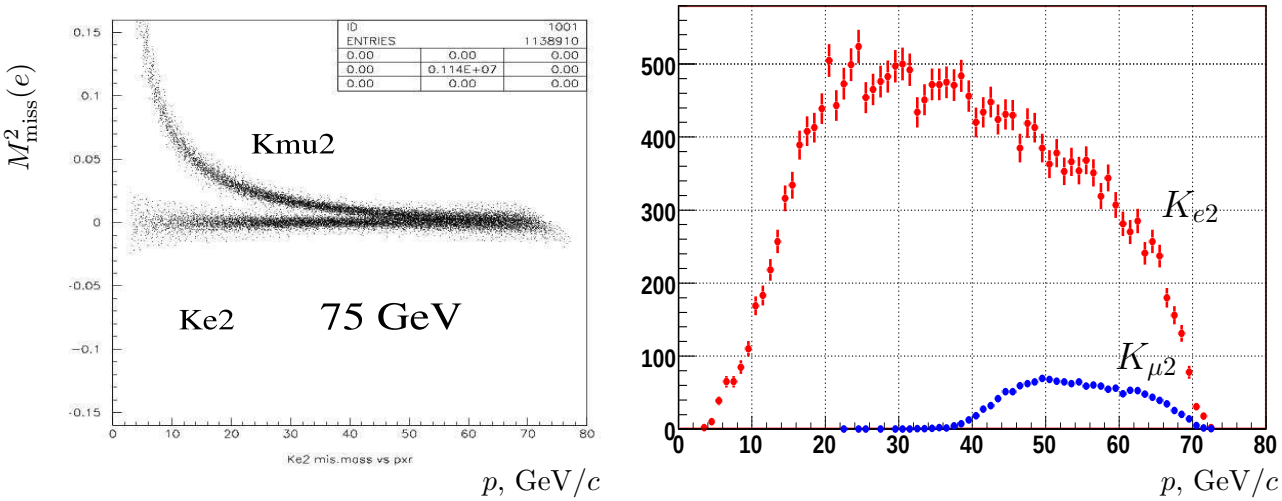

Figure 1: Left: missing mass squared assuming electron mass $M^2_{\rm miss}(e)$ for the charged track vs its momentum for K_{e2} and $K_{\mu 2}$ decays; impossibility of kinematic separation of K_{e2} vs $K_{\mu 2}$ at high track momentum is demonstrated. Right: momentum distribution of K_{e2} and $K_{\mu 2}$ events passing the full K_{e2} selection (Monte Carlo simulation results are presented in this section, since they provide more illustrative examples).

The resolution on the $M^2_{\rm miss}$ quantity used to identify the $K_{\ell 2}$ decays directly affects the background contamination in the K_{e2} sample, as demonstrated in Figure 1. The left plot shows that there is a considerable probability for a $K_{\mu 2}$ event to fake kinematically a K_{e2} event (and vice versa) in the region of track momentum $p > 35$ GeV/c. The right plot presents the $K_{\mu 2}$ background contamination in the K_{e2} sample after all the selection criteria (including particle identification) are applied: 17% contamination is expected in the kinematic region $p > 50$ GeV/c, and 7% contamination averaged over the whole analysis region 15 GeV/$c < p <$ 65 GeV/c.

The kaon momentum $\vec{P}_K$ is not measured directly for each event; the beam average measured with reconstructed $K^\pm \to 3\pi^\pm$ decays is used instead to compute $M^2_{\rm miss}$. To minimise the resolution on $\vec{P}_K$, narrow band and narrow angular spread kaon beams were used (in terms of absolute momentum, $\Delta P_K^{\rm RMS}/P_K \approx 2\%$, compared to 3% in 2003–04).

To improve the resolution on $\vec{P}_\ell$, maximum possible MNP33 momentum kick is used (263 MeV/c, compared to 120 MeV/c in 2003–04). In these conditions the resolution on track momentum is expected to be $\delta p/p = 0.47\% \oplus 0.020\% p$ (where p is expressed in GeV/c). In order to keep the beams within the beam pipe while traversing the apparatus, the beams are steered in directions opposite to spectrometer deflections by the TRIM3 dipole located upstream the entrance of the decay volume. The deflection angle was optimized in the course

of running (its final value is ± 0.2 mrad).

2.2.2 Muon identification

As discussed earlier, a $K_{\mu 2}$ decay can fake a K_{e2} decay in terms of track identification (high energy deposition by a muon owing to emission of a high energy bremsstrahlung photon). According to earlier preliminary measurements (and in reasonable agreement with simulations based on bremsstrahlung cross sections), the probability for a muon to have $0.95 < E/p < 1.05$ in the analysis track momentum range is $P(\mu \to e) \sim$ few 10^{-6} (and momentum dependent). Its magnitude, though relatively small, is non-negligible with respect to R_K, making the $K_{\mu 2}$ channel the main background to K_{e2}.

Direct measurement of $P(\mu \to e)$ is a necessary requirement for accurate background subtraction. To achieve this goal, a 4.5 cm thick lead wall (+2.0 cm thick iron support) was inserted between the two HOD planes to cover 6 horizontal counters (6.5 cm wide each) of the second HOD plane during the first half of the running time. The presence of the lead wall reduced the geometrical acceptance for the K_{e2} events by 18%. The requirement that the charged track after having traversed the lead gives a pulse height compatible with a minimum ionizing particle in the following HOD counter allows pure muon samples to be selected, in which the electron component (including electrons due to muon decays in flight) is suppressed.

The following pure samples of muons (in the whole analysis momentum range) were collected: 1) muons from the $K_{\mu 2}$ decays collected simultaneously with the main data taking; 2) muons from special muon runs during which the hadron beam was absorbed in the beam dump. Each of the two samples contains about 2000 muons in the range of poor $K_{e2}/K_{\mu 2}$ kinematical separation (35 GeV/c $< p <$ 65 GeV/c) traversing the lead wall and faking electrons by $0.95 < E/p < 1.05$.

With suitable corrections for energy loss in the lead wall itself, the measured LKR energy deposition of muons traversing the lead wall can be used to evaluate the background to K_{e2}. In addition, a highly pure sample of muons from the $K_{\mu 2}$ decays not necessarily traversing the lead wall (with electron contamination due to $\mu \to e$ decays to be subtracted by MC) can be kinematically selected in the track momentum region of good $K_{e2}/K_{\mu 2}$ separation, i.e. $p < 25$ GeV/c. While not of direct interest for background subtraction, this sample can be used to cross-check the lead wall based methods, and to study a possible non-uniformity of the E/p response of the apparatus.

2.2.3 Trigger logic

The following basic signals were used to form the trigger logic for the main decay channels of interest (K_{e2} and $K_{\mu 2}$).

- Q_1: a coincidence of hits in the two planes of the HOD;
- $E_{\rm LKR}$: energy deposition of at least 10 GeV in the LKR;
- 1TRK: at least 1 hit present in at least 2 of the 4 views of the DCH1;
- 1TRKM: 1TRK and loose upper limits for the numbers of hits in the DCHs.

A low bias trigger option was chosen to minimize the corresponding systematic effects, as suggested by the NA48/2 experience. As a start-up configuration, a trigger setup used for the special NA48/2 run in 2004 was used: the K_{e2} decays were collected with a $Q_1 \times E_{\rm LKR}$ condition, while the abundant $K_{\mu 2}$ decays were collected with the Q_1 condition alone downscaled by a factor $D = 50$. The Q_1 condition is mostly triggered by muon halo of the beam, and its purity with respect to the selected $K_{\mu 2}$ events was measured to be about 2%. The $Q_1 \times E_{\rm LKR}$ is satisfied by most $K^{\pm}$ decays except for the most abundant $K_{\mu 2}$, and its purity with respect to the selected (rare decay) K_{e2} events was measured to be about 10^{-5}. In addition to the main triggers, various downscaled control trigger samples were collected to monitor trigger efficiencies. The inefficiency of the Q_1 trigger (measured in 2004 to be at the level of 0.2% for an appropriate set of geometric acceptance cuts) is expected to cancel eventually in the $\Gamma(K_{e2})/\Gamma(K_{\mu 2})$ ratio. The inefficiency of the $E_{\rm LKR}$ condition for electrons, which directly enters the result, is controlled with the Q_1/D sample; it was measured with the 2007 data to be below 0.1% for the analysis track momentum cut of $p > 15$ GeV/c.
Continuous efforts to increase the trigger purity without affecting the efficiencies were made during the running. The following improvements were gradually introduced: 1) the 1TRK, and later the 1TRKM condition was added to the K_{e2} and $K_{\mu 2}$ triggers to suppress events due to kaon decays downstream the DCH1 plane; 2) the beam deflection angle at the entrance to the decay volume was optimized to minimize trigger rates; 3) the downscaling of the Q_1 trigger was increased to $D = 150$ (after the $E_{\rm LKR}$ inefficiency was measured to be sufficiently small). Each trigger improvement allowed increasing the beam intensity to fully occupy the readout bandwidth of $\sim$55K events per 14.4s SPS cycle. These improvements allowed an overall increase of the trigger purities and the K_{e2} candidate rate per SPS spill by almost a factor of 2.

Period	Pb wall	TRIM3 deflection	Intensity, ppp	K_{e2} trigger $K_{\mu 2}$ trigger	Rates /spill	Candidates /spill
23/06–11/07	Yes	$\pm$0.3 mrad	7×10^{11}	$Q_1 \times E_{\rm LKR}$	36K	0.23
				$Q_1/50$	16K	290
12/07–30/07	Yes	$\pm$0.3 mrad	8×10^{11}	$Q_1 \times 1{\rm TRK} \times E_{\rm LKR}$	33K	0.26
				$Q_1 \times 1{\rm TRK}/50$	17K	330
30/07–8/08	Yes	$\pm$0.2 mrad	11×10^{11}	$Q_1 \times 1{\rm TRK} \times E_{\rm LKR}$	31K	0.29
				$Q_1 \times 1{\rm TRK}/50$	21K	370
9/08–27/08	Yes	$\pm$0.2 mrad	13×10^{11}	$Q_1 \times 1{\rm TRK} \times E_{\rm LKR}$	42K	0.34
				$Q_1 \times 1{\rm TRK}/150$	7K	120
29/08–22/10	No	$\pm$0.2 mrad	18×10^{11}	$Q_1 \times 1{\rm TRKM} \times E_{\rm LKR}$	42K	0.54
				$Q_1 \times 1{\rm TRKM}/150$	10K	160

Table 1: Summary of the running periods: run conditions, typical proton intensity, definitions of the main triggers, trigger and event candidate rates per 14.4s SPS spill.

2.2.4 Data sample recorded

The K_{e2} physics run took place from June 23 to October 22, 2007. A summary of run periods showing the improvements in data taking and trigger conditions, beam intensities, and event rates per SPS spill is presented in Table 1.

A cumulative plot of the number of K_{e2} candidates collected (satisfying rather tight selection conditions of the online monitor) is presented in Figure 2. Period-to-period improvements of event rate indicated in Table 1 are clearly visible. Short periods with null K_{e2} candidate rate are mostly due to either special data taking conditions aiming at studies of systematic effects, or the SPS machine development periods. The conservative online estimate of the number of K_{e2} candidates is 112K, of which about 92K are K^+, and the rest are K^- candidates. These figures are to be compared to the previous largest single experiment sample of 8K candidates (KLOE [7]).

2.3 Data analysis

The analysis strategy is based on counting the numbers of reconstructed K_{e2} and $K_{\mu 2}$ candidates collected simultaneously, consequently 1) the result is independent of the knowledge of the kaon flux; 2) several systematic effects, such as parts of the trigger and detection efficiencies, cancel in the ratio.

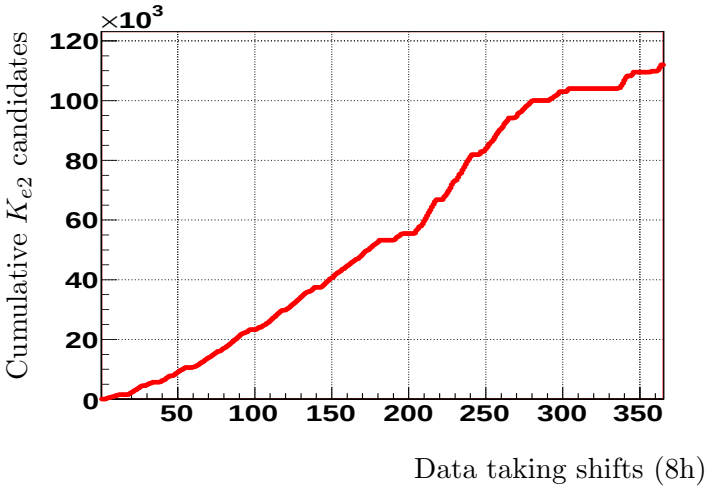

Figure 2: Cumulative plot of the number of K_{e2} candidates recorded in 2007.

The correction for difference of K_{e2} and $K_{\mu 2}$ geometric acceptances is computed by Monte Carlo (MC) simulation. However the MC is used to a limited extent only: trigger and particle identification efficiencies, which are difficult to reproduce with simulation, are measured directly using the data.

The analysis is performed independently for each of the data taking periods with differing running conditions, and in bins of the reconstructed momentum of the charged track. The primary reason for momentum binning is that background contaminations in the K_{e2} (see Figure 1) and $K_{\mu 2}$ samples strongly depend on this variable. The ratio R_K in every momentum bin can be computed as

$$R_K = \frac{1}{D} \cdot \frac{N(K_{e2}) - N_{\mathrm{B}}(K_{e2})}{N(K_{\mu 2}) - N_{\mathrm{B}}(K_{\mu 2})} \cdot \frac{f_\mu \times A(K_{\mu 2}) \times \epsilon(K_{\mu 2})}{f_e \times A(K_{e2}) \times \epsilon(K_{e2})}, \tag{4}$$

where $N(K_{\ell 2})$ are the numbers of selected $K_{\ell 2}$ candidates ($\ell = e, \mu$), $N_{\mathrm{B}}(K_{\ell 2})$ are numbers of background events, f_ℓ are efficiencies of e/μ identification criteria, $A(K_{\ell 2})$ are the geometrical acceptances computed with MC, $\epsilon(K_{\ell 2})$ are trigger efficiencies, and D is the downscaling factor of the $K_{\mu 2}$ trigger.

An express analysis based on a fraction ($\sim 3\%$) of the 2007 K^+ data sample (lacking the final detector calibrations) was performed to evaluate the data quality, and confront the results to the expectations from the simulation. The corresponding K_{e2} and $K_{\mu 2}$ missing mass plots are presented in Figure 3.

Systematic uncertainties

Backgrounds in the K_{e2} sample. As discussed in Section 2.2.2, the main source of

background is that due to $K_{\mu 2}$ decays with misidentified muon. As a part of the express analysis, the probability for a muon to fake an electron $P(\mu \to e)$ was measured using the special 2007 muon run with the lead wall installed (which is only a part of the available pure muon sample). An example of the measured muon E/p spectrum, and the resulting $P(\mu \to e)$ in track momentum bins are presented in Figure 4 (small corrections for energy loss in the lead wall itself are still missing). The $K_{\mu 2}$ background contamination (plotted in Figure 3a) was estimated to be $(7.5 \pm 0.2)\%$.

The background induced by the muon halo discussed in the Section 2.2.1 (visible at $M^2_{\rm miss} < 0$ in Figure 3a), was measured to be $(1.3 \pm 0.1)\%$ using the run period with the the K^+ beam dumped. The contamination can be further decreased be applying a stricter cut on the closest distance of approach between the charged track and the mean beam trajectory.

Other identified sources of background in the K_{e2} sample (due to kaon decays, and not involving particle misidentification, meaning that they can be reliably subtracted using MC simulation) are the following. (1) the "structure dependent" radiative $K_{e2\gamma}(SD)$, contamination estimated by MC is $(0.7 \pm 0.1)\%$ for data collected without the lead wall, and $(2.8 \pm 0.4)\%$ for data collected with the lead wall. The precision of the estimate is currently limited by the poor experimental knowledge of $K_{e2\gamma}(SD)$ branching fraction; a separate NA62 measurement of the rate is foreseen. (2) $K^+ \to \pi^0 e^+ \nu$: contamination estimated by MC is well below 1%, and only at high track momentum.

The $K^\pm \to \pi^\pm \pi^0$ decay is a potential source of background, however no evidence for it was found in the 2004 test run data at 1% precision level. A possible subtraction procedure is based on kinematic rejection, and measurement of pion misidentification probability.

Backgrounds in the $K_{\mu 2}$ sample. The following sources were identified: 1) background from the muon halo, about 0.1% contamination, to be subtracted as for the K_{e2} decays; 2) $K^\pm \to \pi^\pm \pi^0$ background, contamination below 0.5%, to be subtracted by MC using the measured probability of pion misidentification.

Electron identification efficiency (and its dependence on track momentum and impact point position) can be measured with a clean sample of electrons by kinematic selection of the $K^\pm \to \pi^0 e^\pm \nu$ decays collected simultaneously with the main data sample. However the accessible kinematic region is limited to $p < 50$ GeV/c. To cover the whole analysis momentum range, a special 15h run with a broad band K_L beam was carried out. A preliminary analysis of the $K_L \to \pi^\pm e^\mp \nu$ decays from this run demonstrated that f_e is higher than 99% in most of the analysis momentum region (actually increasing with p), as presented in Figure 5. A further improvement is expected when the final LKR calorimeter calibrations are

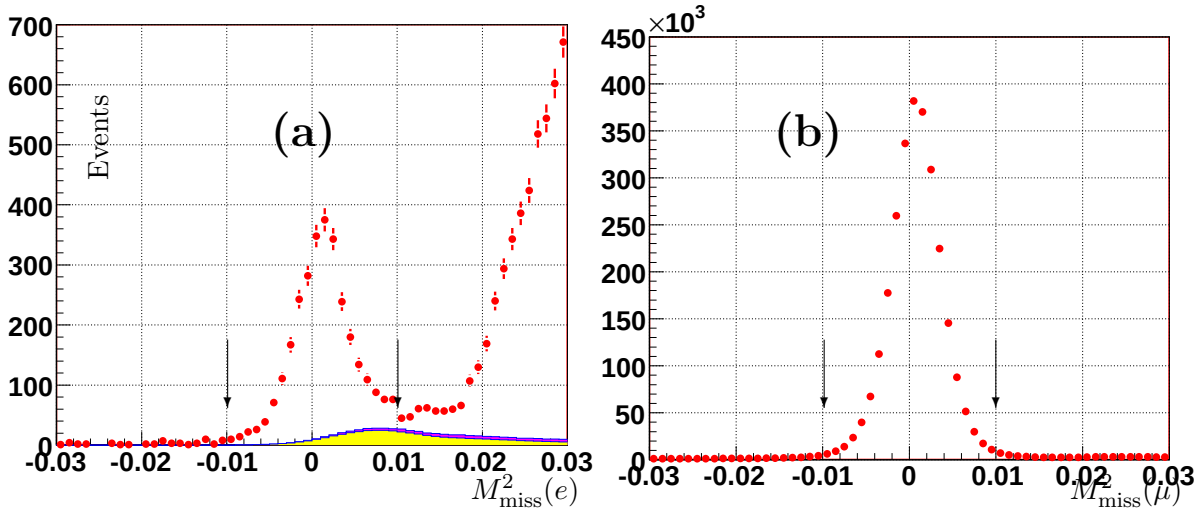

Figure 3: Missing mass squared in (a) electron, (b) muon hypothesis for events passing the other K_{e2} and $K_{\mu 2}$ analysis cuts, respectively, for the analyzed fraction of the 2007 data. The $K_{\ell 2}$ peaks are shifted with respect to zero due to lack of spectrometer absolute calibration. The measured $K_{\mu 2}$ background in the K_{e2} sample is marked with a shaded area. The analysis missing mass cuts are marked with arrows.

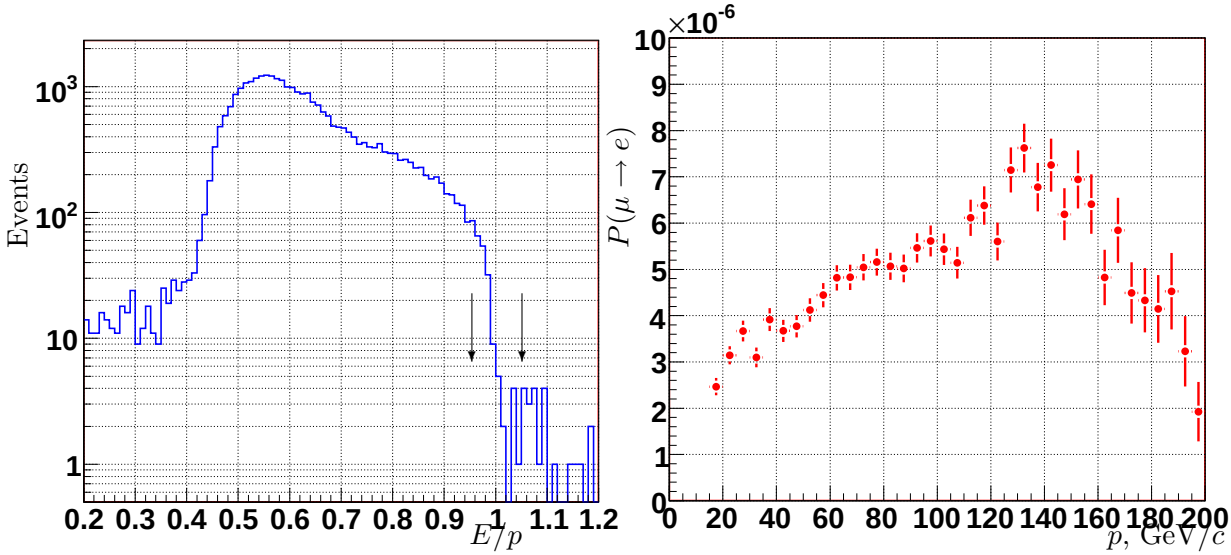

Figure 4: a) E/p spectrum of muons with 20 GeV/c $< p <$ 25 GeV/c triggered by $Q_1 \times E_{\rm LKR}$. The drop below $E/p \approx 0.4$ is due to the 10 GeV LKR energy deposition requirement in the trigger. Electron identification range is marked with arrows. b) The measured $P(\mu \to e)$ vs track momentum.

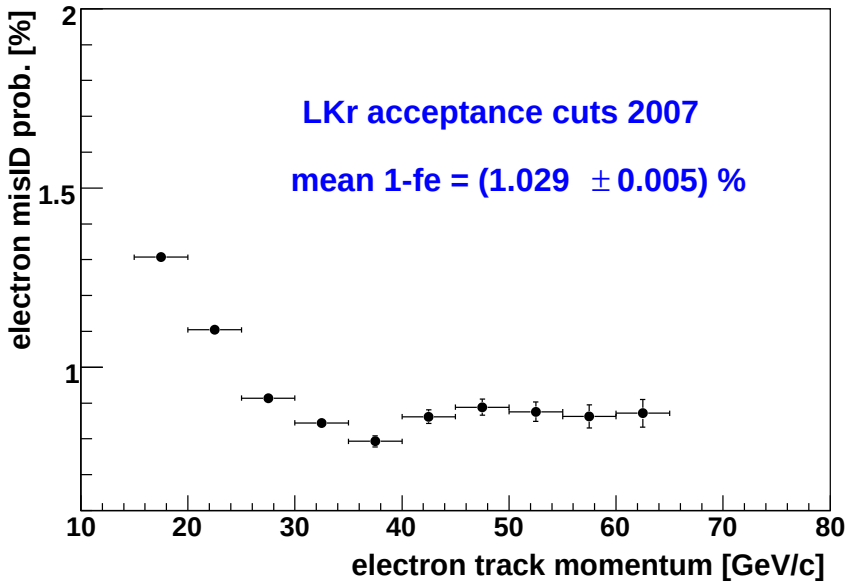

Figure 5: Electron mis-identification probability $1 - f_e$ vs track momentum in the analysis momentum range.

implemented, and the database of dead cells is updated. The precision of f_e measurement is expected to be better than 0.1%.

Muon identification efficiency f_μ was measured in 2004 to be momentum dependent, and lie in the range from 0.996 to 0.999 in the analysis track momentum region. It can be measured with a precision much better than 0.1% with a pure muon sample. In fact, a measurement of f_μ is simpler than a measurement of $P(\mu \to e)$, since any electron contamination in a muon sample is outside the muon identification range of $E/p < 0.2$.

Geometric acceptance correction $A(K_{\mu 2})/A(K_{e2})$ is momentum dependent, and ranges (for the presently used selection) between 1.2 and 1.3 in the analysis momentum interval. The size of the correction can be significantly decreased by using an inclusive K_{e2} selection accepting also the $K_{e2\gamma}(IB)$ contribution. The 2004 analysis has demonstrated that the MC correction can be performed with a precision better than 0.1%, after the appropriate MC beam spectrum tuning is performed to match the data.

Trigger efficiency correction $\epsilon(K_{\mu 2})/\epsilon(K_{e2})$ is discussed in Section 2.2.3: the efficiencies are measured directly with the data, and the expected size of the correction is as small as $\sim 0.1\%$, thanks to the low bias trigger strategy.

Other known sources of systematic uncertainties (which contribute at 0.1% level, and can be corrected for using the data) include: 1) trigger afterpulses biasing the Q_1 downscaling factor D; 2) global LKR calorimeter readout inefficiency.

2.4 Summary

The data sample collected in 2007 allows a statistical precision of $\delta R_K/R_K = 0.3\%$ to be archived. Data taking strategy was optimized using the experience of NA48/2 K_{e2} analysis to minimize and/or correctly account for the systematic biases. Preliminary studies of the expected systematic uncertainty demonstrate that a total precision of $\delta R_K/R_K = 0.5\%$ is within the reach.

2.5 Data Processing

The data collection and storage has been performed using essentially the hardware and software infrastructure at CERN: during the SPS extraction the raw data from the subdetectors were sent to the online farm for event building. Data was shipped through an high-speed dedicated network link to the Central Data Recording [CDR] running on the central CERN batch facility [lxbatch]. The CDR runs the event reconstruction software and applies a filter [Level-3] removing not interesting events on the basis of very safe cuts. This reduces by about 70% the total amount of data written to tape. During the first period of the data taking –until July 15th– the Level-3 software was used only in flagging mode, i.e. without actually rejecting any event, in order to check the reliability of the filter. In order to save tape space, the same filter has been applied to data taken before July 15th after the end of the data taking. The output of the Level-3 [both the filtered raw and the reconstructed events] was then sent to the CASTOR storage facility for the migration to tape. The reconstructed data are used for the production of calibration constants, needed for a further reconstruction step performed after the data taking.

The amount of raw data from the experiment to the CDR has been of more than 50 000 triggers per burst, with an average size of 11 kB/event, corresponding to a sustained average bandwidth of 35 MB/s. About 450 000 bursts were collected, for a total amount of processed data of the order of 300 TB, corresponding to a total amount of raw data stored to tape of 90 TB after the Level-3 filtering. The commitment and the services provided by the CERN IT Department are acknowledged and very much appreciated.

3 Sensitivity Studies for $K^+ \to \pi^+ \nu\bar{\nu}$

3.1 Introduction

The sensitivity of the experiment has already been investigated [8] with the configuration described in the proposal [9]. However, the simulation used in that analysis had simplifications reflecting the still approximate design of the various sub-detectors. Following the changes and improvements achieved in the last two years in the general layout and in the sub-detectors design, a more sophisticated simulation has been built and some crucial aspects of the sensitivity re-analyzed. Particular attention has been paid to the variation of the background rejection using the new spectrometer configuration with four straw chambers and one magnet only.

3.2 Background characterisation

The signature of the $K^+ \to \pi^+ \nu\bar{\nu}$ event is one track in the final state and nothing else. All the other events having a similar signature are backgrounds. Their rejection relies on the event kinematics, on the veto of photons and on the particle identification. The kinematics of a one-track event can be fully described using the M^2_{miss} defined as the square of the difference of the four-momentum of the kaon and of the charged decay product under the assumption that it is a pion. Using this variable two categories of background can be distinguished: one kinematically constrained, and the other kinematically not constrained (see Figure 6). The decays belonging to the first class correspond to more than 80% of the total K^+ branching fraction. Among them, the $K^+ \to \pi^+\pi^0$ is particularly dangerous because it falls in the kinematics region of the signal. Due to its high branching ratio, a $K^+ \to \pi^+\pi^0$ rejection factor larger than 10^{12} is required, which is achievable only if the kinematical rejection complements the photon rejection. As a consequence the signal has to be looked for in two separate regions around the $K^+ \to \pi^+\pi^0$ peak, called region I and region II. The need of such a cut drove the choice of the technology for both the beam and the pion spectrometer. Similar considerations are valid for $K^+ \to \mu^+\nu$ events, where the kinematical rejection complements the muon identification. Photon veto and particle identification, instead, are the only experimental tools available for the rejection of the non-constrained background. In this case, however, the rejection profits from the relatively small branching ratios of the channels.

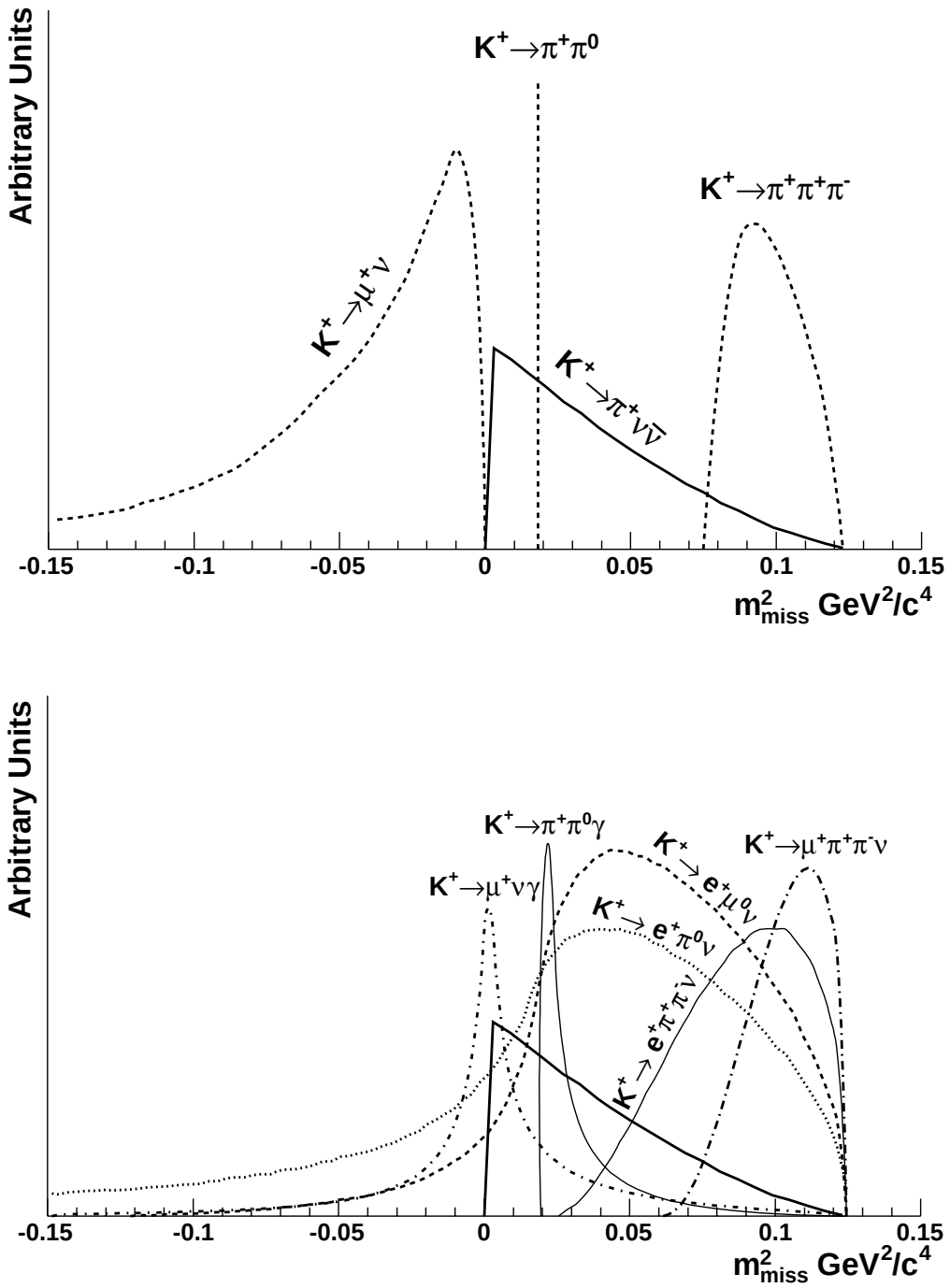

Figure 6: Shape of the M^2_{miss} for signal and background events reconstructed from the generated kaon and charged decay product three-momenta. The downstream track is assumed to be a pion. The kinematically constrained background is depicted in Figure (a), the not kinematically constrained in Figure (b). The relative normalisation is arbitrary.

3.3 Simulation

A geometrical simulation of the whole apparatus in the configuration proposed in this addendum has been developed. The response of the various sub-detectors has been implemented in form of libraries, built from specific stand-alone simulations and analyses of test beam data. The beam line has been simulated with Turtle and Halo. The Gigatracker stations and the straw chambers have been simulated using Geant4 [10]. The large angle photon vetoes have been studied using Geant4 simulations and data from a test beam performed in Frascati. Results from data and the well-tested NA48 simulation have been used for the liquid krypton calorimeter.

3.4 Kinematical reconstruction

Kaon tracks have been generated according to the layout proposed in this addendum. The hits released by a beam particle in the Gigatracker stations are grouped to form a track. A 2% inefficiency per station is assumed. The pattern recognition makes use of the timing information, of the χ^2 of the track projection in the non-bending plane of the spectrometer and of the knowledge of the average beam momentum*. A fit to the hit points gives the slope of the beam track in the non-bending plane. The momentum and slope of the track in the bending plane, instead, are computed analytically. The resolution is about 150 MeV/c for the momentum and about 12 μrad for the angle measurements. The reconstruction efficiency is about 92%.

The kaon decays in the regions between the third station of the Gigatracker and the first straw chamber have been considered. The straw chamber spectrometer measures the three-momentum of the charged decay product. The distance between a straw wire and the particle impact point on the straw tube is measured from the time collection of the induced signal with 130 μm resolution. A view plane is composed of four tube layers to resolve the left-right ambiguity. A space hit in one chamber is defined as the intersection of the coordinate of the impact point measured in each view plane. Because of the geometry of these planes, a hit may have a reconstructed number of views varying from 1 to 4, depending on the impact point position. As a consequence, ghost hits appear in case of multi-track events. On average five hits per chamber are reconstructed in three track events. The hits with at least 2 views are grouped to form a track. Tracks with hits in four and three chambers are looked for. In case of tracks with four hits, the pattern recognition makes use of the χ^2 in the non-

*During real data taking the average kaon momentum can be measured using events like $K^+ \to \pi^+\pi^+\pi^-$.

bending plane and of the distance between the extrapolation to the magnet of the segments built using the hits before and after the magnet. A more sophisticated algorithm groups the hits to form a 3-hit track. The probability of fake track reconstruction in three track events is estimated at the level of percent. The three-momentum of the track is measured using a least squared fit to all the reconstructed views. The covariance matrix due to the effect of multiple scattering is also taken into account. The momentum resolution can be parametrized as $\sigma(P)/P = 0.33\% \oplus 0.007\%P$. The average angular resolution varies from 55 μrad at 10 GeV/c to 20 μrad at 60 GeV/c. The resolution of the M^2_{miss} as a function of the track momentum is shown in Figure 7.

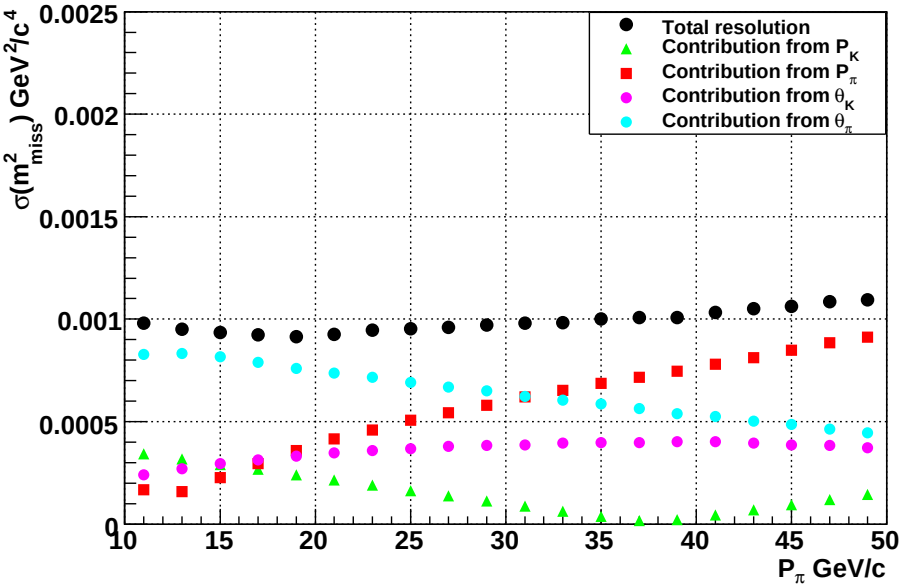

Figure 7: Squared missing mass resolution as function of the pion momentum in $K^+ \to \pi^+\pi^0$ events. The different contributions to the total resolution are also shown.

The intersection between the track reconstructed in the Gigatracker and in the downstream spectrometer gives the decay vertex position with about 30 cm resolution along the z axis. The closest distance of approach (CDA) between the two tracks has a resolution of about 1 mm.

3.5 1-Track Events Selection

The fiducial region extends from 5 to 65 m downstream of the last station of the Gigatracker. The accepted events must have at least one track reconstructed in the Gigatracker and only one track in the straw chambers and in the RICH. A track in the downstream spectrometer

must have hits in all the four chambers and a χ^2 lower than 2. The RICH provides the time of the event with a resolution better than 100 ps. Because the rate in the Gigatracker is about 800 MHz on average and the time resolution of one Gigatracker station is about 200 ps, more than 30% of events have at least two tracks reconstructed in the Gigatracker in a 200 ps window around the event time. The association between the beam track and the downstream track is made on the basis of the time difference and of the CDA of the reconstructed vertex. Once the kaon track is selected, the decay vertex must fall within the fiducial region and have a CDA less than 0.8 cm. The reconstructed downstream track has to hit a region of the straw chambers corresponding to at least 2 views per hit, must pass through the RICH volume without intersecting the 8.5 cm radius beam pipe and has to fall within the liquid krypton acceptance. This last requirement helps to reject backgrounds with positrons. The liquid krypton, in fact, must complement the RICH in the π/e separation, because of the high branching ratio of the $K^+ \to e^+\pi^0\nu$ decay. For similar reasons applied to the π/μ separation, the track must also be within the muon detector acceptance. Because the pion detection threshold in the RICH is about 13 GeV/c, events with a track having a momentum lower than 15 GeV/c are rejected. Event with the track momentum above 35 GeV/c are also rejected. This last cut costs about 50% in signal acceptance, but is crucial to reject the $K^+ \to \pi^+\pi^0$. In this case, in fact, the π^0 has at least 40 GeV/c and can be vetoed with an inefficiency smaller than 3.5×10^{-8}. Moreover also the muon rejection takes advantage of this cut because the π/μ separation deteriorates rapidly above 35 GeV/c. Finally, considerations based on the signal over background ratio lead to the following kinematics cuts:

- $0 < m^2_{miss} < 0.01$ GeV^2/c^4 (region I)
- $0.026 < m^2_{miss} < 0.068$ GeV^2/c^4 (region II)

3.6 Signal and Background analysis

The $K^+ \to \pi^+\nu\bar{\nu}$ decays have been generated including a vector form factor similar to the one contributing to the $K^+ \to e^+\pi^0\nu$ decay. The signal acceptance is 14.4%: 3.5% in region I and 10.9% in region II. The acceptance is about 15% lower than the one obtained with the detector configuration used in the proposal. The loss comes from a pion dispersion effect due to the single spectrometer magnet and the acceptance cuts at the RICH and liquid krypton. The effect is enhanced by the long lever arm between the spectrometer magnet and the 4th straw chamber needed to detect extra charged particles in decays with more than one charged particle in the final state, like $K^+ \to e^+\pi^+\pi^-\nu$ or $K^+ \to \pi^+\pi^+\pi^-$.

The new configuration with one magnet and four chambers only might have an impact on the rejection of $K^+ \to \pi^+\pi^0$ and $K^+ \to \mu^+\nu$ decays. A less performant spectrometer, in fact, could reduce the kinematical rejection power. The quality of kinematical rejection depends on the resolution of the M^2_{miss}, which depends in turn on the non-gaussian tails affecting the downstream track reconstruction and on the wrong kaon association. The second effect is almost independent of the spectrometer configuration and was estimated [8] to induce a 10^{-4} inefficiency in the $K^+ \to \pi^+\pi^0$ and 5×10^{-6} in the $K^+ \to \mu^+\nu$ rejections. In the present configuration this number should be 15% lower because of the smaller geometrical acceptance. The effect of the non-gaussian tails, instead, has been re-evaluated with the new spectrometer configuration. These tails come from large angle scattering suffered by the charged particle passing through the chambers, as a consequence of hard $\delta-$rays production and elastic hadronic interactions. These processes have been simulated using Geant4. About 3×10^{-5} $K^+ \to \pi^+\pi^0$ remain because of the non-gaussian tails, before applying the veto on the π^0. The residual events are distributed symmetrically in region I and II. Half of them are due to the tails in the angle reconstruction, half to the momentum reconstruction. The cut on the CDA is very effective in controlling the contribution from the angle reconstruction. The use of four chambers and one magnet only does not give extra degrees of freedom internal to the spectrometer to handle the contribution from the momentum reconstruction. To compensate for this, the RICH may provide an independent measurement of the pion momentum with a resolution four times worse than the one given by the spectrometer. Indeed such a redundancy may be used to reduce by another factor two the contribution to the $K^+ \to \pi^+\pi^0$ background from the non-gaussian tails, but at the price of 20% in signal acceptance. However, this contribution is at least three times smaller than the one due to kaon mis-matching: for this reason the extra cut on the momentum measured with the RICH does not improve the total signal over background ratio and it is not applied.

Using a similar analysis, about 3.1×10^{-6} $K^+ \to \mu^+\nu$ remain because of the non gaussian tails and without applying the muon identification. In this case the momentum measured with the RICH is not redundant since the RICH will be used for π/μ separation.

The π^0 and μ veto inefficiency in $K^+ \to \pi^+\pi^0$ and $K^+ \to \mu^+\nu$ events can be considered to be almost independent of the kinematical rejection inefficiency. Assuming 3.5×10^{-8} for π^0 veto inefficiency, the total $K^+ \to \pi^+\pi^0$ background is about 7.5%, with 2% due to the effect of the non-gaussian tails. Assuming 10^{-5} as muon detector inefficiency and the results from the RICH simulation for the inefficiency of μ/π separation, the background due to the $K^+ \to \mu^+\nu$ is about 2.6%, with 1% due to the non gaussian tails. The reconstructed M^2_{miss}

for signal and $K^+ \to \pi^+\pi^0$ and $K^+ \to \mu^+\nu$ is shown in Figure 8. Only the contribution to the tails of the reconstructed downstream track is considered. These histograms are normalized to the 4.8×10^{12}/year kaon flux expected in the fiducial region and take into account inefficiencies in the π^0 veto and the μ/π separation.

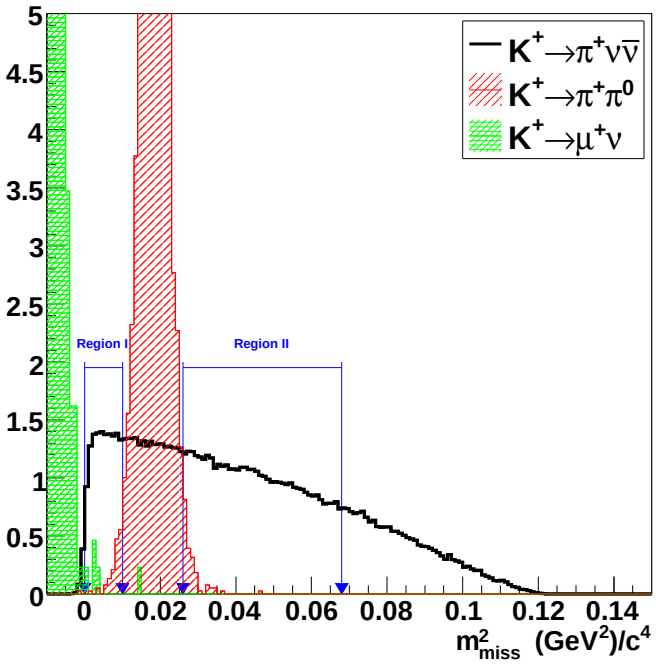

Figure 8: Reconstructed squared missing mass for signal and $K^+ \to \pi^+\pi^0$ and $K^+ \to \mu^+\nu$ background.

No significant variations with respect to the double spectrometer configuration previously proposed are expected in the other backgrounds.

3.7 Conclusions

We observe a 15% reduction in the signal acceptance using the present spectrometer configuration with respect to the double spectrometer setup which is offset by better immunity to K_{e4} backgrounds and a more conservative layout of the straw tracker.

4 The Beam for the $K^+ \to \pi^+\nu\bar{\nu}$ Experiment

Figure 9 represents the updated layout of the beam to measure $K^+ \to \pi^+\nu\bar{\nu}$ with a single magnet spectrometer configuration. Compared to earlier version (described in the Proposal P-326), the optics are adapted to the requirement of suppressing the e^+ component in the unseparated, positively-charged beam. The necessary condition is that, after initial momentum selection, the beam is brought to double (horizontal and vertical) focii at a point where a thin (0.1 X_0) W radiator can be introduced. This causes the e^+ to lose sufficient energy by Bremsstrahlung to be rejected after further momentum definition. The relatively large divergences of the beam at the focii ensure that multiple-scattering in the radiator material does not lead to catastrophic loss of the hadrons out of the defined beam emittance.

The 75 GeV/c, narrow momentum-band (1.2 % RMS), hadron beam is derived from the existing target station T10. The elements are installed along the present K12 beam line pointing towards the existing LKR calorimeter. The design employs a triplet of radiation-resistant, acceptance quadrupoles to focus the beam to the mid-point of a *front-end achromat*, which is composed of four (MTRV) dipole magnets to provide momentum selection and recombination. In the middle of the achromat the wanted beam is displaced vertically downwards by 100 mm, allowing its momentum band to be defined and primary protons and unwanted secondary hadrons to be dumped in the two motorized dump/collimator units (TAX), in between which the e^+ radiator is located. A subsequent quadrupole triplet refocuses the beam through a collimation and muon-sweeping stage. A quadrupole doublet then renders the beam parallel, matching it to a modified (H_2-gas filled) CEDAR differential Cerenkov counter to tag the K^+. A final quadrupole doublet is used to match the beam to the spectrometer and tracking system, whilst limiting the beam size in the apertures of the downstream detectors. The beam tracking system (for the layout of the detectors the reader should refer to Figure 12) consists of three *Gigatracker*(GTK) stations, composed of Si-pixel arrays each of active size: $\pm$ 30 mm (horizontally) by $\pm$13.5 mm (vertically), installed in vacuum. These are rearranged so that the space between GTK 1 and 3 is occupied by a toroidally magnetized muon **scraper** and a *second achromat* of four C-shaped (MCBH) dipole magnets, with their yokes arranged so as to enhance the defocusing action of the scraper for μ^+. In the middle of the second achromat, where GTK 2 is located, the magnets cause a parallel displacement of the +75 GeV/c beam by +60 mm in the **horizontal** plane to provide the momentum measurement. GTK 3 is placed **after** the final (variable) cleaning collimator and is followed by a *guard-ring* of scintillation counters (LAV-0 of inner/outer diameter 100/300mm) mounted in vacuum and by a veto counter (VETO-0) surrounding

the vacuum tube.

The (opposite) deflections of the last two magnets of the second achromat are actually so tuned that the beam is centred at GTK 3, but is directed away from the axis by -1.2 mrad in the horizontal plane. This angle is chosen so that the subsequent Single Spectrometer magnet will deflect the beam back into the central aperture of the LKR calorimeter. The existing decay vacuum tank, shortened by about 34 m, is connected in liaison with the former *He tank* and is evacuated (to $\approx 10^{-6}$ mbar pressure). The latter is extended by ≈14 m and houses the spectrometer, designed to detect and track charged particles from K^+ decays in the 60 m long fiducial region and thereby also to provide hermetic coverage for π^- from Ke4 decays of momenta $\leq$ 60 GeV/c. Tracking is performed by 4 chambers in vacuum, each consisting of 4 quadruple planes of straw tubes, 2.1 m long, (arranged in x-, y-, u-, v-projections), leaving 120 mm wide/high gaps centred on the deflected beam trajectory. These chambers, ST-CH 1 - 2 and 3 - 4, are located, with appropriate lever-arms, upstream and downstream of the existing, large-aperture spectrometer magnet, MNP33. The magnet provides a pT-kick of +270 MeV/c, giving a +3.6 mrad deflection to the +75 GeV/c beam. In conjunction with the upstream deflection of -1.2 mrad, the beam thereby converges to the undeflected beam axis at a point near the exit of the LKR calorimeter.

The LKR is followed by the re-instrumented hadron calorimeter (HAC), an additional iron-wall of 0.8 m thickness and x-, y- planes of a (new) MU VETO detector. The beam is finally deflected to the side by a 3 m long, 200 mm gap, IHEP dipole magnet, MSP-12A, which provides a +1620 MeV/c pT-kick (+21.6 mrad deflection). The remaining length between the Al vacuum window at the end of the spectrometer and the LKR is occupied by a RICH counter, of length 18.0 m and outside diameter 2.8 m, filled with Ne gas at atmospheric pressure. The counter is traversed by a central, thin-walled, beam tube (inside diameter 163mm). It is followed by the two scintillator planes of the existing charged hodoscope (CHOD 1, 2). The decay vacuum-tank, single-spectrometer and RICH are interspersed by 12 annular, large-angle photon-veto counters (LAV 1 - 12), which surround the acceptance cone for charged-particles. These are assumed to be constituted of overlapping rings of 370 mm-long lead-glass blocks, recuperated from the OPAL 'Barrel' detector, arranged radially with their PMs protruding from new, cylindrical sections of the vacuum tank. An Intermediate Ring Calorimeter, IRC, (inner/outer diameter 140/240mm) is located at the downstream end of the RICH to cover the central, inactive region of the LKR. Together with the large-angle LAV-counters and the final (220 mm x 220 mm) Small-Angle Calorimeter (SAC) located 7.3 m downstream of the centre of MSP-12A, they assure hermetic coverage to veto photons

emitted at all angles $\leq$48 mrad from K^+ decaying in the fiducial region. Finally, the +75 GeV/c beam, deflected to the side of the SAC, is dumped in a concrete plug inside an enlarged (800 mm diameter, 8 metres deep) hole at the end of Hall ECN3.
Apart from the suppression of the positron component and a revised matching to the dimensions of the Gigatracker, the overall characteristics of the beam are similar to those of the beam as described in the Proposal. A comparison with the performance of the beam quoted in the Proposal is shown in Table 2. The calculated muon halo rates in the principal detectors are shown in Table 3; they are not significantly different from those in the Proposal.
The relative composition of hadrons in the beam (at 102 metres from the target) is now based on the mean of measurements performed at +75 GeV/c momentum from 500 and 300 mm Be targets, using a Nitrogen filled CEDAR in the H2 beam at the SPS (October 2007). The results of these measurements are shown in Figure 10 and 11, respectively.

5 Detectors

The updated list of detector elements for the $K^+ \to \pi^+\nu\bar{\nu}$ experiment and a brief functional description is given here for reference. A conceptual layout of the updated setup is shown in Figure 12.

1. CEDAR

   A Differential Cherenkov counter (an upgraded form of the CEDAR built for the SPS secondary beams) placed on the incoming beam to tag the minority particles of interest (kaons).

2. GIGATRACKER

   Thin silicon micro-pixel detectors for (redundant) momentum measurement of the incoming beam with sub-nanosecond time resolution to provide a tight time coincidence between the incoming kaon and the outgoing pion.

3. CHANTI

   A set of ring anticounters after the last Gigatracker station to form a "guard ring" and a large one around the beginning of the decay volume to veto charged particles coming from the collimator.

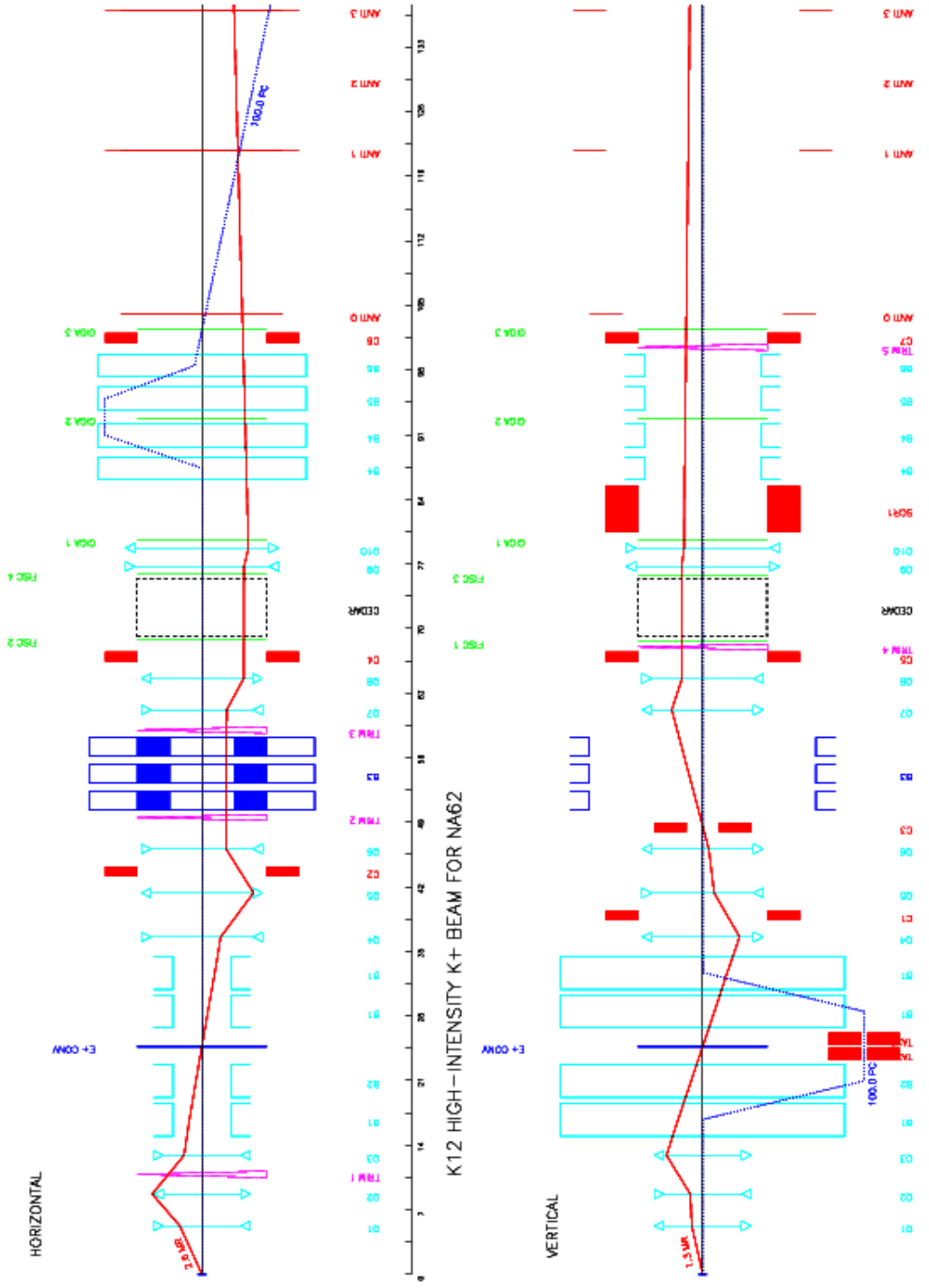

Figure 9: Schematic layout and optics of the high intensity K^+ beam.

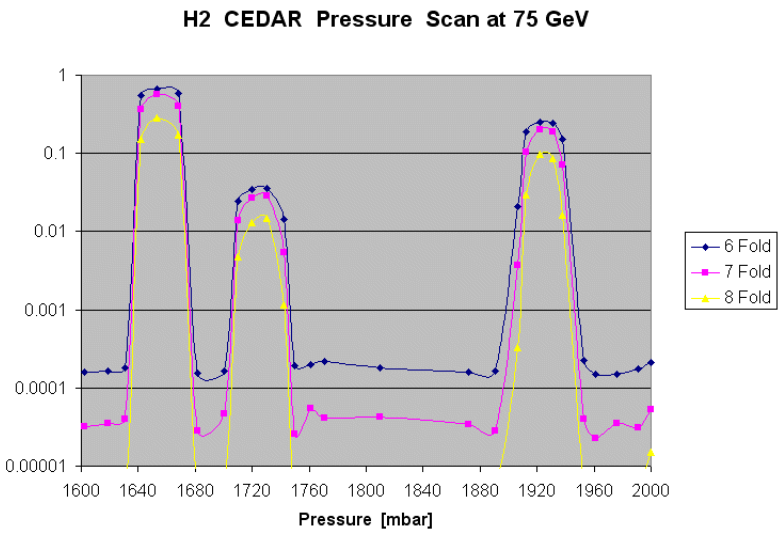

Figure 10: CEDAR pressure scan in a +75 GeV/c beam from a 500 mm Be target.

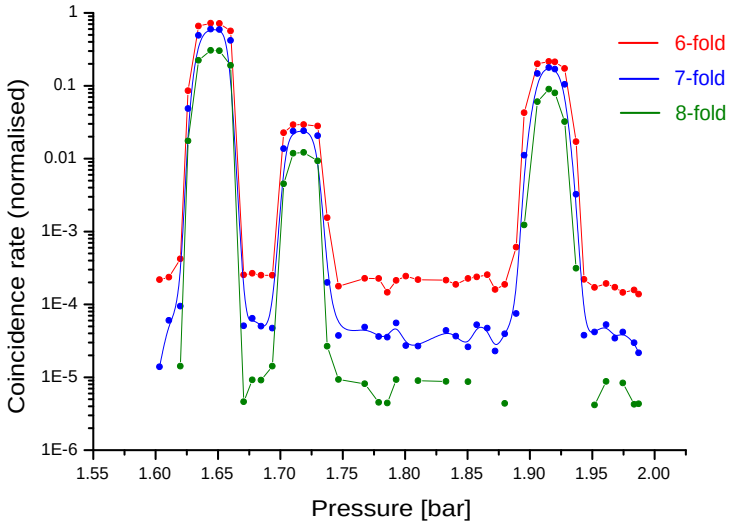

Figure 11: CEDAR pressure scan in a +75 GeV/c beam from a 300 mm Be target.

Parameter	Present Design	In Proposal
Incident protons per pulse on T10 target, assuming a 4.8 s flat top (3 s eff. spill) every 16.8 s	3.3×10^{12}	3.0×10^{12}
e^+ radiator	1 X_0 W	none
Angular acceptance Horizontal × Vertical $[\text{mrad}]^2$	$\pm 2.6 \times \pm 1.3$	$\pm 2.3 \times \pm 2.1$
Solid Angle [μsterad]	$\simeq 12$	$\simeq 16$
Central momentum [Gev/c]	+75	+75
RMS momentum spread [%]	1.2	1.0
RMS divergence H,V [mrad] at CEDAR	0.071, 0.074	0.08, 0.08
at GTK3	0.10, 0.09	0.11 0.10
2 × RMS beam size H,V [mm] at GTK1	28.9, 11.9	–
at GTK2	27.1, 11.8	–
at GTK3	25.9, 11.9	16, 22
at last STRAW ch	21.8, 25.2	25,25
Beam flux per pulse [$\times 10^6$] protons	550 (23%)	490
K^+	**145 (6.0%)**	**150**
π^+	$\approx$ 1685(70%)	1500
e^+,μ^+	$\approx$ 1, $\approx$ 20 ($\approx$ 1%)	$\approx$ **350**, ($\approx$ 20)
Total	$\approx$ **2400**	$\approx$ 2500
Effective total rate [MHz]	$\approx$ 800	

Table 2: Performance characteristics of the new beam, compared with those in the original P-326 Proposal.

Detector concerned	Present Design	In proposal
	Sim. halo rate in MHz, [max KHz/cm^2]	Sim. halo rate in MHz, [max KHz/cm^2]
CEDAR-PM's ($8 < r < 12$ cm)	1.9 [8]	2.5 [10]
Large angle veto ANTI 1	1.4 [0.1]	–
ANTI 1-12 OR	4.4	≈ 4
Last straw chamber: per plane,		
$5 \leq \lvert x \rvert \leq 105$ cm	9	$\approx$10
per 1 cm diameter straw	0.5 [$\approx$40]	≈ 0.5
RICH ($10 \leq r \leq 105$ cm	9	
IRC ($7 \leq r \leq 12$ cm)	6 [$\approx$40]	≈ 3 [10]
LKR, Hodoscope ($12 \leq r \leq 120$ cm)	10 [5]	≈ 7 [2]
SAC (22×22 cm^2)	0.4 [1]	0.5 [1.5]

Table 3: Simulated muon halo rates in some critical detectors.

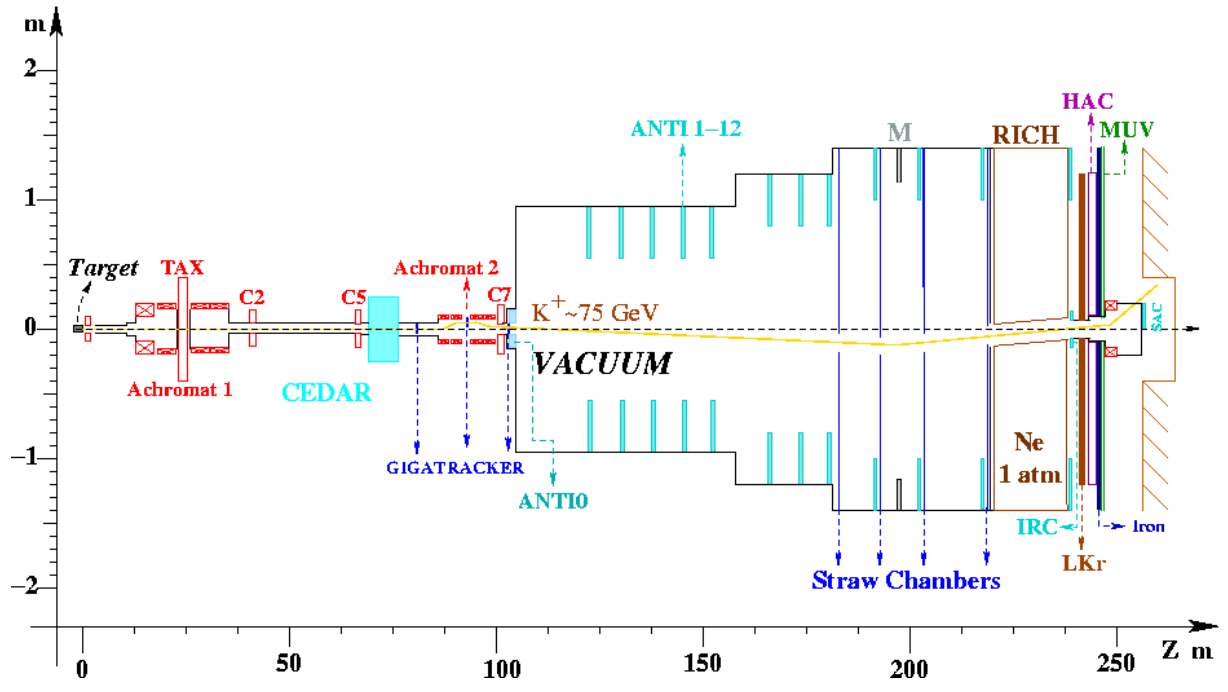

Figure 12: Conceptual layout of the $K^+ \to \pi^+ \nu\bar{\nu}$ experiment. ANTI refers to the Large Angle Vetoes (LAV) described in the text.

4. LAV

   A set of ring-shaped anti-counters surrounding the vacuum tank and providing full coverage for photons originating from the decay region with angles as large as 48 mr.

5. STRAW

   A magnetic spectrometer measuring the direction of the out-going pion and its momentum. Chambers of straw tubes are proposed as the tracking detector for their capability to operate in vacuum.

6. RICH

   A gas Ring Imaging Cherenkov counter providing muon/pion separation.

7. LKR

   The high-performance electromagnetic calorimeter built for the NA48 experiment acting as photon veto in the forward region.

8. MUD

   A hadron calorimeter and muon detector capable of identifying muons with very small inefficiencies.

9. IRC, SAC

   Intermediate ring and small angle photon veto calorimeters covering the angular regions around and in the beam.

6 GIGATRACKER Progress Report

6.1 Introduction

For the experiment, the beam spectrometer is a crucial detector which has to provide several precise measurements of beam particles: a) direction, b) momentum; c) timing. At the same time, it has to operate in a severe environment, the maximum beam particle intensity being ≈ 1.5 MHz/mm^2, corresponding to a total rate over the detector of almost 1 GHz, hence the name GigaTracKer (GTK). The detector is made of three silicon pixel stations placed along the beam line as sketched in Figure 13, where the layout of the system in the horizontal plane is shown. Each station covers an area of $(60(X) \times 27(Y))$mm^2, with the area split into $(300 \times 300)\mu$m^2 pixels 200 μm thick. The thickness represents a good compromise between

the material budget and the charge yield ($\approx$ 15000 electrons) when crossed by a relativistic particle. The required track time resolution is $\approx$ 150 ps (rms), which serves to separate close-in-time tracks with good efficiency. The stringent time resolution requires a design where the on-pixel front-end is optimized to enhance the time performances and obtain a time resolution of $\approx$ 200 ps/station (rms).

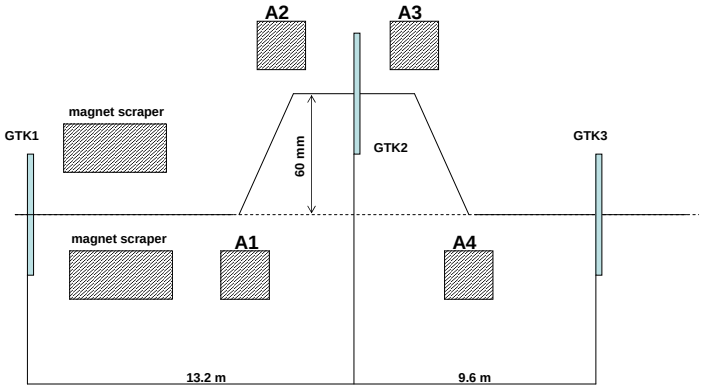

Figure 13: Layout of the Gigatracker.

With respect to the solution presented in the Proposal we have adopted a configuration which has several advantages:

- single detector type for all stations; the micromegas-based TPC has been dropped;
- all the stations are mounted in the vacuum tube;
- compact detector with transverse beam size designed to match realistic arrangement and dimensions of ASICs;
- established sensor technology based on p-in-n.

The new configuration has been studied with a simulation: tracks were followed through the detector and non-gaussian tails of the multiple scattering were considered. The excellent position resolution of the matrix of pixels results in a resolution on the track direction

of $\approx$ 14 μrad. Also the beam momentum measurement benefits from the track position resolution and the overall momentum uncertainty has been determined to be $\approx$ 0.2 %.
GTK information has to be combined with the downstream spectrometer measurements to reconstruct the squared missing mass, M^2_{miss}, of the event. M^2_{miss} depends primarily on the momenta and on the angle between the incoming and outgoing track directions.
According to the design rate, position and divergence of the beam, we simulated $K^+ \to \pi^+\pi^0$ decays. The match between the two prongs of the spectrometer, GTK and downstream, was then checked. The tracks were required to be reconstructed with a time difference within a window equal to $3 \times \sigma_t$, where $\sigma_t \approx 190$ ps was derived from the two independent measures of the beam and outgoing track time. Finally, the track spatial match was checked on the closest distance of approach (CDA) between the two tracks with a three-sigma cut, being $\sigma_{CDA} =$ 1.4 mm. The ratio S/B, where S is defined as the number of events correctly reconstructed and B the number of events reconstructed after picking up a wrong track due to pile-up or hit inefficiencies, was found to be $\approx$ 19. The value is quite similar to the configuration with a micromega-based TPC, which was originally chosen because of its thinner design. We conclude that the performances with this new configuration are not significantly spoiled with respect to the previous set-up.
The following sections are organized as follows. We discuss the system configuration parameters in Section 6.2, while in Section 6.3 we present the sensors and the flip chip bonding. The design of the on-detector electronics, the readout architecture and the DAQ concept are introduced in Section 6.4. The off-detector electronics is discussed in Section 6.5. The cooling requirements together with the mechanics are considered in Section 6.6. Finally Section 6.7 is devoted to the presentation of the road map of the system implementation. In the last section, human resources that will contribute to the project, an updated cost estimate and break-down amongst institutions is presented.

6.2 System configuration and parameters

The GTK consists of three stations, containing one hybrid pixel detector module each. The pixels have dimensions of 300 μm x 300 μm. The hit arrival time of a pixel cell is measured with a resolution of at least 200 ps in each station. A material budget of 0.5 % X_0 per station is targeted. For the on-detector system integration following parameters need to be optimized.

- Material budget in active beam area.

- Read-out chip size and active matrix size.
- Accessibility to power and I/O connections on the chip.
- Particle rate per pixel.
- Heat dissipation and cooling.

In order to minimize material budget in the active beam area the connections to the read-out chip are outside the area and are accessible only from one side of the chip only. The beam profile has been adapted in such manner that two adjacent read-out chips rows cover the beam area. Figure 14 and Figure 15 show the configuration.

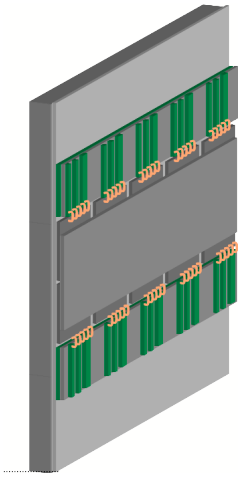

Figure 14: Configuration of Gigatracker.

The beam area of 60 mm $\times$ 27 mm is covered by one detector module containing two rows of five read-out chips bump bonded to one sensor element. The detector module is attached to a carbon fiber support structure. The dissipated heat produced by the 10 read-out chips is estimated to be 2 W/cm^2 for a total of 32 W. The heat transfer is established by the carbon fiber support to the outside of the beam area where cooling elements are located. Sharing the high particle flux at the beam centre with two rows of readout chips compared to a solution with three rows reduces the maximum particle rate seen by individual read-out chips, see Figure 16. Another aspect in the design of large pixel matrices, where power supply is provided from one side only, is the power drop along a column. For chips in 0.13 μm CMOS technology and a column length of 13.5 mm with a power consumption of 2W/cm^2 the metal planes layout has to be carefully considered: a first evaluation indicates that the solution with the power supply from one side is practicable.

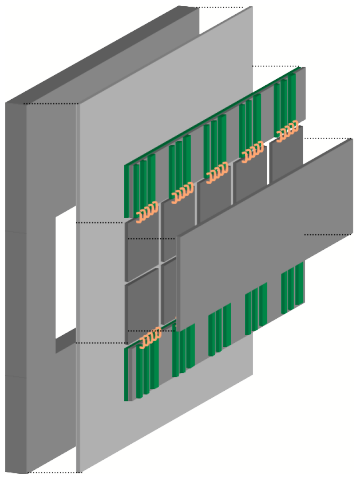

Figure 15: Configuration of Gigatracker (exploded view).

Sensors & Bonds	0.24 % X_0
R/O chip	0.11 % X_0
Support structure	0.10 % X_0
Total in beam	0.45 % X_0

Table 4: Material budget.

The thickness of the sensors is 200 μm and the thickness of the readout chips is 100 μm. In the presented configuration the material budget is uniform over the entire active area. Table 4 summarizes the material budget. The system parameters are listed in table 5.

6.3 Sensors and Flip Chip Bonding

In each GTK station one large sensor (60 mm $\times$ 27 mm) will be connected to 2 $\times$ 5 readout chips. The interconnection between the sensor and the readout chips will be made with Pb-Sn bump bonds.

6.3.1 Sensors

The size and choice of thickness of the detector were mainly governed by optimizing two main requirements for the detector:

- a low as possible material budget and
- sufficient signal to provide the necessary time resolution.

Number of stations	3
Number of pixels per station	18000
Number of pixel chips per station	2 rows x 5 columns
Number of pixels per chip	1800
Size of pixels	300 μm x 300 μm
Thickness of sensor	200 μm
Thickness of read-out chip	100 μm
Time resolution of GTK (rms)	150 ps
Time resolution of one station (rms)	200 ps
Input dynamic range	5000 - 60000 electrons
Particle rate per station	800 MHz
Average particle intensity per station	0.5 MHz/mm^2
Design particle rate per chip	130 MHz
Number of trigger levels	1
Latency	>1 μs up to 1 ms
Trigger window	$\geq$ 10 ns
Dead time due to read-out	1% (2% in beam centre)
Time stamp resolution per station	$<$ 200 ps (rms)
Total dose in 1 year	$\approx 10^5$ Gy
Material budget	0.5 % X_0 per station
Power dissipation per station	$\leq$ 2W/cm^2, 32 W
Operating temperature vacuum	< 0 ^{o}C

Table 5: GTK system parameter.

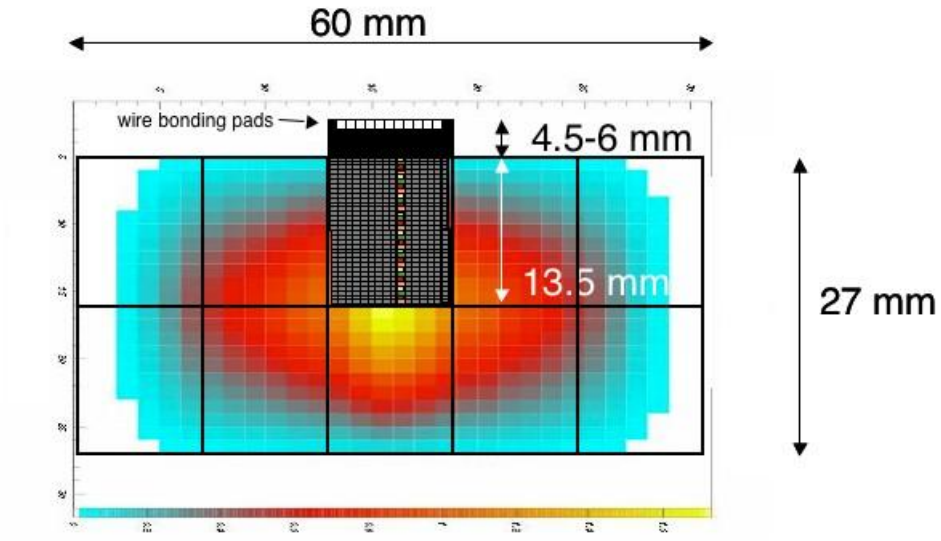

Figure 16: Beam profile with the arrangement of 2 × 5 chips showing active matrix size. One column shares high and low multiplicity regions.

As the aim for as low as possible material in the active beam area is orthogonal to the need for as much signal as possible provided by the sensor a compromise had to be found. Simulations showed that with a thickness of 200 μm a timing resolution of $\approx$ 200 ps [11] can be achieved. While at the same time 200 μm thick sensors present an acceptable addition to the material budget and allow to keep the overall budget per layer to $\approx 0.5\%$ X_0.
An important parameter which determines the choice and lifetime of the sensor is the operating environment. While the requirement for operation in vacuum will mainly need a careful study of the module design and cooling without substantial increase of the material budget, the radiation environment presents a severe challenge to the lifetime of the sensor. The expected fluence in 100 days of data taking (which corresponds to about one year of operation) is $\approx 2 \times 10^{14}$ 1 MeV neutrons cm^{-2} [12]. This is comparable to fluences in the LHC silicon strip trackers accumulated over a runtime of 10 years. In addition the beam distribution will be non-uniform across one sensor with a larger beam intensity in the central region [13]. A study was launched to investigate what sensor choices would be available and would comply with the GTK requirements.
Regarding the requirements for the electronic readout chips, i.e. the required time resolution of 200 ps, and the relative harsh radiation environment for the sensor the choice of a hybrid silicon detector was taken. This allows to separately optimise the individual components, chips and sensor respectively.

Comparing different silicon sensor technologies available for hybrid detectors two main trends have been identified: planar sensors and 3D sensors. While all current HEP experiments use planar sensors in various flavours, the 3D detectors promise to be a very interesting technology in the future, but are still in their infancy. The starting time for the NA62 experiment is foreseen to be in 2011. Therefore planar detectors were chosen as a mature baseline technology while still keeping a close look at the 3D development.
In order to achieve the required time resolution the sensor needs to be highly overdepleted to operate close to the charge carrier saturation velocity minimizing the charge collection time to 2-4 ns [14]. Collection times of this order are reached in 200 μm sensors when applying bias voltages of 400 V and more. An underdepleted operation is therefore excluded. The possibility of underdepleted operation in a high irradiation environment would have been the main advantage for choosing n-in-n detectors. However, the costs for these detectors are a factor 2 and more above the costs for p-in-n detectors as full double sided processing is used for the production. Taking these points into consideration a choice for p-in-n detectors was made.
The radiation will cause several defects in the sensor material which will lead to macroscopic changes:

- Increase of the leakage current
- Change of the depletion voltage
- Charge trapping and loss

A study has been carried out using prototype p-in-n diodes in order to determine the possible operation time of a GTK plane in the beam [15]. Several diodes were irradiated to different fluences between 10^{12} and 2×10^{14} 1 MeV n_{eq} cm^{-2}. The radiation induced damage effects were tested with standard I-V and C-V measurements as well as measuring the charge collection using a fast single channel preamplifier. In summary it seems possible to operate a GTK sensor up to a fluence of about 10^{14} if it can be cooled to 5° or less. The actual radiation induced leakage current presents the main limitation for operation at this stage. Further studies will require an investigation of the charge collection properties with a final readout chain. In the current baseline it is therefore foreseen to replace each GTK station after reaching a fluence of 10^{14} in the hot centre, which corresponds to a runtime of about 60 days under optimum beam conditions.
In Table 6.3.1 we present the main technology choices for the GTK sensor.

Sensor type	planar p-in-n
Thickness	200 μm
Active size	27 mm $\times$ 60 mm
Pixel size	300 μm $\times$ 300 μm

Table 6: Summary of the sensor parameters.

The regions in between chips will be covered by elongated pixels on the sensor to maintain the sensitive detector area over the full sensor size. As the GTK design foresees a relatively large sensor the measurements before flip chip bonding on the bare sensor have to be carefully evaluated. It has to be studied if the implementation of a bias-grid could facilitate the selection of good sensors and thus improve the production yield.

6.3.2 Flip Chip Bonding

The choice of a hybrid pixel system requires a high quality interconnection to connect each readout cell with one cell in the sensor. Previous experiences in LHC experiments have shown that such high yield interconnections can be established using either Indium or Pb-Sn bump bonds. Bump bonding yields in the production of better than 99.9% have been achieved [16]. In the present baseline it is foreseen to use Pb-Sn solder bump bonds.
In order to flip chip bond the individual chips to the sensor a matrix of bump bonds is deposited on each of the components. Typical bump sizes are in the order of 20-30 μm. The deposition is done using several sputtering, etching, and electroplating steps interleaved with photolithographic steps to exactly define the bump size and position. The bump deposition process has to be studied and optimized for the final components. The handling and processing of the thin components has to be investigated and the process flow has to be defined accordingly. Once the bumps have been defined the sensor and the chips are diced out of the wafer and the bumps are reflown in an oven. Finally the components are connected together using high precision alignment and positioning tools. Due to the difficult and delicate bumping and flip chipping process all operations have to be carried out in a high class cleanroom.
The thinning of the readout chips is an integral part of the flip chip processing. This operation can only be carried out during the flip chip processing in order not to endanger the bumping process due to external contaminations. The requirement of the GTK to have thinned chips with a target thickness of 100 μm explores new domains for hybrid silicon pixel detectors.

Current state of the art detectors have reached minimum chip thicknesses of 150 μm [16]. The internal stresses in the silicon have to be well understood in order not to compromise the bump bonding yield due to deformed chips. The target yield is 99.9% bump yield per chip. It has to be investigated at which point in the bumping process flow the thinning can be carried out and how eventual stresses can be compensated for.

6.4 On-detector electronics

6.4.1 Pixel chip architecture

Resulting from the above considerations an active pixel matrix of 13.5 mm x 12 mm in size with 45 rows $\times$ 40 columns of pixels with dimensions of 300 μm $\times$ 300 μm are foreseen, resulting in 1800 pixels per chip. The chip area outside the active beam area used for data processing and control is estimated to be in the order of 4.5 to 6 mm large resulting in a total chip size of 18 to 19.5 $\times$ 12 mm, see Figure 16. The communication to and from the pixel read-out chip is done via high speed differential signals. This reduces the number of connections and thus increases module reliability. The number of I/O pads is limited as the connections to the module are done on one side of the chip only, see Figure 16. A high number of single ended data lines would increase the digital system noise. On two high speed serial input lines the clock signal and the serial control signals are connected. On one slower serial input port and one parallel input port configuration data are transmitted. The data output ports consist of two 3 Gbit/s serial ports for the data and one slower serial port for status information. For test purposes 10 single ended outputs are foreseen. Figure 17 illustrates the I/Os of the chip.

The major challenges for the implementation of the pixel read-out chip are connected to the demanding objectives as to achieve the stringent time resolution, by the compensation of the associated time-walk and to cope with the high data rate within a tight power budget. The design and layout of the digital processing units must be done so that the digital noise has little effect on the analog front end. The implementation of the pixel read-out chip GTK is done in 0.13 μm CMOS technology. This technology is fully available and design tools have been provided. First studies indicate that the technology might be sufficiently radiation hard by itself for the expected total dose $\approx 10^5$ Gy/year [12][17][18]. However, further tests will show whether radiation hardening techniques need to be applied. Triplication of critical registers and nodes may be needed to avoid single event upset effects. The 130 nm has a relatively high substrate resistivity when compared to 250 nm technology. This makes

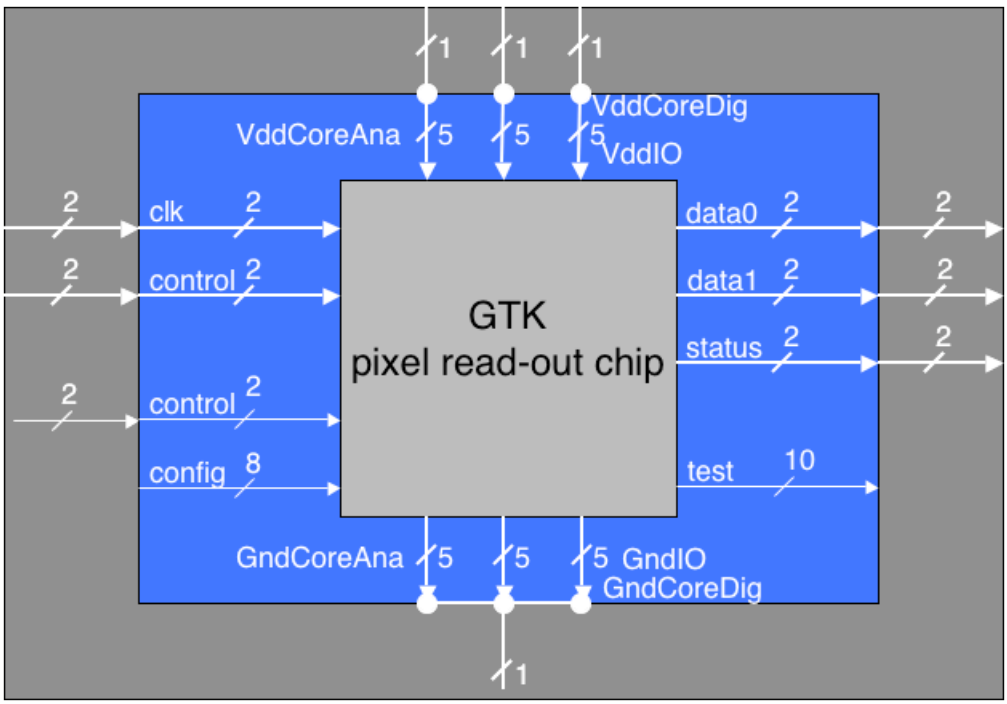

Figure 17: IO connection to the GTK pixel read-out chip.

it easier to insulate digital and analogue blocks by means of guard-rings. However, the high sensitivity and large bandwidth of analog front-end require techniques like differential circuit of noisy digital circuits and differential analog front-end. These tend to reduce both propagation of ground and substrate noise and to improve immunity of analog front-end.
The on-detector electronics of the Gigatracker has to meet challenging requirements such as:

- Input dynamic range: $5000 - 60000$ electrons
- Space resolution: 100 μm (rms)
- Time resolution: 200 ps (rms)
- Average data rate per square centimeter: ≈ 50 MHz/cm^2
- Power consumption ≤ 2W/cm^2

A comprehensive list of specifications can be seen in Table 5.
The space resolution allows for a relatively big pixel cell. A pixel size of 300 μm $\times$ 300 μm has been chosen, which results in ≈ 1000 cells per cm^2 and in a maximum power budget of 2mW/channel. This figure must however take into account also the dissipation of the chip

periphery and of the fast I/O devices. Combined together, the above specifications demand the design of a pixel read-out chip with unprecedented performance. Therefore, a vigorous $R\&D$ program is needed in order to select the optimal architecture. We have identified three critical $R\&D$ tasks that will be pursued in parallel:

- Design of a pixel-level front-end capable of 200 ps resolution
- Selection of the most appropriate technique for the time digitisation
- Study of digital read-out architecture

6.4.2 Design options

Basic front-end analogue building blocks have been designed and submitted beginning of 2007. The aim has been to test the functional performances as well as CMOS 0.13 μm technology parameters. The ASIC electrical performances have been investigated and the time resolution due to the jitter and time-walk contributions have been evaluated. In the following sub-sections we discuss the results obtained with the prototypes.

6.4.3 Time walk correction

With a dynamic range of 10 : 1 a standard leading edge discriminator will experience a time-walk incompatible with the required accuracy. Hence, a time-walk compensation has to be applied. Two alternatives are under consideration, namely the use of a low-power Constant Fraction Discriminator (CFD) and the correction via the Time over Threshold (ToT) method. Each solution has its unique advantages and disadvantages and only a study based on realistic demonstrators will allow the selection of the most appropriate solution.

A. Constant Fraction Discriminator

Constant fraction discriminator is the "analogue approach" to address the time-walk problem, since with this technique a precise timing pulse is obtained by means of analogue signal processing. A CFD has the advantage that it produces the time information with a single measurement, thereby reducing the data volume with respect to the ToT method. The challenge in case of the Gigatracker is to meet the precision of 200 ps (rms) within the given power budget, which is well below the one of a standard CFD. In a first $R\&D$ phase a CFD optimized for NA62 has been designed and implemented on silicon using a 0.13 μm CMOS technology. The test chip contains three channels, each formed by a charge sensitive amplifier and a CFD. Each channel dissipates 500 μW from a 1.2 V power supply, while

the power consumption of the CFD alone is 130 μW. Figure 18 shows preliminary results obtained from the electrical tests of the circuit. The jitter and the time walk are shown as a function of the number of electrons of the input signal for two preamplifier configurations: fast, corresponding to a shaping time of 3.5 ns (indicated as DF1CORR in figure 18) and slow, 5.5 ns shaping time (as DSCORR2 in figure 18). A peak-to-peak residual time walk of 270 ps is achieved with both configurations.

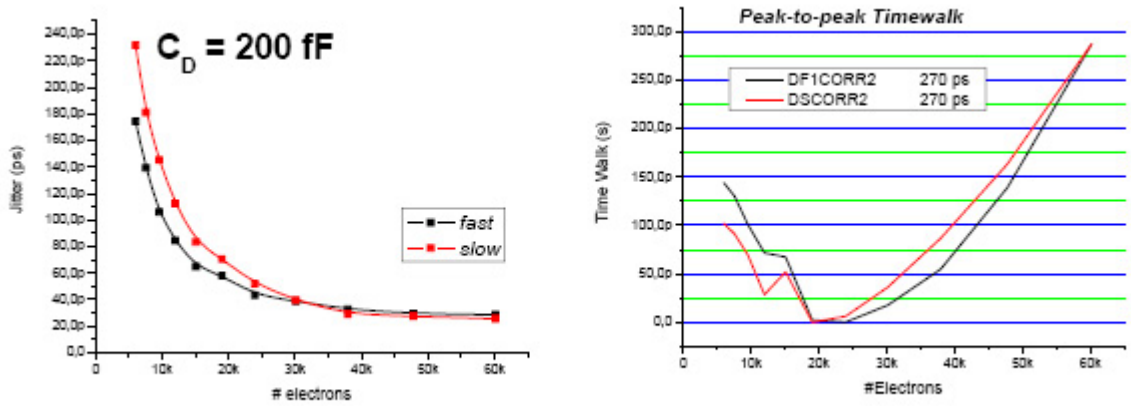

Figure 18: Jitter (left) and time walk (right) performances of the CFD prototype. Signals of different amplitude have been injected with on chip calibration lines. An on chip capacitance of 200 fF mimics the pixel parasitic capacitance.

Figure 19 reports the simulated resolution that would be obtained in case a Landau distribution is applied to the incoming signals. The convolution of the signal amplitude distribution, which is rather narrow, and the residual time walk results in a deviation of $\leq$ 100 ps.
Although these first results are quite promising it should be demonstrated that the performance of the CFD are not impaired when the circuit operates in a more realistic environment, where the interference introduced by the digital blocks will also be present. This can be studied only with a more complete demonstrator incorporating on board also a significant amount of logic cells.

B. Time over Threshold correction

The time walk correction is based on an algorithm derived from the correlation between the time over threshold (pulse width) and the experienced time walk. The correlation is found out from the measurement data of the prototype NINO [20]. The time walk vs. pulse width of the NINO prototype is presented in Figure 20. The points marked with diamonds

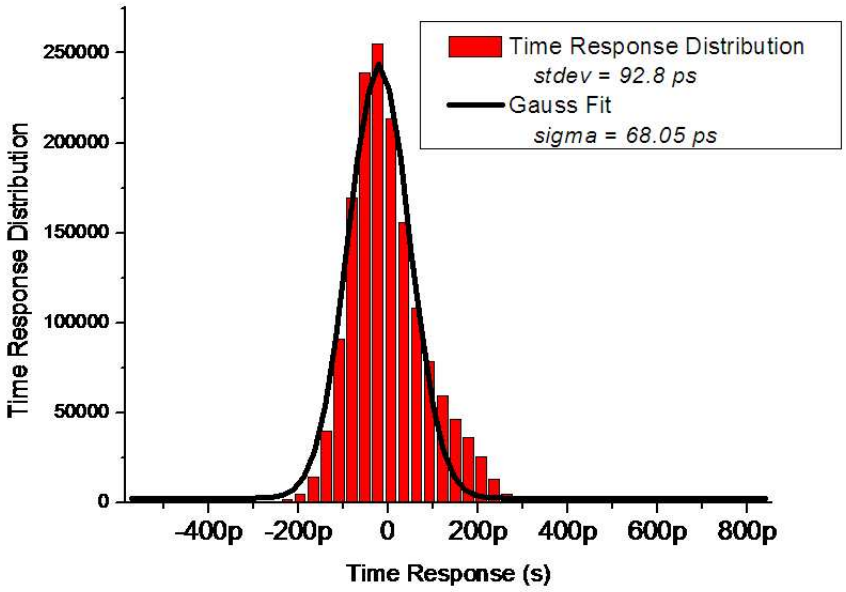

Figure 19: Simulated convolution of the CFD response with a Landau distribution

present the average time walk and the points marked with plus-signs present the peak-to-peak variation of the time walk, in other words the peak-to-peak jitter of the NINO. As seen from the plot, the average time walk is a nearly linear function of the pulse width.

The correlation defining the algorithm must be, however, verified with a setup corresponding to the real life situation in the Gigatracker. This means that measurements providing the data must be repeated with the pixel detector bump-bonded directly to the readout electronics, which must include the front end amplifier that is not implemented at this point.

Measuring the pulse width requires measuring time at two different instants per event, i.e. the rising edge crossing threshold and the falling edge crossing threshold. These time measurements are converted into a digital time stamp using a TDC. For this double time stamping (DTS) two sets of hit registers need to be used as shown in Figure 21: one triggered by the leading edge and the other by trailing edge, giving two digital words t1 and t2.

The time walk vs. signal time width correction algorithm can be implemented offline during the event processing. This solution, which increases the number of bits to be transmitted out from chip, would consent to determine the correlation and trace it as a function of time. Techniques, which allow on-chip time walk compensation, as digital logic or look-up table, are under investigation.

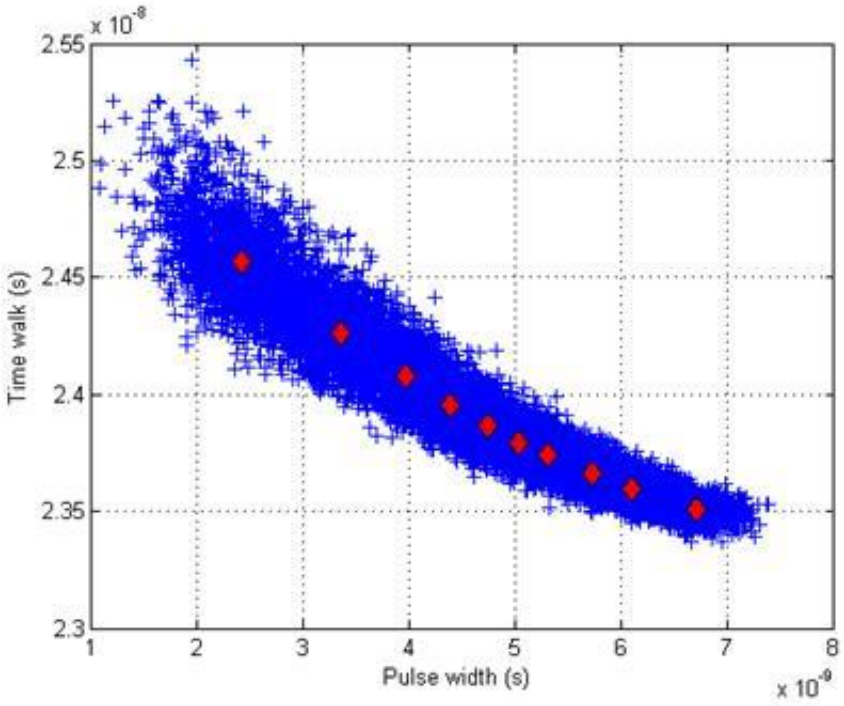

Figure 20: Plot of the time walk vs. pulse.

6.4.4 TDC options

In the chip a clock counter will provide a coarse time information. A fine measurement will be obtained with a Time to Digital Converter (TDC) measuring the time elapsed between the discriminator signal and the next clock edge. If the size of the time bin matches the required resolution (200 ps), the quantisation noise of the TDC will have a minor impact on the overall accuracy. The dynamic range of the TDC should span two clock cycles. This it useful to avoid ambiguities in associating the hit to one of two adjacent clock periods. If we suppose to use a master clock with a frequency of 100 MHz a 7 bit TDC is needed. TDCs can be implemented either using Time to Amplitude converters (TACs) or Delay Locked Loops (DLLs).
With the relatively big pixel size it is not excluded a priori that a TAC based TDC can be implemented on a pixel by pixel basis. This will have two advantages:

- the comparator signal does not need to be propagated outside the cell, thus avoiding the use of high power high speed digital driver in the pixel;
- most of the critical signal processing circuitry will be embedded in the pixel with an efficient use of the pixel area and design flexibility.

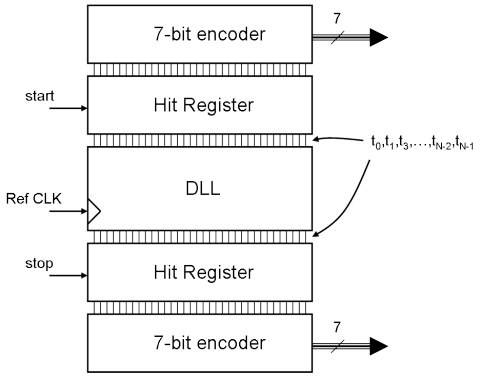

Figure 21: Block diagram of the double time stamp TDC.

Pixel address	11 bit
High precision time stamp 1	7 bit
High precision time stamp 2	7 bit (0 for CFD)
Low precision time stamp	7 bit
Total word length	32 (25)
Total data rate	4.2 (3.3) Gbit/s

Table 7: Data bits per hit

A TAC based TDC is however intrinsically slower than its DLL based counterpart. Therefore the latter will be the natural option if the TDC has to be shared among different pixels or if the Time over Threshold technique (that requires two measurements per each hit) will be selected.

6.4.5 Read-out architecture

The GTK chip is designed for the maximum particle rate in the centre of the beam. The maximum hit rate per centre chip is 130 MHz. The amount of data produced by one hit is summarised in Table 7.

In the option with the Time over Threshold discriminator two high precision measurements are performed whereas the constant fraction discriminator delivers only one measurement economizing 7 bits out of 32. A counter adds a low precision time stamp increasing the dynamic range to 1.28 μs for a 100 MHz master clock frequency.

Consequently, a total average data rate of 4.2 Gbit/s needs to be transferred and processed for each chip. Considering fluctuations in the data rate and to reduce the amount of on-chip

Nominal particle rates per	
Station	0.8 GHz
Centre chip	130 MHz
Centre column of pixels	3.3 MHz
Average pixel in centre column	73 kHz
Pixel in beam centre	140 kHz

Table 8: Hit rates

buffering the design parameter has been set to 6 Gbit/s. The NA62 experiment can deliver a trigger signal to the GTK not earlier than 1 μs and up to 1 ms. The trigger signal then points to a time window of 10 ns where the data hits are of interest and need to be extracted and stored. In a time span of 1 ms the average data amount accumulated in one read-out chip is 4.2 Mbit. The amount of logic required to store this amount of data would take a too large area. Resulting from these considerations a triggerless on-detector architecture where all hit data is sent off the chip has been adopted. The event selection is done in the off-detector electronics. The design of a link with 6 Gbit/s is extremely challenging even in a 0.13 μm CMOS technology. At least two 3 Gbit/s serial links will share the data load.

6.4.6 Particle and data rates

The pixel chips in the centre of the station are subject to the highest particle flux and resulting from that have to process the highest data rate. As all chips are designed identically the particle rates of the beam centre define the chip design specifications. The chip readout is organized in columns in order to average the pixel hit rate of cells close and far from the beam centre. The hit rate of the centre column of pixels is estimated to be 3.3 MHz or 80 MHz/cm^2. This results in an average pixel hit rate of 73 kHz for the centre column with a peak pixel hit rate in the centre of 140 kHz. Extrapolating the average column hit rate to the full chip results in a chip hit rate of 130 MHz, thus defining the chip design hit rate to 130 MHz. Table 8 summarizes the design rates.
The specification of chip data acquisition efficiency is 99 % for the overall beam area and 98 % for the very centre of the beam. In the option with the DLL based TDC the DLL provides a reference time stamp and several hit registers store the signal arrival time. However, one cannot afford to have one hit register per pixel cell but needs to multiplex a group of pixels to several hit registers. The number of pixels combined in one hit register is defined by the maximum accepted dead time or minimum acquisition efficiency of 99 % (98%). Calculations

and hardware description language based (VHDL) simulations have been performed to define the maximum number of pixels which can be multiplexed together for the DLL based TDC option. The time a pixel cell occupies the shared hit register depends on the discriminator signal and the number of timing measurements to take. In the option where the time walk is compensated by taking two measurements, as for the time-over-threshold, the pixel cells occupies the multiplexed TDC logic during the full input signal width.
The graph in Figure 22 shows the maximum number of pixels multiplexed together for a occupation times of 10 ns and 25 ns. For a hit rate of 80 MHz/cm^2, an occupation time of 10 ns and efficiencies of 99 (98) % , 20 (37) pixels can be multiplexed to the same hit register. This allows to merge half of the pixels of one column together and shows that the occupation time should be below 10 ns.

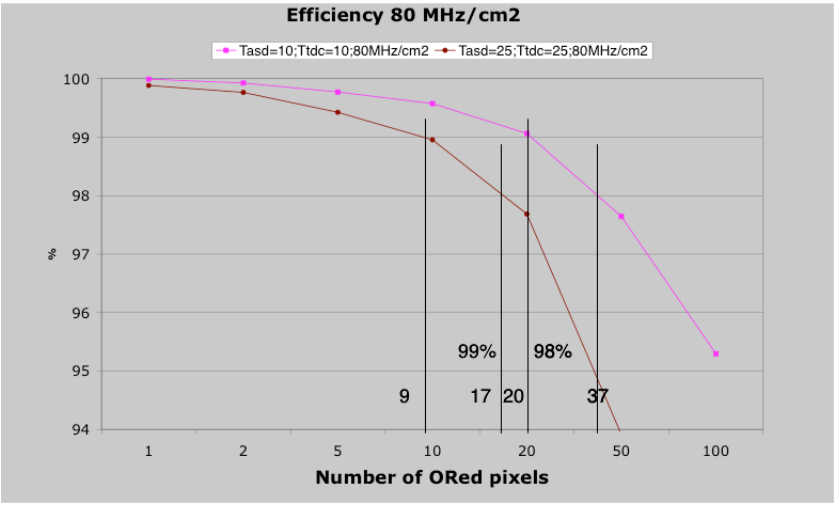

Figure 22: Acquisition efficiency for a hit rate of 80 MHz/cm^2 and occupation time of 10 ns and 25 ns. For 10 ns and an efficiency of 99 (98) % 20 (37) pixels can be multiplexed together.

For the option where each pixel cell has its own TDC, the conversion delay and the delay until the pixel hit time is read out needs to be taken into account for the calculation of the efficiency. During this time the corresponding pixel cannot record a second hit. The graph in Figure 23 gives the maximum allowed dead time per pixel of 80ns (200ns) for an efficiency of 99 (98) % for the centre pixel data rate of 150 MHz/cm^2.

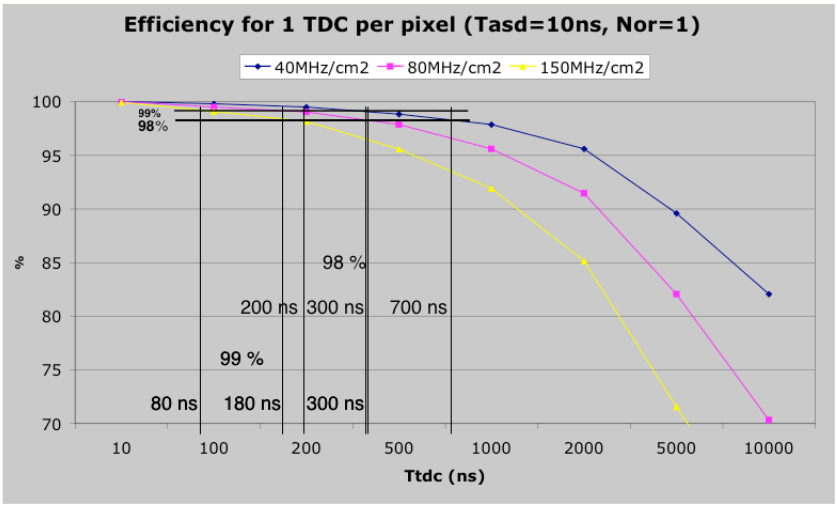

Figure 23: Efficiency over dead time of the TDC and pixel cell read-out.

Figure 24 shows a block diagram of the read-out architecture for the DLL based TDC. The hit information from the discriminators is sent to a merging logic and forwards the timing signals to the TDC hit registers and stores the address of the hit pixel. Then the hit registers send the information to the serialisation stage where buffering and multiplexing of all combined pixels takes place. In the option of a dedicated TDC per pixel the read-out architecture is similar. A round-robin based arbitration logic reads the hit information, time and address, for each column and forwards it to the serialisation stage.

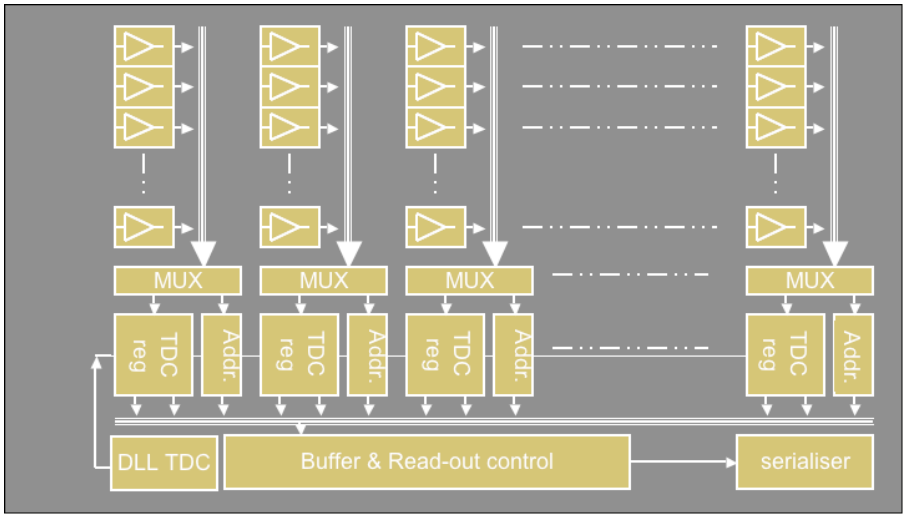

Figure 24: Read-out architecture for the DLL based TDC option.

6.4.7 Communication and power connection to the module

Figure 14 and Figure 15 show the module configuration. The chips have their wire bonding connections on the top and bottom border outside the active beam area. The chip pads are wire bonded to a pitch adapter which routes the signals some 20 cm to a radiation protected area. There the high speed serial signals, are converted from/to optical signals and routed to the control room. Each chip has as inputs from the control room, the clock, serial control, configuration signals, and as outputs the two data output signals and the status signals, resulting in 3 input and 3 output serial optical links to each chip. Parallel configuration ports are used to set modes locally hardwired, such as the operation modes but also the chip identification number. No copper connection to the module is foreseen. The clock line of one module is common to all chips in a module, whereas all other links are dedicated point-to-point connections. In total, each module has 21 input serial optical links and 30

Links	Speed	Number of links for GTK	Direction
Clock	100 Mbit/s	3	In
Control	100 Mbit/s	30	In
Configuration	100 Mbit/s	30	In
Data0	3 Gbit/s	30	Out
Data1	3 Gbit/s	30	Out
Status	100 Mbit/s	30	Out

Table 9: Hit rates.

output serial optical links. Thus, the full GTK needs 63 input links and 90 output links. Table 9 summarizes the links for the GTK.

The optical transmission system can be built up using commercial transmitters, receivers and optical fibers as they are located in a non-radiated environment. Multi channel transceivers are available such as illustrated in Figure 25. Another option is the link chip set of the Multi-Gigabit-Transmission System, GBT, which is currently under study and development and allows transmission of up to 3.36 Gbit/s in radiated environment [21]. However, it is not clear whether the time scale of this development fits the GTK needs.

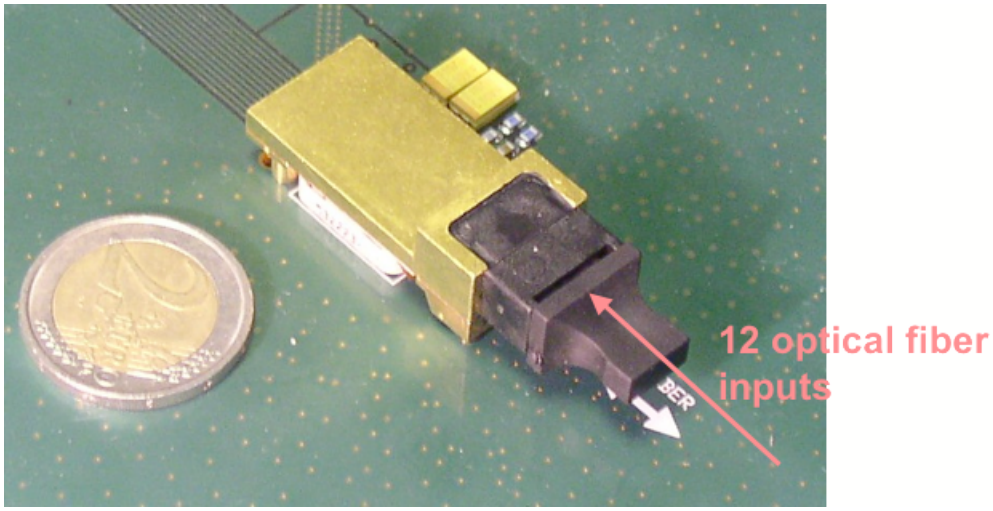

Figure 25: 12-channel optical input module (Zarlink).

The power connection to the chips is done via the pitch adapter. Each chip receives separate power lines with sense wires connected very close to the bond wire connections. Regulators are mounted on the pitch adapter and are connected to remote power supplies. As the on-detector electronics has a small thermal inertia and any cooling defect will heat up and

possibly destroy the module temperature sensors are integrated in the read-out chip and the temperature is constantly monitored using hardware based circuits allowing to cut the power immediately. As power dissipation is an issue it will be studied whether the on-detector electronics or parts of it can be powered down during the spill-off time (2 seconds beam, 12 seconds no beam).

6.5 Off-detector electronics

The on-chip electronics provides all registered hits on ninety 3-Gbit/s optical fibers. The off-detector electronics receives and stores this information during the trigger latency, which is currently not fully defined yet, but can be as long as 1 ms. Upon reception of a positive trigger signal the electronics selects all hits within a programmable time window of about 10 ns and forwards the retained hits to the DAQ. Hardware based online monitoring routines verify the proper behaviour of the detector. The system is built up using FPGA based hardware processors.

Recently several multi-channel multi-gigabit optical receiver systems connected to powerful FPGA processors for the LHC experiments have been developed. Multi-channel optical receivers allow to receive all 90 optical links on one single system. Compact FPGA processors based on bus systems using either daughter card connections or high speed serial back plane connections, such as ATCA or MTCA [22] establish the connection between processing cards and the PC.

6.6 Mechanics and cooling

The fluence at the Gigatracker stations is expected to reach 2×10^{14} 1 MeV neutron equivalent and generates adverse effects on the silicon sensors characteristics [12]. In order to prevent thermal runaway due to the increase in the induced leakage, the sensors, operating in high vacuum, should be kept at low temperature, in any case not higher than a few degrees above 0 ^{0}C. This requires an efficient cooling system, which however must be very low mass in order to avoid degradation in the performance and efficiency of the detector.

To meet these requirements, a cooling concept is being developed in which the cooling circuit will be placed at the edges of a low mass heat sink to which the detector active devices will be attached. The study is focused on very thin, high thermal conductivity substrates ($\approx 100\mu$m of K1,100 carbon fibres), or equivalent material, combined with the most efficient thermal interface material (thermal grease).

Following a very preliminary estimate, a detailed calculation has been carried out based on a realistic model of the pixel planes, using a specific finite-element thermal calculation tool [19]. Figure 26 shows the thermal profile across the detector for several types of substrate and thermal interfaces.

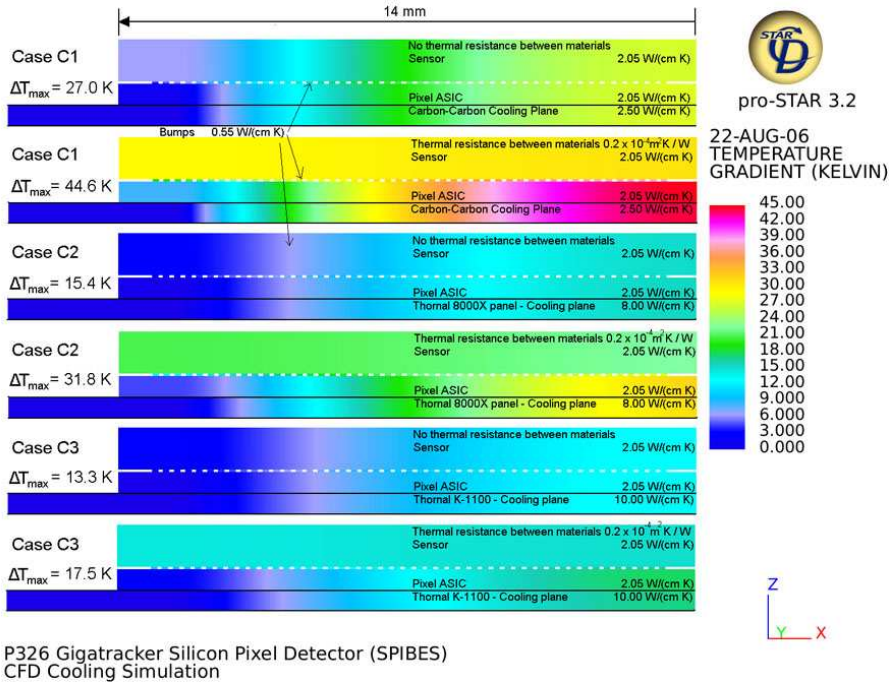

Figure 26: Thermal profiles for different temperature end-points and detector configurations.

These simulations show that satisfactory operating conditions can in principle be achieved by a proper choice of the materials. However, the results rely on certain assumptions and strongly depend on the real properties and the quality of the assembly. An experimental verification with realistic prototypes is indispensable.

6.7 Plans for developments towards detector construction

The plan outlined in this section is still preliminary; the evaluation of the technical issues and the estimate of the manpower needs are based on previous experience with pixel detector systems and are considered to be realistic.

6.7.1 Sensors

In the initial stage the overall design of the sensor will be finalized. This includes in particular the configuration of the guard-rings, the possible implementation of a bias grid and the layout of the backside aluminium metalisation. Openings in the Al backside will allow to carry out laser tests on final modules. However, these opening will also be more prone to contamination and scratches which would decrease the sensor quality. A very important issue for bump bonding is the planarity of a full size sensor. In the prototype production an optimisation of the process has already been introduced to provide wafer bows below 30 microns. On the final sensor wafer mask, it is foreseen to implement test structures which match the demonstrator chip design. This will allow to connect individual demonstrator chips to single sensors of the same size. These demonstrators will be evaluated with test pulses, radioactive sources and particle beams. The evaluation will be repeated after irradiation to verify the compliance of charge collection properties with the requirements.

6.7.2 Flip-Chip Bonding

A four-phase program has been defined for the *R&D* work programme leading to the first demonstrator modules. It is currently under discussion with the bump boding supplier. It is foreseen to investigate the thinning and flip-chip bonding of the modules in different stages, decoupling as much as possible the thinning from the bump deposition part. It also includes the investigation on how to connect demonstrator chips to single sensors. An important point is that the demonstrator chips will be diced out individually from MPW wafers; the bump deposition and bonding process will be different from the one eventually adopted with full wafers. Once full size and final readout wafers and sensor wafers will be available a final evaluation of the process ow will be necessary.

6.7.3 System implementation

Prototypes of the building blocks in the front-end chain including the pre-amplifier, discriminator, TDC, serializer and high speed output drivers are used to qualify the best option for the discriminator and TDC, to prove the robustness against noise and to prove the proper functionality concerning time resolution and power drop. Noise generators on the chip will be used to qualify the front-end in a more realistic environment. A sub matrix of 8 times 8 cells of the final pixel chip will be produced and connected to a sensor element. The full detector chain, including the read-out architecture, the analog front-end and the cross-talk robust-

ness, will be qualified. Already at this stage sophisticated off-detector electronics processors will be built up to analyse the data. Tests with on-chip test pulsers, radiation sources and a test beam will qualify the system. In the last step the full matrix will be implemented in the chip. Assemblies of one single chip and full 10-chip modules will be qualified. At the same time the full system including off-detector electronics, cooling, mechanics, services and cabling will be designed and built.

6.7.4 Mechanics and cooling

To expedite the thermal study without waiting for the pixel readout chip to be available, it is planned to investigate the case of a detector array, of approximately 20 cm^2 area, made out of ALICE pixel ladders. The on-chip power dissipation of 1 W/cm^2 is sufficiently close to the one anticipated for the Gigatracker chip. The configuration of the ladders is well suited for all electrical and thermal measurements. The aim is to determine the most effective choice of the base components and of the assembly procedure. The active devices are available, so the development work can be focused on the substrate and thermal interface issues.

6.8 Human resources, timescale and costs

Timescale and costs are presented in Table 10, while the requested human resources are reported in Table 11. The human resources, quoted in Full Time Equivalent (FTE) units, are meant for the whole project and should be found on a 50% - 50% basis within CERN and INFN groups. Time charts are based on the experience gained in other pixel detector projects, whilst the cost profile relies on the current engineering prices.

year	**2007**	**2008**	**2009**	**2010**	**2011**	**Integral**
	kCHF	**kCHF**	**kCHF**	**kCHF**	**kCHF**	**kCHF**
FE ELECTRONICS						
CMOS 0.13μm						
prototypes MPW	18	200				
pixel ASIC						
engimeering run(s)			600	600		
pixel ASIC						
production run					150	
CMOS 0.13μm subtotal	**18**	**200**	**600**	**600**	**150**	**1.568**
SENSORS						
(including radiation test & prototypes)	**5**	**30**	**30**	**5**		**70**
BUMP BONDING						
(including test & prototypes)		**40**	**80**	**110**	**80**	**310**
INTERCONNECTS						
(MCM-hybrids)		**10**	**20**	**60**	**40**	**130**
TEST R/O CHAINS	**5**	**20**	**20**	**20**		**65**
OPTICAL LINKS		**20**	**40**	**50**	**40**	**150**
BACK-END ELECTRONICS		**15**	**35**	**80**	**70**	**200**
LV and HV						
POWER SUPPLIES+CABLES		**10**	**20**	**30**	**30**	**90**
SUPPORT and COOLING		**20**	**20**	**70**	**40**	**150**
MECHANICS/VACUUM		**10**	**20**	**70**	**40**	**140**
CONTINGENCY		**10**	**25**	**25**	**10**	**70**
OVERALL TOTAL	**28**	**385**	**910**	**1.120**	**500**	**2.943**
FUNDING REQUESTS						
(kCHF, EURO/CHF = 1.56)						
INFN	**28**	**131**	**408**	**626**	**214**	**1.407**
INFN (kEURO)	18	84	262	401	137	902
CERN		**254**	**502**	**494**	**286**	**1.536**

Table 10: Estimate of cost and spending profile for the Gigatracker based on current engineering run prices.

2007	2008	2009	2010	2011
7.8	**12.5**	**13.8**	**14.8**	**15**

Table 11: Profile of the human resources (FTE).

7 Photon Vetoes Inefficiency Requirements

The layout presented in the proposal has been changed from 13 to 12 large angle photon veto (LAV) rings, with internal and external radii adjusted to use the OPAL lead glass modules as will be described in Section 8.1. In addition only one IRC is proposed, to be used around the calorimeter beam pipe. The SAC will be mounted at the far end with a horizontal displacement in such a way that it is not hit by the undecayed beam particles. The simulation of the global inefficiency to the π^0 from $K^+ \to \pi^+\pi^0$, as was described in the proposal, has been run again to validate the new layout. Additional investigations have been made to identify the most critical detectors and energy ranges.
The following points should be noted:

- The cut on the charged pion momentum is between 15 and 35 GeV.
- After having applied a cut on the longitudinal coordinate of the decay vertex and the cut on the charged pion momentum, the fraction of $\pi^+\pi^0$ with two photons in the forward direction both within the LKR calorimeter acceptance is 82%.
- In all the remaining 18% of the events, the photon with the highest energy hits the LKR calorimeter while the other photon, in 98.9% of the cases, hits the LAV. As a consequence, with the chosen LAV geometrical coverage (which cannot easily be extended and is essentially independent of the active detection medium), in a fraction of 0.2% of the π^0 from $K^+ \to \pi^+\pi^0$ only the high energy photon can be detected.

The inefficiency for the detection of the photon hitting the LAV for different possible choices has been extensively studied with direct measuments and MC simulation. It is in any case sufficiently small as to add only a fraction (10%-20%) to the purely geometrical inefficiency quoted above. The energy spectrum of the forward photon is shown in Figure 27, as a scatter plot of the distance of the photon to the charged pion impact point on the calorimeter versus the energy of the photon. Assuming that the this photon is detected with e.g. 10^{-5} inefficiency, vetoing any gamma will allow a rejection at the level of $2 \cdot 10^{-8}$.
Most probably, to keep the inefficiency of the gamma detection in the LKR calorimeter at 10^{-5} or lower, a cut on the distance of the gamma from the charged pion in the calorimeter should be done to avoid the effect of cluster fusion. A cut at a distance of 10 cm will deteriorate the global inefficiency by a factor of about two, adding about 0.2% more inefficient events. However a careful study of the two clusters involved will most likely allow to improve the γ detection efficiency. Figure 28 shows the dependence between the energy and

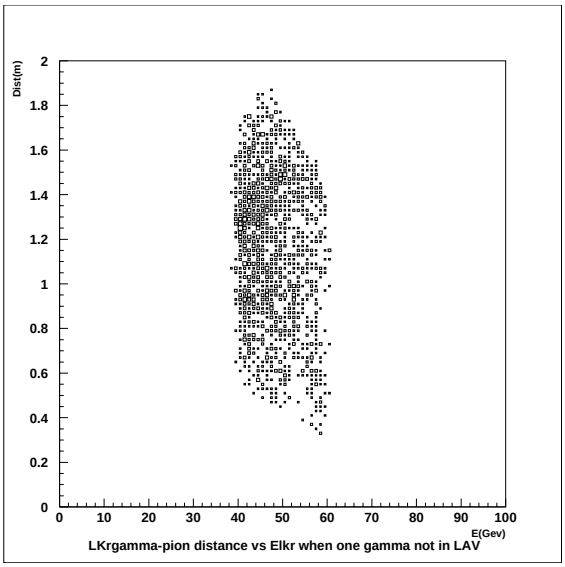

Figure 27: $\pi^+ - \gamma$ distance vs. energy when one photon misses the LAV.

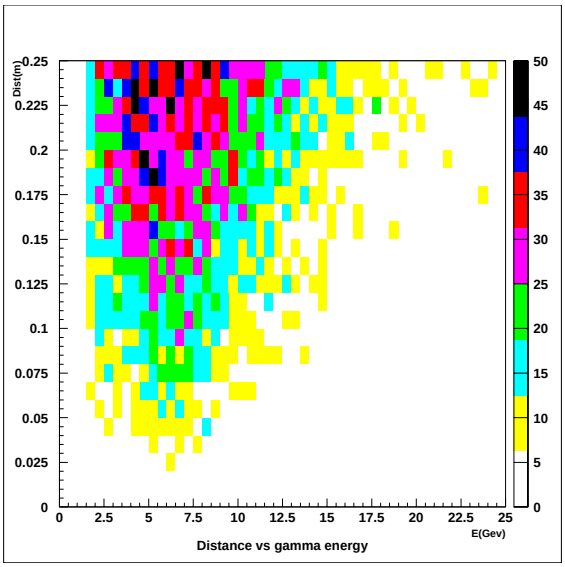

Figure 28: $\pi^+ - \gamma$ distance vs. energy when the two photons are in the LKR calorimeter.

the distance of the charged pion to the closer photon. Figure 29 and 30 show the energy distribution of the energy of the near and the far photon, respectively, for a distance cut of 10 cm. The fraction of inefficient events due to the distance has been found to be linear as as function of energy in the range of interest (Figure 31).

The updated data with the global inefficiencies are shown in Table 12. "Realistic" and "optimistic" parametrisation refer to the definition in the proposal. Additional rows show the result using the results of the tests for the parametrisation of the inefficiency of the LAV and of the LKR. For these results, the cut on the distance to the charged pion is not applied.

8 Large Angle Vetoes (LAV)

8.1 Test of prototypes for the choice of the technology

The original proposal presented two technologies for the construction of the large angle vetoes: lead/scintillator tiles with WLS readout and lead/scintillating fiber sandwich. For these, construction and procurement of existing prototypes started in 2006. Meanwhile, lead glass modules used in the OPAL experiment were made available to the Collaboration and they have been included in our test plans.

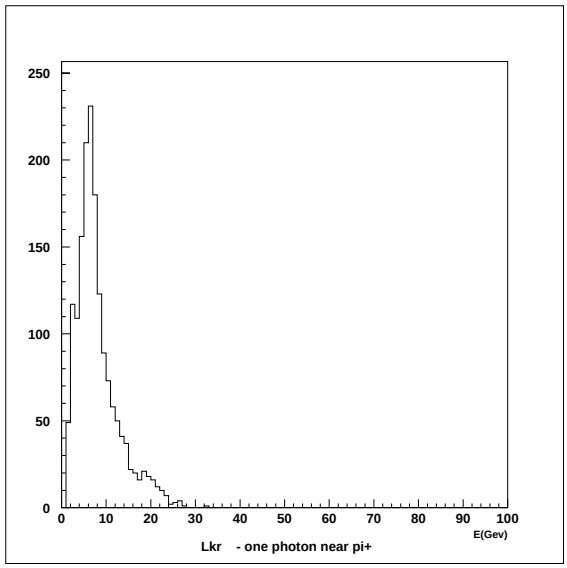

Figure 29: Energy of the gamma closer than 10 cm to the charged pion.

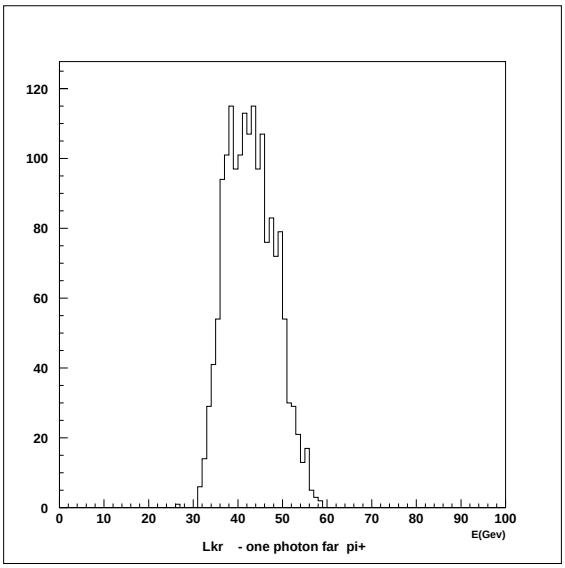

Figure 30: Energy of the other gamma farther than 10 cm from the charged pion.

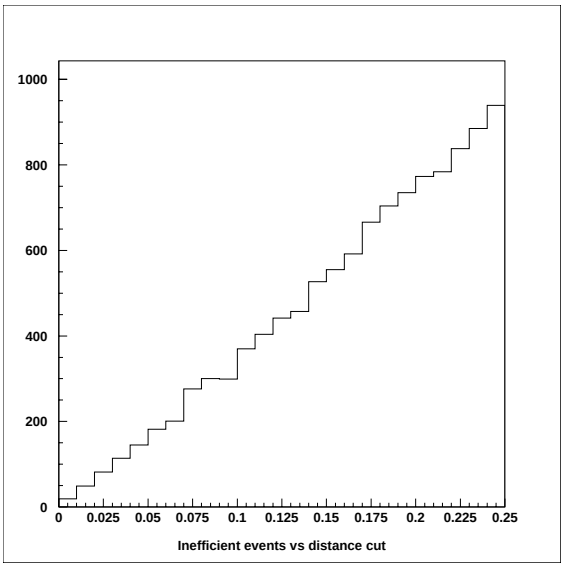

Figure 31: Number of inefficient events vs. $\pi^+ - \gamma$ distance.

	Average inefficiency	Fraction of ineff. events
Realistic choice		
Without pion momentum cut	$1.0 \cdot 10^{-7}$	1.00%
With pion momentum cut	$2.8 \cdot 10^{-8}$	0.28%
Optimistic choice		
Without pion momentum cut	$0.9 \cdot 10^{-8}$	0.89%
With pion momentum cut	$2.2 \cdot 10^{-9}$	0.20%
Using the results of the tests		
Without pion momentum cut	$1.6 \cdot 10^{-7}$	0.89%
With pion momentum cut	$1.7 \cdot 10^{-8}$	0.20%

Table 12: Total average inefficiencies.

- **Tile prototype:** A possible design consists of a sandwich of lead sheets and scintillating tiles with WLS fiber readout. An assembly of 16 wedge-shaped modules forms the veto counter. An example of such a detector, using 80 layers of 1-mm thick lead sheets and 5-mm thick scintillating tiles, was designed for the (now canceled) CKM experiment at Fermilab. Tests at the Jefferson Lab showed that the inefficiency of the detector for 1.2 GeV electrons was at most $3 \cdot 10^{-6}$ [23].

- **Fiber prototype:** Another solution is based on the design of the KLOE calorimeter [24] and consists of 1-mm diameter scintillating fibers sandwiched between 0.5-mm thick lead foils. The fibers are arranged orthogonally to the direction of particle incidence and are read out at both ends. Two U-shaped modules form a veto station.

- **Lead glass modules:** The third option is to use the lead glass modules already used in the barrel of the OPAL calorimeter [25] and which could be available in more than sufficient quantity. Each block is a kind of truncated pyramid with a height of 37 cm and with trapezoidal bases of about 11 $\times$ 11 cm. A 4-cm long light guide couples the lead glass block to a Hamamatsu R2238 photomultiplier.

In order to determine the best choice in terms of detection inefficiency, we loaned from Fermilab the CKM prototype, we tested a few of the OPAL lead glass blocks and we built a lead-fiber prototype.

8.2 The lead-fiber prototype

One U-shaped module was built in Frascati in 2006. The inner radius (60 cm) and length (310 cm along the inner face) are similar to the specifications for one of the upstream veto stations. The prototype has a radial thickness of 12.5 cm, about a third of the final one, but sufficient for the transverse containment of low-energy electron showers incident along the centre line of the module. Layers of the module were constructed by rolling 1-mm grooves into 0.5-mm lead foils and gluing scintillating fibers into the grooves. The longitudinal depth of the module is determined by the width (25 cm) of the lead foils. The desired radial thickness was obtained by stacking 99 layers. The ends of the module were milled and then fitted with light guides, with a segmentation in the plane transverse to the fibers of six cells along the depth and three along the radius. In the region covered by the last two cells in depth, scintillating fibers in alternating grooves were replaced by lead wires, in order to have a lower fiber density at the back of the detector, without needing complicated modifications to the lead-foil grooving machine.

8.3 The tests

The three prototypes were tested at the Frascati Beam Test Facility. This is an electron transfer line leading off the DAΦNE linac. It can provide electrons or positrons, in 10-ns pulses with a repetition rate of 50 Hz, with $50MeV < E < 750MeV$ and mean multiplicities from < 1 to 10^4 per pulse.

A "tagging system" has been built to define without ambiguity the arrival of an electron on the device to be tested. It is composed of two beam profile measuring devices, two tagging counters to define the beam and two veto counters (scintillators with a hole inside), mounted on the same support and well aligned along the beam axis. The tagging efficiency of this system varies with the momentum; the global tagging efficiency for 1-electron events depends also on the Poissonian probability to have one electron in the beam. Figure 32 shows the effect of the tagging: out of all events with different multiplicities, the loose selection (with only the two defining counters) is shown in red and the tight, final one, using also the vetoes, is plotted in black.

Table 13 gives the total statistics obtained in the June-July 2007 run. For the fiber prototype, a complete energy calibration has been performed and the results are final, whereas for the other two solutions, analysis is ongoing and the results shown are still preliminary.

The determination of the inefficiency was done looking for tagged events with an energy

	Energy	P(1e-)	Eff. (tag*1e-)	Tagged Events	Ineff. Events	Inefficiency
Fiber prototype	200 MeV	31.3%	2.5%	68829	5	$7.3^{+4.1}_{-3.3} \cdot 10^{-5}$
	350 MeV	33.0%	9.2%	207385	3	$1.4^{+1.1}_{-0.9} \cdot 10^{-5}$
	500 MeV	33.3%	14.3%	371633	1	$2.7^{+4.7}_{-1.7} \cdot 10^{-6}$
CKM prototype	200 MeV	29.5%	3.7%	65165	2	$3.1^{+3.1}_{-1.5} \cdot 10^{-5}$
	350 MeV	31.8%	8.8%	221162	3	$1.4^{+1.0}_{-0.6} \cdot 10^{-5}$
	500 MeV	29.0%	17.6%	192412	1	$5.2^{+0.8}_{-3.2} \cdot 10^{-6}$
Lead Glass	200 MeV	30.2%	3.9%	25069	3	$12.0^{+9.2}_{-5.2} \cdot 10^{-5}$
	500 MeV	26.0%	17.1%	91511	1	$1.1^{+1.8}_{-0.7} \cdot 10^{-5}$

Table 13: Statistics accumulated in the June-July 2007 run.

deposit less than 50 MeV, which were declared inefficient. Table 13 shows the numbers of inefficient events and the preliminary results for the inefficiency to electrons. Figure 33 summarizes these results. All three solutions give a value for the inefficiency below the requirements for the P-326 Large Angle Veto system [26].

8.4 The baseline design

As the results of the tests showed comparable performances for the three technologies, we then selected the less expensive solution for the baseline design, namely the lead glass one. We are now engaged in a test with cosmic rays of a suitable number of OPAL blocks (≈ 40) to verify the uniformity of the response and the quality of the available stock. Additional work is continuing to simulate the baseline design, using the data collected in the summer for validation, to evaluate the effect of punch-through and photonuclear reactions.

Each one of the OPAL counters is a truncated pyramid of SF57 glass, with trapezoidal bases of 11 $\times$ 11 cm and a length of 37 cm. A steel flange, with holes for fixation, is attached to one of the bases. Through a 8.5 cm diameter hole a lead glass light guide couples the bulk of the glass to the photomultiplier (Hamamatsu R2238). All the elements are glued together and the PM is equipped with its base and a mu-metal screen. A sketch of the single counter is shown in Figure 35.

A test to evaluate the effect of the radiation on the transparency of the blocks has been performed during 2007. A measurement of the transparency as a function of wavelength was

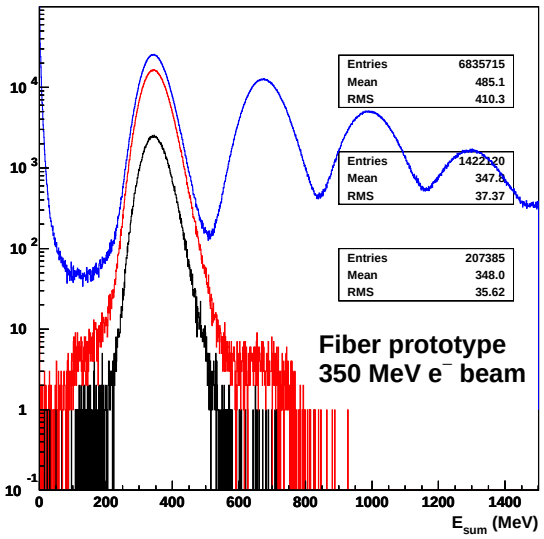

Figure 32: Effect of the tagging system.

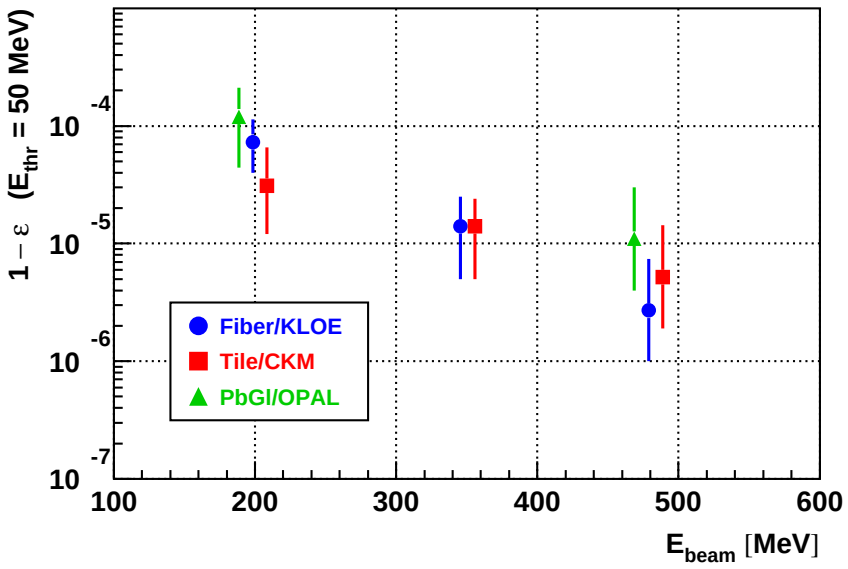

Figure 33: Inefficiency vs. energy for the three solutions.

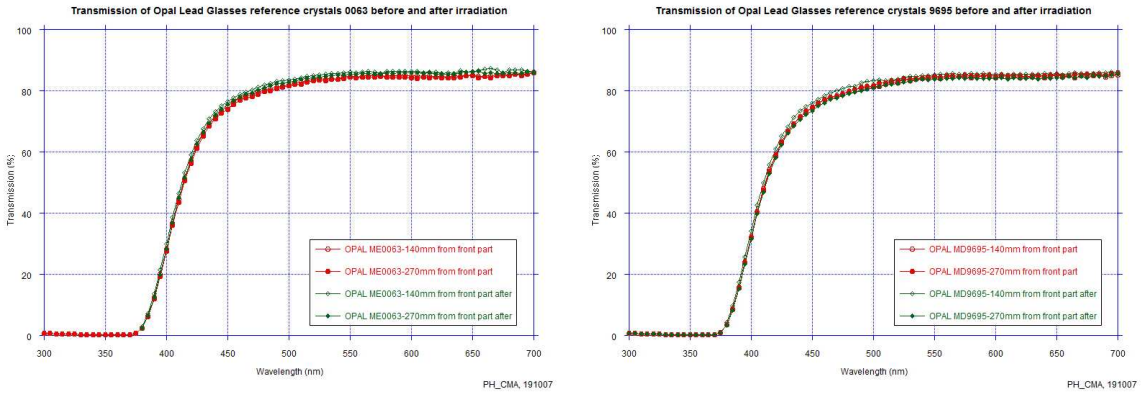

Figure 34: Results from the transparency measurement of the irradiated lead glass blocks.

first performed in May on three blocks, of which two have been installed around the upstream part of the K12 beam line, together with radiation monitors. They were measured again after four months of the 2007 run and no change in the transparency was found (Figure 34). The 2007 exposure time corresponds (in terms of number of protons on target) to about 0.4 years of future running. One block was installed in a position which is close to where the first large angle veto ring will be placed. The measured dose here was $\approx$ 26 mGy of neutrons and $\approx$ 20 mGy of other particles, mainly muons. A calculation of the muon dose in one year of the future experiment at that position yields $\approx$ 50 mGy which confirms the 0.4 year of a future run. Another block was mounted upstream of a concrete wall where the dose was measured to be $\approx$ 416 mGy of neutrons and $\approx$ 110 mGy of other particles. This block was thus irradiated with the equivalent of $\approx$ 6 years of running for neutrons and of $\approx$ 2 years for muons. These measurements leave us confident that radiation damage to the lead glass should not be an issue.

8.4.1 Mechanical design

Counters will be mounted in each ring with a radial orientation. As the inner radius of curvature of the blocks is not matched to the radius of the rings, several layers of blokcs will be used. As an example, the first five rings, with an inner radius of 53 cm, will be composed of five layers, 32 blocks each. Each layer is shifted by a fifth of the angle between two blocks in order to have complete hermeticity at least with three blocks ($20X_0$). In Figure 36 we show a conceptual sketch for the mechanical layout of the blocks. The structure will be installed in appropriate new sections of the decay tube, machined and polished internally,

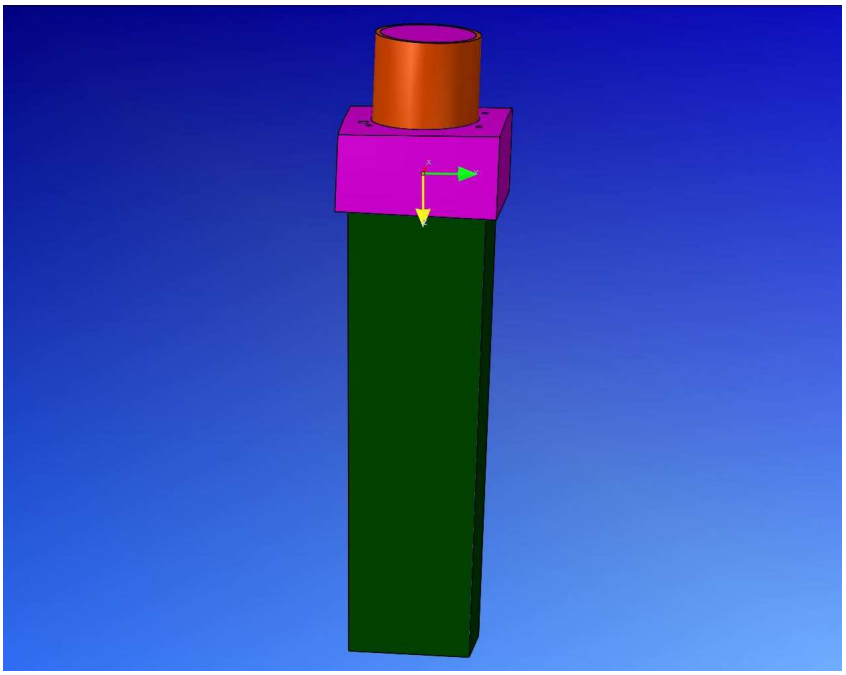

Figure 35: A single OPAL lead glass counter

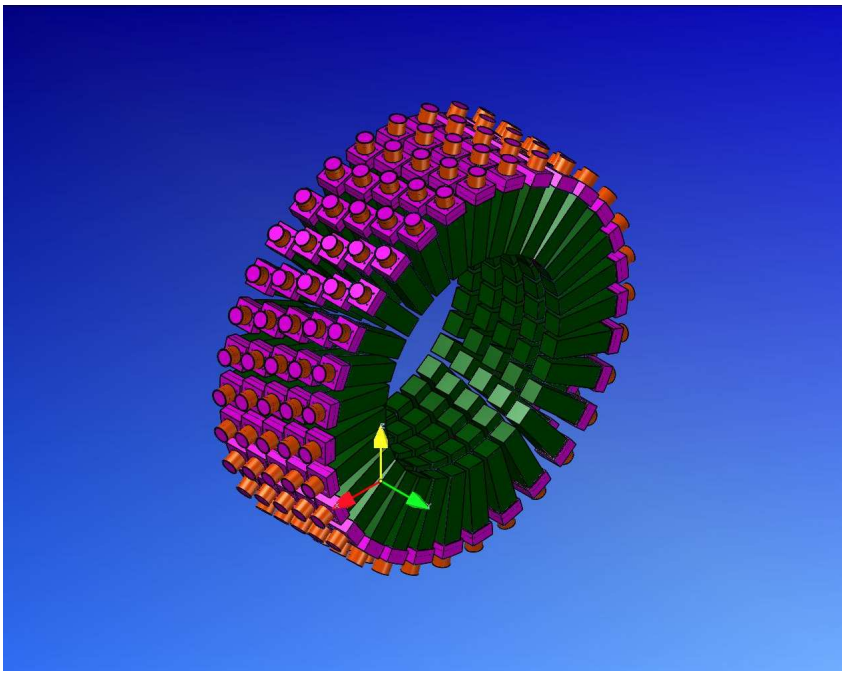

Figure 36: Layout of lead glass blocks in a pocket

with a number of holes equal to the number of blocks. Each block will be mounted in such a way as to have the PM protruding out of the hole in the air. An additional mechanical piece will be installed on the steel flange of the counter and it will have the following functions:

- Provide a stronger way of bolting the piece to the tube
- House the necessary O-ring for vacuum tightness
- Improve the strength of the module with additional gluing on the sides around the glass-steel interface

8.5 Readout

The functionality for the readout described in the proposal is still valid. Precise definition of the requirements is underway, also given the choice of the technology and the characteristics of the signals. The following points will be addressed:

- The digitizing clock frequency and accuracy
- The expected time and double pulse resolution
- The need for amplification and possibly shaping of the photomultiplier signal
- The possible integration of FADC circuitry in a new type of the TDC cards being developed in Pisa, to have redundant and complementary information
- The need for the delivery of fast trigger information

8.6 Cost estimation and responsabilities

The cost estimation for the LAV is the following:

- Lead glass blocks - in kind 2700 kCHF
- Mechanics 1500 kCHF
- High voltage 400 kCHF
- Trigger and readout 500 kCHF

The responsible institutes are Napoli, Pisa, Roma1 and Frascati. As the lead glass modules are in storage at CERN and as it is mandatory to minimize their movements, it is planned to construct the mechanical pieces in specialized firms in Europe and mount everything at CERN. It is assumed that CERN, as the host laboratory, will provide the logistics for the construction work (space, transport, workshops, etc.).

9 Liquid Krypton calorimeter (LKR)

In order to measure the inefficiency to photons of the LKR calorimeter, two analyses have been performed: the first one uses $\pi^+\pi^0$ data from a minimum bias run in 2004; the other relies on data taken in 2006 with tagged photons obtained from the bremsstrahlung of electrons in the Kevlar window and in the two first drift chambers. The latter analysis is very delicate and preliminary results giving upper limits are shown here.

9.1 2004 data

$K^+ \to \pi^+\pi^0$ decays collected during a special run in 2004 with the NA48 apparatus [27] run have been used to make this measurement. Events with a single track were selected with a trigger which included multiplicity in the drift chambers, a signal in the hodoscope compatible with one track and a muon veto. The rate was about $4 \cdot 10^4$ events/burst.
$\pi^+\pi^0$ events were selected imposing the squared missing mass (M^2_{miss}), defined as the square of the difference between the K^+ and the π^+ 4-momenta, to be equal on average to $M^2_{\pi^0}$. A cut $0.01 < m^2_{miss} < 0.026$ $(\mathrm{GeV/c^2})^2$ defined the kinematical region for signal events.
Background events were rejected with a series of requirements and cuts:

- E/p < 0.8 to reject positrons
- Cut on the decay vertex coordinates to remove tracks accidentally scattered in the beam line
- Cut on the energy in hadron calorimeter to remove muons not detected by the muon veto
- Cut on the number of hits in the charged hodoscope to reject photon conversions
- Minimum number of clusters in the LKR calorimeter to minimize effects from accidentals

- Only one cluster closer than 20 cm to the track extrapolation
- Hits in time with the seven anticounter rings and with the forward calorimeter installed and tested in that run

We assumed the minimum energy cluster not associated with the track to be the lower energy γ from the π^0. Then we looked for the other imposing the kinematics constraints.
About $7.33 \cdot 10^5 K^+ \to \pi^+\pi^0$ events were selected. For specific configurations of the energy deposition, the analysis showed a behaviour of the reconstruction algorithm which induced an inefficiency of $\approx 5{\cdot}10^{-4}$, which was recovered almost totally by an independent reconstruction software.
The behavior of the result as a function of the distance between the reconstructed cluster and the expected photon position for data and simulation is shown in Figure 37. The presence of a residual inefficiency at large distances, well explained by the simulation, can be interpreted as due to the $K^+ \to e^+\pi^0\nu_e$ background events and to $K^+ \to \pi^+\pi^0$ events in which the prediction failed because of non gaussian tails affecting the calorimeter and the spectrometer responses. In order to minimize these effects, the final inefficiency was quoted regardless of the distance of the additional reconstructed cluster from the expected photon position. Five events out of $7.33 \cdot 10^5$ were found to be inefficient, corresponding to an inefficiency of $(0.7 \pm 0.3_{stat}) \cdot 10^{-5}$, in agreement with the Montecarlo simulation.
Systematics checks on cluster energy showed that the result is stable within by $5 \cdot 10^{-6}$ as a function of the cut on the distance between the minimum energy cluster and the other clusters, indicating a second-order effect due to cluster merging. The possibility that the minimum energy cluster came from a relic of the pion clusterisation instead of a photon was investigated using a pure sample of pions collected during the 2004 run. The consequent fake inefficiency was estimated to be below $0.5 \cdot 10^{-5}$. Finally, the result was found to be stable with respect to the charged and neutral energy scales.
Taking into account both data and simulation, an upper limit was extracted from the quoted inefficiency using the procedure described in [28] applied to a binomial distribution. The uncertainty on the background and a systematical uncertainty of $0.5 \cdot 10^{-5}$ were also considered in the extraction of the upper limit, following [29]. The final result for the inefficiency η_{LKR} is:

$$\eta_{LKR} < 0.9 \cdot 10^{-5} \ @90\%\ C.L.\ (E_\gamma > 10GeV) \tag{5}$$

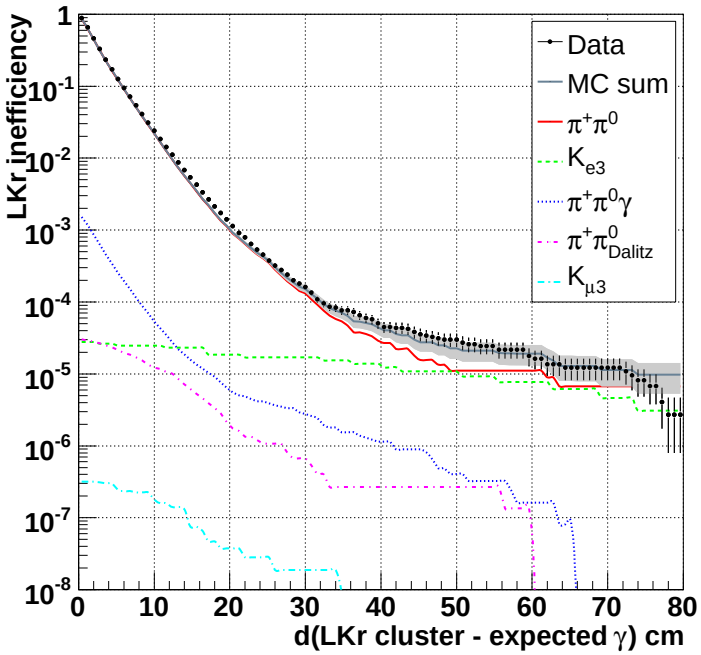

Figure 37: Inefficiency as a function of the distance between the cluster reconstructed in the calorimeter and the expected photon position in $K^+ \to \pi^+\pi^0$ events. A gray band corresponds to the total statical uncertainty of the simulation.

9.2 2006 data

An alternative method to measure the efficiency of the calorimeter was exploited in a dedicated run performed in 2006. This run made use of the NA48 apparatus and of an electron beam produced by protons extracted from the SPS. The electrons were selected to have 25 GeV/c momentum with a RMS spread of 0.2%. Just before the beginning of the decay region, two dipoles controlled the beam direction in x and y giving the freedom to choose the impact point on the downstream detectors. The electrons could interact with the experimental apparatus and produce bremsstrahlung photons. When the radiation occurred in the 1.3% X_0 material upstream of the spectrometer magnet, the beam direction defined the impact point of the photons on the calorimeter. At the same time the spectrometer magnet deflected in the x direction the electrons which hit the calorimeter at the same y position of the photons, but at least 12 cm distant along x. During the data-taking the hit multiplicity in the hodoscope was used to trigger the electrons, producing about 1 KHz of data acquisition rate. A matrix of 40×24 cells around the impact point of the photon on

the calorimeter was not zero suppressed in order to study the effect of a possible on-line inefficiency for low energy photons. Figure 38 shows the positions of the clusters in a typical event.

The measurement is limited below 4 GeV by a background due to electron bremsstrahlung in $\approx 1\%$ X_0 of air in the beamline downstream of the 25 GeV/c momentum selection. To reduce this background, we used the x-deflecting magnet at the entrance of the decay region as an electron spectrometer. A cut in dx/dz of the electron was applied as a function of the expected photon energy: this cut is effective in controlling the background above 4 GeV. Below 4 GeV the background is at the level of 10^{-3} and only an upper limit for the inefficiency can be quoted.

The accepted events were divided in 5 bins of energy with the statistics shown in Table 14.

Table 14: Statistics of the accepted events.

E_γ (GeV)	Number of events
2.5,4	$1.2 \cdot 10^5$
4,5.5	$3.5 \cdot 10^5$
5.5,7.5	$4.7 \cdot 10^5$
7.5,10	$3.1 \cdot 10^5$
>10	$5.6 \cdot 10^5$

To handle properly the low energy photons which could merge with a nearby 25 GeV electron, an optimized reconstruction algorithm was implemented to identify two adjacent clusters, with a correction for fake clusters (due to the non zero-suppression readout), obtained from a sample of full-energy electrons.

The preliminary results from the analysis are shown in Table 15.

The result above 10 GeV is consistent with the measurement done in 2004. The study of the systematics, needed to improve the upper limits below 10 GeV, is not straightforward, as it needs an accurate simulation of the beam line, of the radiation effects in the decay volume and of the cluster merging effects.

9.3 LKR Consolidation

The LKR must be kept operational during the R&D and construction phase of the experiment and consolidation phase was launched for both the cryogenic control system and the readout

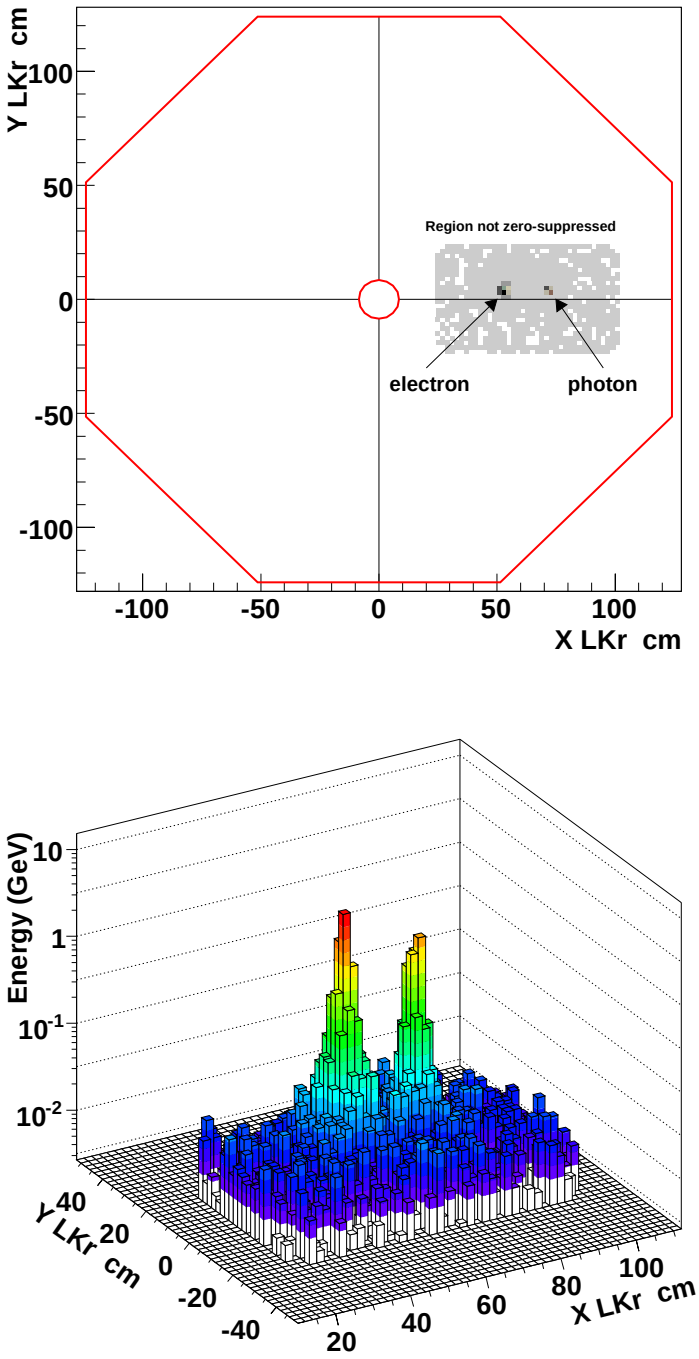

Figure 38: Clusters on the electromagnetic calorimeter for an event in which the electron did bremsstrahlung (a). Energy profile of the clusters: each bin corresponds to one cell.

electronics. A New control system will be installed during the 2007-2008 shutdown [30].

Table 15: Preliminary values of the single-photon calorimeter inefficiency as a function of the photon energy.

E_γ (GeV)	Inefficiency
2.5,5.5	$< 10^{-3}$
5.5,7.5	$< 10^{-4}$
7.5,10	$< 5 \cdot 10^{-5}$
>10	$< 8 \cdot 10^{-6}$

Concerning the readout, the old optical link cards sending the data from the digitiser (CPD) to the Data Concentrator suffered hardware failures due to the critical environment in which they were operating (temperature $\sim 35^\circ$ C). They are being replaced by CMOS to LVDS translators and the CPD output is directly connected to a new board, FPGA based, via standard 30 cm twisted pair shielded CAT5 cables.
The new Smart Link Module board (SLM), shown in Figure 39), hosts an Altera Cyclone II FPGA driving the input data coming from 4 CPDs with a rate of 60 MB/s. A finite state machine stores the raw data from the CPDs into the SRAM. Thereafter reformatting is performed and the data is stored at fixed addresses in a 1 GB DDR2 memory also hosted in the SLM. The data are then sent via a standard 1Gb Ethernet connection from the SLM directly to a rack PC. Each PC receives data from 4 SLMs, having 224 CPDs the new system will consist of 56 SLMs and 14 PCs. The data will be zero suppressed and/or compressed in the PCs and afterwords they will be merged with the data coming from the other subdetectors.
The new read-out chain will also avoid the use of the Data Concentrator and RIOs electronics where, after 12 years of operations, we also start to suffer lack of spare modules.
The new system was debugged during 2007 run reserving 16 CPDs for this purpose. The read-out chain was successfully tested and the project is now ready for the final construction.

10 Small angle vetoes (IRC and SAC)

The new layout is compatible with only one Intermediate Ring Calorimeter (IRC) at the entrance of the LKR calorimeter and with the Small Angle Calorimeter (SAC) covering the zone near 0 degrees after the muon deflecting magnet. Even if the positions and alignments

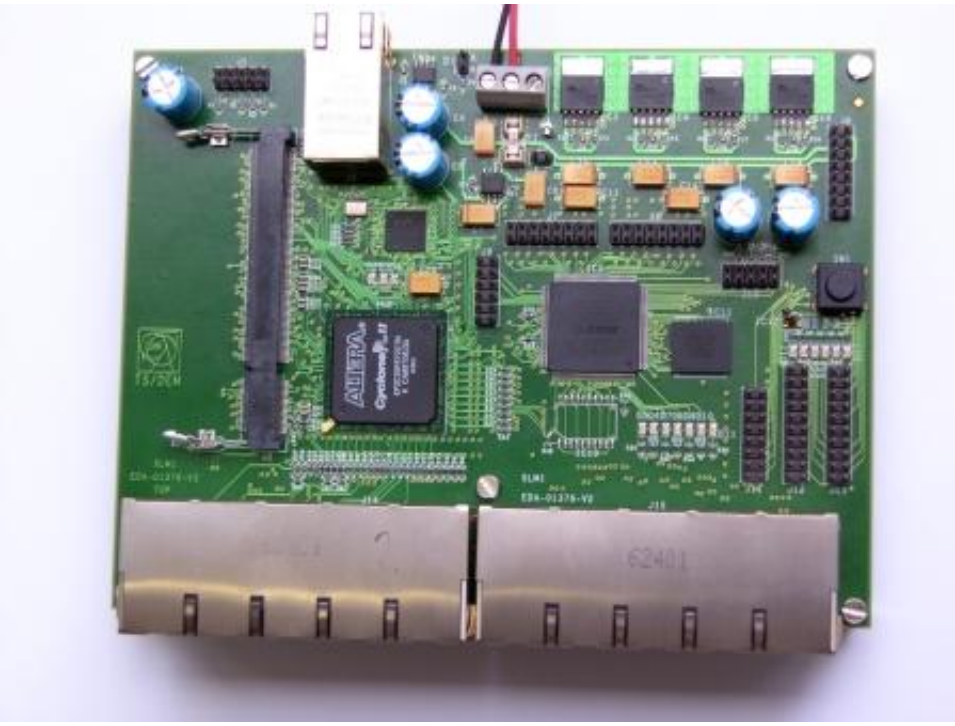

Figure 39: The SLM (Smart Link Module) board.

are slightly different from the ones in the proposal, the basic requirements are still the same. As baseline design, it is planned to build both detectors with the "shashlyk" technology as described in the proposal. Indeed, during 2006, a small prototype for the SAC has been built with the "shashlyk" technology and this was tested during the 2006 run.

10.1 SAC prototype testing in 2006

Durung the P326 2006 test run a prototype of the shashlyk SAC was constructed and tested. It profitted from the electron beam of 25GeV and preliminary studies were undertaken.
The active part of the detector was assembled from 70 lead plates with thickness of 1.5mm with 1.5mm scintilator plates in between for a total of 16 radiation lengths. The transversal dimensions were chosen to be 20.5x20.5 cm. The light was taken out with 480 wave-length shifting fibers 1mm Y-11(250)MSJ (Kuraray) which were separated into four bunches. The detector was equipped with four photomultipliers. The complete prototype was placed inside a black-painted metal box. A picture of the detector is shown on Figure 40.
During the tests the detector was placed between the two planes of the scintilator hodoscope of the NA48 experiment. The signals were sent to the existing CPD based read-out of the

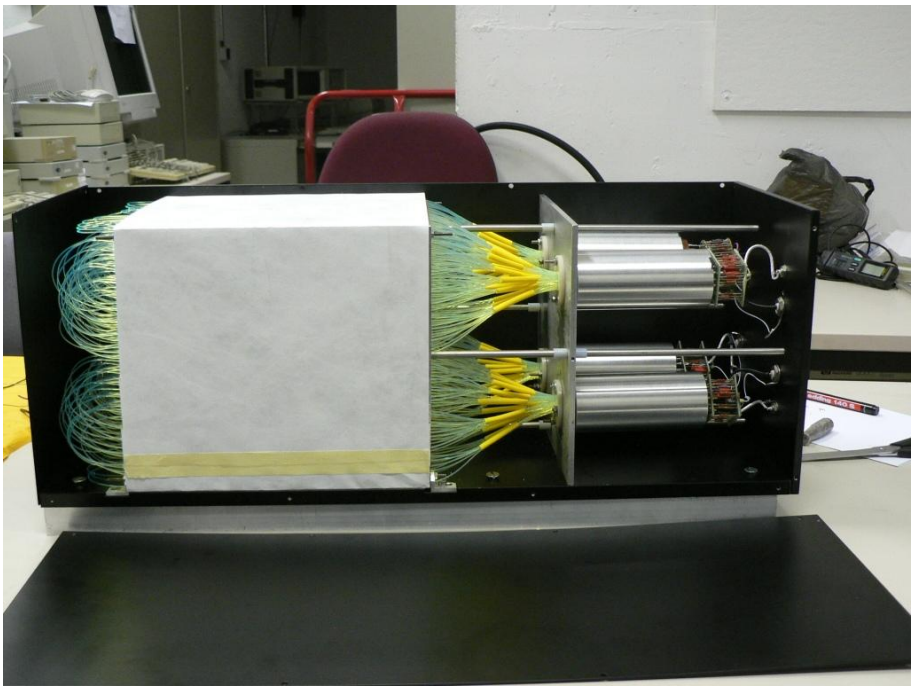

Figure 40: SAC prototype at the assembly room before closing the front side of the box. The body of the detector is wrapped with white paper and the scintilating fibers taking the light to the photomultipliers are visible.

muon veto.

The electron beam was deflected to point directly to the SAC. Several runs were taken with the beam pointing to different spots of the detector which allows to study the inefficiency as a function of the entry point. A total of 10^7 events were recorded.

The trigger for the data taking was based on signal from the spectrometer consistent with one charged track. The digitized data from the read-out first had to be decoded (i.e. to reconstruct the individual hits) and afterwards to reconstruct the clusters and measure their energy. A small sample of data was analyzed with a very simplified reconstruction based only on peak-finding. The energy was reconstructed as weghted sum of the amplitude A_i in the four channes.

$$E_{tot} = \alpha_1 * A_1 + \alpha_2 * A_2 + \alpha_3 * A_3 + \alpha_4 * A_4 \tag{6}$$

which were determined requiring a mean energy of 25 GeV in a subsample of the data.

The offline selection required only one charged track with momentum between 24.8 and 25.2 GeV and a hodoscope time inside the trigger window. The track also had to point inside

the prototype. A total of 35846 events were reconstructed. The ΣA_i distribution is shown on Figure 41. No event was found without an associated signal in the SAC-prototype. This allows to set an upper limit of the inefficiency $\epsilon < 6.4 \times 10^{-5}$ with 90% confidence level.

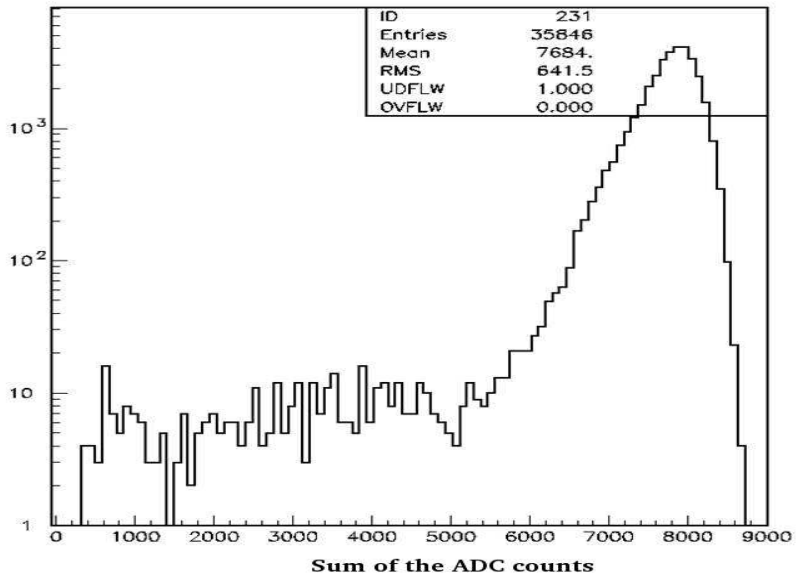

Figure 41: Reconstructed energy of the events used to measure the shashlyk prototype inefficiency. With a cut at 200 ADC counts the number of the inefficient events is 0.

The data analysis and the study of the inefficiency and the random veto as a function of the reconstructed energy treshold is still ongoing. The cost of the SAC-prototype was minimized due to the usage of the existing read-out of the muon veto and power supply system of the NA48 hadron calorimeter. The total cost was approximately 20 KCHF not including the man power.

10.2 Total cost estimation for the Small Angle Vetoes

The cost of the prototype was extrapolated to obtain the total expected cost of the SAC and IRC taking into account more complicated design of the mechanics of the IRC.

- Scintillator 30 kCHF
- Lead and Mechanics 30 kCHF

- Fibers 3 kCHF
- Photomultipliers 12 kCHF
- HV and ReadOut 25 kCHF

The teams responsible for the construction are University of Sofia and INR Moscow.

11 Charged anticounters CHANTI

We have introduced a set of ring anticounters after the last Gigatracker station to form a "guard ring" and a large one around the beginning of the decay volume to veto charged particles coming from the collimator. There will be six rings of inner diameter 100mm and outer diameter 300 mm. The large counter will have an inner diameter of 360 mm and an outer one of 1200 mm.
They will be built with scintillator tiles with a suitable segmentation in ϕ, read with wavelength shifting fibers. There will be two planes of 1cm-thick scintillator for each ring with a small staggering to avoid cracks. Fibers from corresponding longitudinal layers will be connected to the same photomultiplier.
The responsible teams are Napoli, Pisa, Roma1 and Frascati. The expected costs are

- Scintillator and fibers 15 kCHF
- Mechanics 30 kCHF
- HV and Readout 30 kCHF
- Photomultipliers 40 kCHF

12 The RICH

The RICH detector must fulfill the following tasks:

- separate $\pi^{\pm}$ from $\mu^{\pm}$ between 15 and 35 GeV/c momentum providing a muon suppression factor of at least 10^{-2};
- measure the pion crossing time with a resolution of the order of 100 ps;
- produce the L0 trigger for a charged track;
- help in the rejection of momentum non-gaussian tails of the magnetic spectrometer;
- help in the rejection of photons close to the beam pipe.

Neon at atmospheric pressure has been chosen as the Cherenkov radiating medium. The available space between the last straw chamber and the Liquid Krypton calorimeter is about 18 m which guarantees a good number of photoelectrons and a good Cherenkov angle resolution, if a fine photon detectors granularity is provided: this drives the choice of single anode photomultipliers which can be packed at an interdistance not larger than 18 mm.

12.1 The Cherenkov effect

When a particle of velocity β (in units of speed of light c) crosses a medium with index of refraction n, it emits radiation at an angle θ_c with respect to the particle trajectory such that:

$$\cos\theta_c = \frac{1}{n\beta}; \quad \text{or} \quad \sin\theta_c = \frac{\sqrt{n^2\beta^2 - 1}}{n\beta} \tag{7}$$

forming a Cherenkov cone of half-angle θ_c. The threshold velocity β_t, below which no radiation is emitted, is given by ($\theta_c = 0$) $\beta_t = 1/n$, while the maximum angle of emission θ_{max} is reached for $\beta = 1$ and so:

$$\cos\theta_{max} = \frac{1}{n}; \quad \text{or} \quad \sin\theta_{max} = \frac{\sqrt{n^2 - 1}}{n} \tag{8}$$

If the particle has mass m, the relation between the momentum p and the Cherenkov angle is given by:

$$p = \frac{m}{n\sqrt{\sin^2\theta_{max} - \sin^2\theta_c}}; \quad \sin\theta_c = \sqrt{\sin^2\theta_{max} - \frac{m^2}{n^2p^2}} \tag{9}$$

The threshold momentum p_t for Cherenkov radiation is:

$$p_t = \frac{m}{\sqrt{n^2 - 1}} \tag{10}$$

In order to have full efficiency for a 15 GeV/c momentum pion, the threshold should be around 20% smaller or 12.5 GeV/c, corresponding to $(n-1) = 62 \times 10^{-6}$: this corresponds almost exactly to Neon at atmospheric pressure.
The number of photons N emitted through a radiator thickness x per unit of photon energy E is predicted by the Frank-Tamm equation as a function of the Cherenkov angle (assuming a singly charged particle):

$$\frac{d^2N}{dEdx} = \frac{2\pi\alpha}{hc}\sin^2\theta_c \simeq 370\sin^2\theta_c\,\mathrm{eV}^{-1}\mathrm{cm}^{-1} \tag{11}$$

12.2 The RICH concept

In a RICH (Ring Imaging CHerenkov), the Cherenkov cone is imaged, by means of a spherical mirror, on a photon detector put on the focal plane of the mirror. The focal plane is defined as a plane crossing the focal sphere (the sphere concentric with the spherical mirror and with half the radius) in a point crossed by an axis connecting the mirror curvature centre and a particular point of the mirror (for example the intersection with the beam pipe axis). The orientation of the focal plane is chosen so that the particle average direction is orthogonal to it. If the particle trajectory is orthogonal to the focal plane, the Cherenkov cone image on this plane is a ring of radius r_{ring} given by:

$$r_{ring} = f\tan\theta_c \simeq f\theta_c \tag{12}$$

where f is the focal length of the spherical mirror (i.e. half of its curvature radius) and the approximation is good assuming small Cherenkov angles (it is the case in gas radiators). In Figure 42 the Cherenkov angle as a function of the momentum for pions, muons and electrons is shown.
All the particles with parallel trajectories form concentric rings. If the particle trajectory forms an angle α with the axis orthogonal to the detector plane, the centre of the ring is shifted by a distance d given by

$$d = f\tan\alpha \tag{13}$$

in the same direction of the particle trajectory inclination and the ring is slightly distorted to an ellipse of minimum and maximum semiaxis:

$$a_{min} = f\tan\theta_c;\quad a_{max} = f\tan\theta_c/\cos\alpha \tag{14}$$

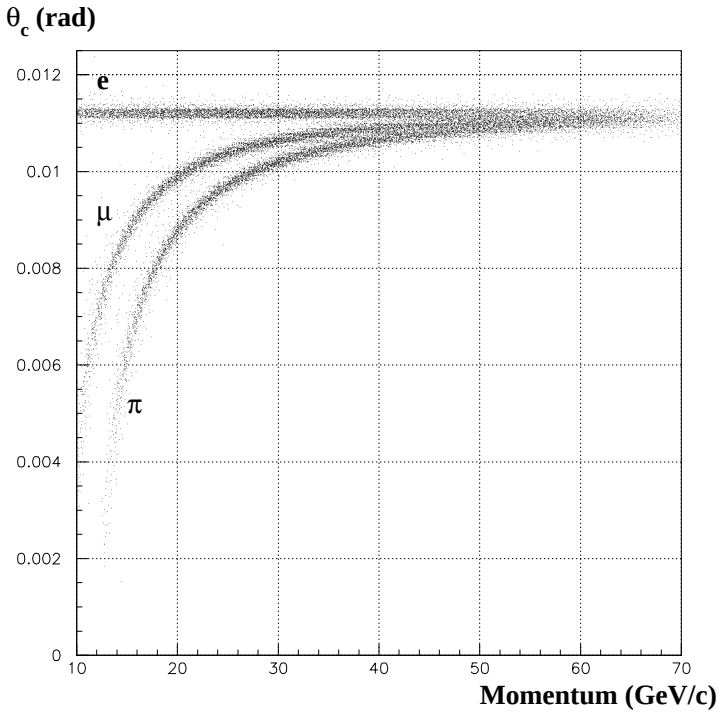

Figure 42: Cherenkov angle as a function of momentum for pions, muons and electrons for the RICH described in the text.

12.3 The NA62 RICH

In the NA62 experiment it is planned to put a RICH between the forth Straw Chamber and the Liquid Krypton Calorimeter. The RICH is composed by a cylindrical vessel 18 m long and 2.8 m large with the beam pipe passing through it. The pipe has three section, of about the same length, with diameter of 20, 22 and 24 mm respectively, increasing in the beam direction; the pipe form an angle of about 2.5 mrad with respect to the vessel axis to follow the beam trajectory. The vessel is filled with Neon at atmospheric pressure which corresponds to 5.6% radiation length. At the downstream end of the vessel a mosaic of mirrors is placed; in order to avoid the beam pipe shadow, Cherenkov photons are reflected by two groups of mirrors pointing to two different regions. The focal length of the mirrors is 17 m (it could be increased as close as possible to the Vessel length). Each focal region is equipped with about 1000 PMTs Hamamatsu R7400-U03 with a pixel size of 18 mm in a compact hexagonal packing. The active area of each PMT is about 8 mm large and a Winston cone is used to convey the Cherenkov light from the 18 mm pixel size. The centre of each PMTs region is about 1 m far from the beam pipe axis.

12.4 The number of photoelectrons

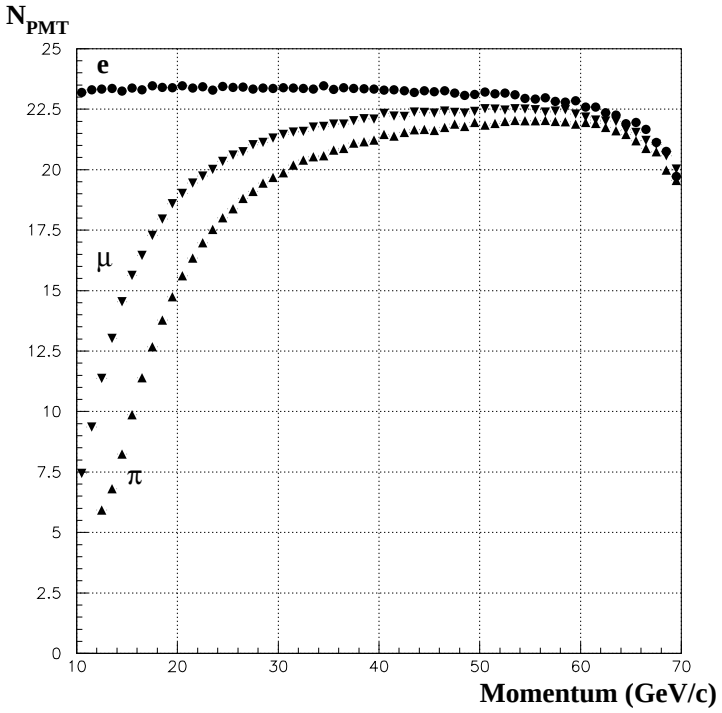

Figure 43: Average number of hit PMTs per event as a function of momentum for pions, muons and electrons from Kaon decays. The drop at high momentum is due to the beam pipe acceptance (high momentum particles tends to be closer to the beam pipe).

The number of Cherenkov photons emitted from the particle passing through the radiator is given by the Frank-Tamm equation. The number of detected photons (photoelectrons) depends on the mirror reflectivity ϵ_{mirr}, the photon detector geometrical acceptance ϵ_{geom}, the photon collection efficiency ϵ_{coll},the transparency ϵ_{trasp} of the medium or of any window separating the detector from the medium and above all on the quantum efficiency $\epsilon_q(E)$ of the photon detector which will depend on the photon energy. Integrating the Frank-Tamm equation over the radiator length L and over the photon energy E, the number of photoelectrons $N_{p.e.}$ is given by:

$$N_{p.e.} = \frac{2\pi\alpha}{hc} L \int \epsilon_{mirr}\epsilon_{geom}\epsilon_{coll}\epsilon_{trasp}\epsilon_q(E)\sin^2\theta_c dE \tag{15}$$

which can be written as:

$$N_{p.e.} \simeq N_0 L \sin^2\theta_c \tag{16}$$

where the quality parameter N_0 is defined as:

$$N_0 = 370 \text{ eV}^{-1}\text{cm}^{-1}\epsilon_{mirr}\epsilon_{geom}\epsilon_{coll}\epsilon_{trasp}\int \epsilon_q(E)dE \tag{17}$$

In Figure 43 the number of photoelectrons as a function of the momentum for pions, muons and electrons from Kaon decays is shown.

We use $\epsilon_{trasp} \approx 0.90\%$ assuming that the PMT are separated from the Neon by a quartz window. We use $\epsilon_{mirr} \approx 0.85$ from the SELEX experiment result for $\lambda > 160$ nm with a mirror coated with aluminum and MgF_2.

ϵ_{geom} is given by the PMTs packing efficiency: $\epsilon_{packing} \approx 0.90$ (see Section 12.5). The catching efficiency of the Winston cone funnelling the light to the PMT is 0.8 from HERMES experiment results (fraction of photons impinging on the funnel reflected to the photocatode); assuming the funnel covers an area of diameter 18 mm, while the PMT has an active diameter of 8 mm, the photon collection ϵ_{coll} contribution is 0.85.

Finally $\int \epsilon_q(E)dE \approx 0.60$ eV for a PMT Hamamatsu R7400-U03 with a UV-glass window and 0.75 eV for a PMT Hamamatsu R7400-U06 with a quartz window: the former PMT type is assumed in the following.

N_0 comes out to be about 130 cm^{-1}, which corresponds to 27.8 photoelectrons for $\theta_c = \theta_{max} = 11.207$ mrad. The number of hit PMTs is smaller than this because the probability that more than one photoelectron is produced in the same PMT is not negligible.

12.5 The Number of Photomultipliers needed

The most efficient way to pack photomultipliers with circular head is with a compact hexagonal packing, where the PMTs are placed at the vertices and in the centre of regular hexagons assembled as in a honeycomb. In Figure 44 the principle of the compact hexagonal packing is shown.

If the distance among the close PMTs centres is d, the area of the regular hexagon is $3\sqrt{3}d^2/2$ while the area of the circles is $\pi d^2/4$. Each hexagon contains $(1 + 6 \times (1/3))$ circles, so that the packing efficiency $\epsilon_{packing}$ is 90.7%.

The result of the simulation gives for $d = 18$ mm and a mirror focal length $f = 17$ m a number of about 2000 PMTs which are hit from photons produced by pions coming from the signal, in the acceptance of the NA62 apparatus and with a momentum between 15 and 35 GeV/c.

In Figure 45 and 46 the PMTs hit by reflected Cherenkov photons are shown; in Figure 47 some examples of Cherenkov rings are shown.

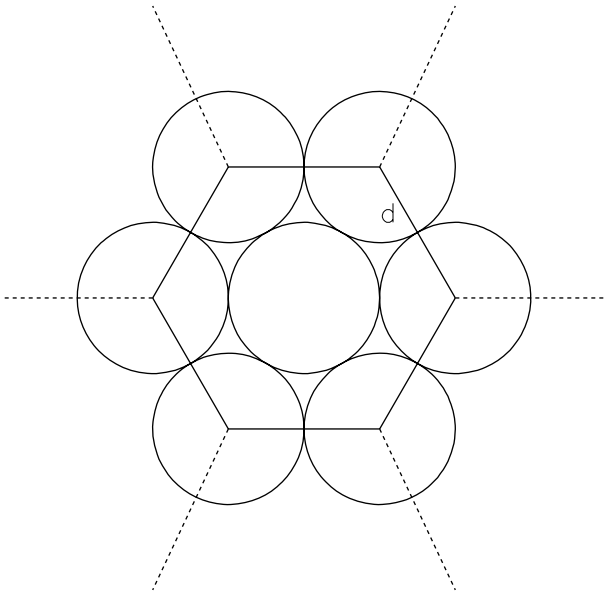

Figure 44: The compact hexagonal packing; d is the distance among close circles centres.

12.6 The mirrors

The area to be covered by a mirror is a very large one, about 2.8 m in diameter, so that is mandatory to foresee a mosaic of smaller pieces. Assuming to build 1 m diameter mirrors, the most compact solution is to produce them in hexagonal shape. Ten mirrors are necessary, of which four of hexagonal shape (but two of them with a semi-hole to accomodate the beam pipe) and six of semi-hexagonal form. An alternative possibility under study concerns four octagonal mirrors, 1 m in diameter, around the beam pipe and four square mirrors, with a smaller diameter, to fill the uncovered area far from the pipe. Each mirror has a glass bulk 2.5 cm thick, a focal 17.0 m long and a D_0 smaller than 1 mm. The D_0 is defined as the radius of the smallest circle, transverse to the mirror axis, where 95% of the light coming from a point source is imaged. Each mirror is independently supported and aligned. Half of the mirrors point to the upper PMT region, half to the lower one, in order to avoid the beam pipe shadow.

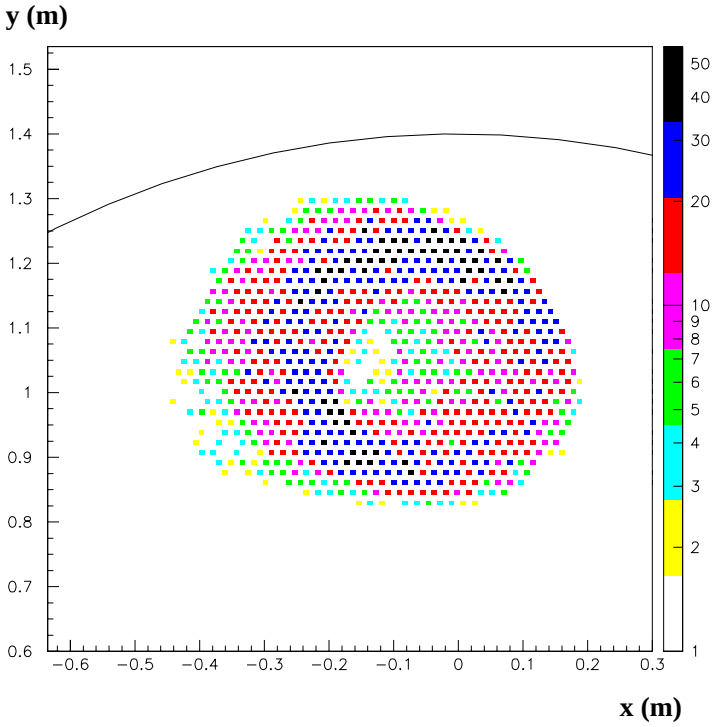

Figure 45: PMTs hit by the photons reflected by one group of mirrors (those pointing upwards).

12.7 Single hit resolution

The ring radius resolution depends on the number of hits and on the single hit resolution. The result of the simulation for the NA62 setup for the Cherenkov angle resolution is shown in Figure 48. The Cherenkov ring is fitted with a circle with 3 degrees of freedom (position of the centre and radius). Actually an ellipse with the same degrees of freedom is fitted (the eccentricity and orientation are constrained by the centre position). The fit is accepted if at least 5 hits are used and if the χ^2 per d.o.f. is smaller than 2.

12.7.1 Pixel size

The proposed pixel size s is 18 mm, so that the contribution to the single hit angle resolutions is, with a focal length $f = 17$ m:

$$\Delta\theta_{pixel}(\,\mathrm{single\,hit}) = \frac{\mathrm{s}}{4\,\mathrm{f}} = 265 \;\; \mu\mathrm{rad} \tag{18}$$

where $s/4$ is the variance of the distance of a uniform distribution inside a circle from an external point. The pixel size contribution to the angle resolution becomes 65 μrad and is

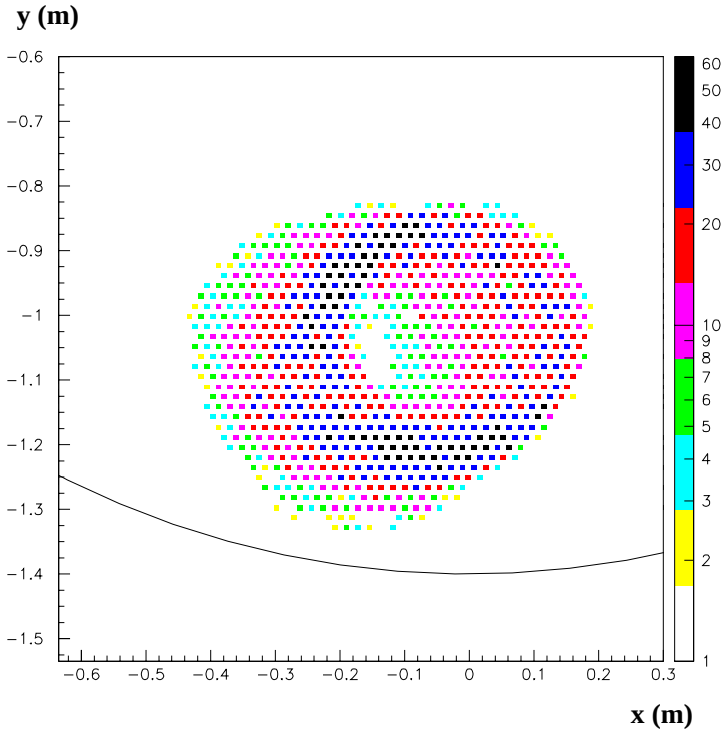

Figure 46: PMTs hit by the photons reflected by one group of mirrors (those pointing downwards).

the major contribution.

12.7.2 Neon dispersion

The variation of the Neon index of refraction as a function of photon frequency ν at 760 mmHg and 0 degree Celsius, according to Landolt, is given by:

$$n - 1 = \frac{C}{\nu_0^2 - \nu^2} \tag{19}$$

with $C = 2.61303 \times 10^{27}$ Hz^2 and $\nu_0^2 = 39160 \times 10^{27}$ Hz^2. The effect of Neon dispersion on the Cherenkov angle resolution depends on the spectral response of the chosen PMTs. Assuming the Hamamatsu R7400U-03 it turns out that the average dispersion $\Delta n = 1.3 \times 10^{-6}$ (it would be 2.2×10^{-6} for a Hamamatsu R7400U-06) and we have for a pion of 35 GeV/c momentum:

$$\Delta\theta_{dispersion}(\,\text{single hit}) = \frac{\Delta \text{n}}{\theta_\text{c}} = 125 \;\; \mu\text{rad} < \frac{1}{2}\Delta\theta_{\text{pixel}} \tag{20}$$

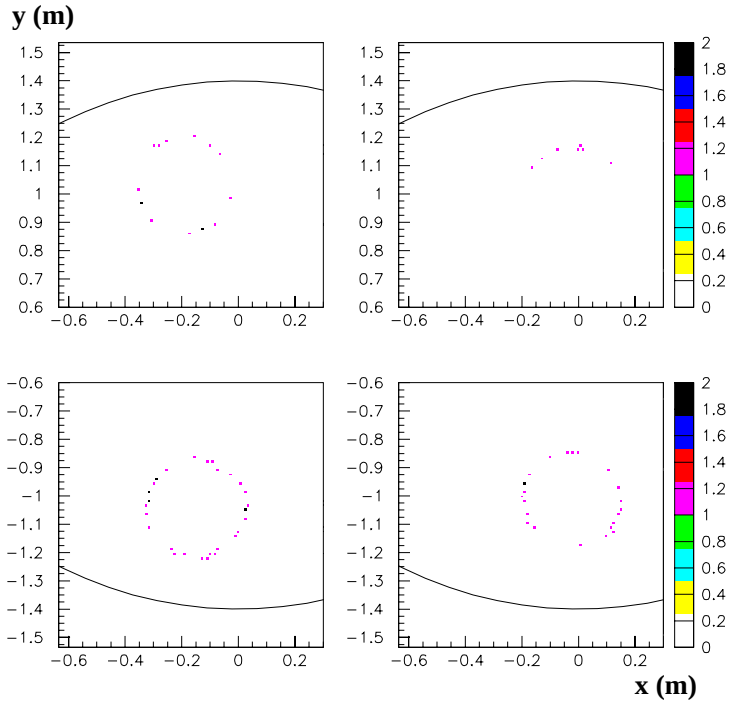

Figure 47: Example of Cherenkov rings. Top-left: ring fully contained in the upper PMTs region; bottom-left: ring fully contained in the lower PMTs region; top-right and bottom-rigth: ring contained in both the PMTs region. The rings are produced by a 35 GeV/c momentum pion.

12.7.3 Pion Multiple Scattering

The pion multiple scattering is given by:

$$\theta_{ms} = \frac{13.6\ \text{MeV}}{p}\sqrt{\frac{x}{X_0}}\left(1 + 0.038\log\left(\frac{x}{X_0}\right)\right) \approx 80\ \mu\text{rad}\frac{35\ \text{GeV}}{p} \tag{21}$$

where the number of radiation length crossed by the pion in the Neon (x/X_0) is about 5.6% and p is the pion momentum; due to the fact that the Cherenkov radiation is uniformly produced along the pion path in the Neon and not at the end, the contribution to the single hit resolution is given by:

$$\Delta\theta_{ms}(\,\text{single hit}) = (2/3)\theta_{\text{ms}} \approx 55\ \mu\text{rad}\frac{35\ \text{GeV}}{\text{p}} << \Delta\theta_{\text{pixel}} \tag{22}$$

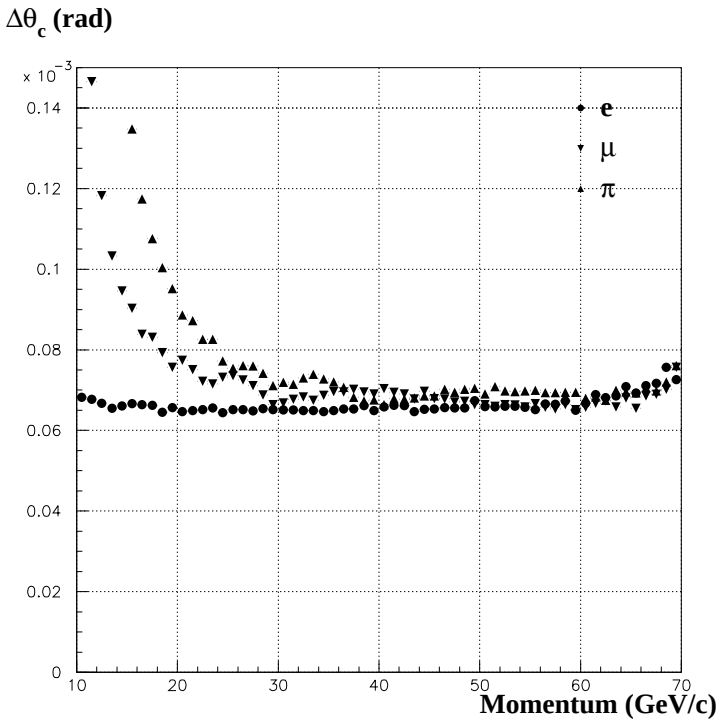

Figure 48: Cherenkov angle resolution.

12.7.4 Other contributions

Other contributions to the Cherenkov angle resolution are small compared to the previous discussed effects. The dependence on the point of photon emission on the pion track increase at high momentum but is still very small. The quality of the mirror assumes a $D_0 = 4$ mm which corresponds to

$$\Delta\theta_{mirror}(\,\text{single hit}) = \frac{\mathrm{D_0}}{16\,\mathrm{f}} = 15\ \mu\text{rad} \tag{23}$$

12.8 Momentum Resolution

The momentum resolution, if the particle mass is known, is given by:

$$\frac{\Delta p}{p} \approx \frac{p^2}{m^2}\,\theta_c\ \Delta\theta_c \tag{24}$$

where $\Delta\theta_c$ also depends on the pion momentum. In Figure 49 the momentum resolution for a pion is shown.

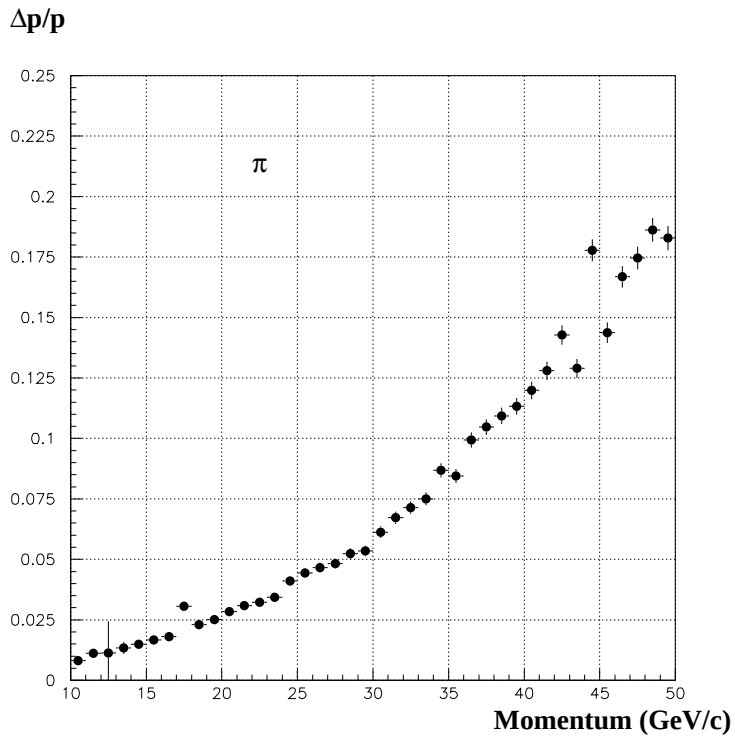

Figure 49: Momentum resolution, imposing the pion mass, as a function of the true momentum.

12.9 Pion-Muon separation

If the momentum p is measured by some other detector (i.e. the spectrometer) the particle mass m_{rec} can be reconstructed from the Cherenkov angle θ_c

$$m_{rec}^2 = p^2 \left(\theta_{max}^2 - \theta_c^2\right) \tag{25}$$

In Figure 50 the squared reconstructed mass at three different momenta are shown: the electron, muon and pion peaks are clearly visible. Momentum resolution and non gaussian tails from the spectrometer are not included.

Putting a cut half-way between the electron and muon peaks (electron selection) and between the muon and pion peaks (pion selection), the suppression factor for muons and the electron or pion losses can be determined and are shown in Figure 51. The muon suppression factor in pion selection, integrated between 15 and 35 GeV/c momentum, is 1.3×10^{-3} (momentum resolution and tails from the spectrometer not included). The muon suppression factor can be improved at the prize of a higher signal loss.

In Figure 52 the muon rejection performances are shown in the case in which only one

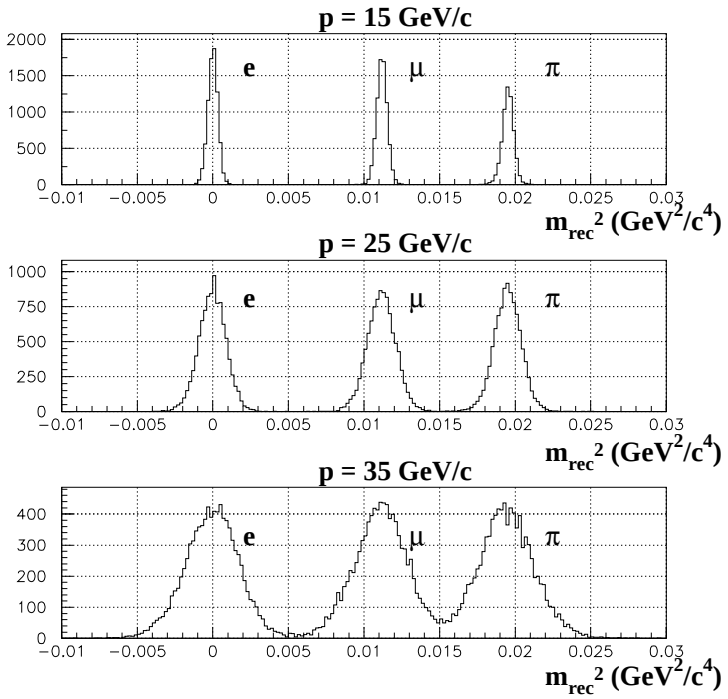

Figure 50: Reconstructed squared mass for three different momenta. The peaks of electrons, muons and pions are clearly visible.

effective mirror (no split) is used and the beam pipe shadow is not removed compared with the standard case (two effective mirrors or split case). The muon suppression factor in pion selection, integrated between 15 and 35 GeV/c momentum, becomes 2.0×10^{-2} in the no split case

12.10 The RICH prototype

A RICH prototype has been built and tested in October 2007. A stainless steel vessel, 17 m long and 60 cm wide (divided in 5 sections) and vacuum resistant, has been placed in the NA62 cavern, where the KABES detectors were previously located. A 50 cm wide, 2.5 cm thick mirror, with a focal length of 17 m, built by the Marcon company, has been used; this mirror is of high optical quality with a D_0 of 0.4 mm. The vessel has been evacuated, then filled with nitrogen for cleaning, again evacuated and finally filled with Neon at 980 mbar. The mirror has been placed at the downstream end of the vessel, mounted on a support structure which could be oriented in two axis by means of two remotely controlled

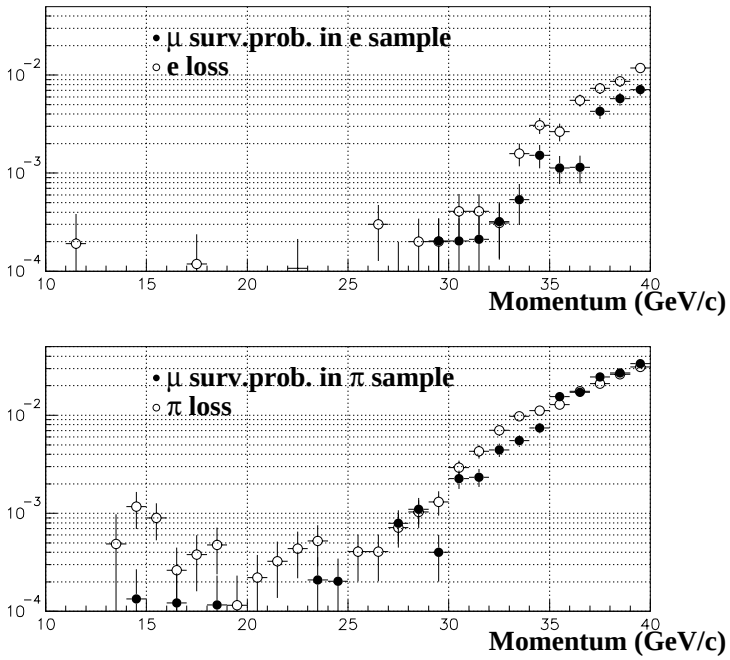

Figure 51: Top plot: electron loss and muon suppression in electron selection. Bottom plot: pion loss and muon suppression in pion selection.

step motors and closed with a stainless steel flange 30 mm thick. At the upstream end a stainless steel flange, again 30 mm thick, has been placed and properly drilled to accomodate 96 PMTs of Hamamatsu R7400 U03 and U06 type (see Figure 53). The PMTs has been separated from the Neon by 1 mm thick quartz windows; a Winston cone, covered with a thin mylar foil, is used to convey the light to each PMT, as it is foreseen for the final detector. The PMTs has been placed where the Cherenkov ring of a 200 GeV/c pion beam was expected, at an interdistance of 18 mm.

In a test performed in the 2006 fall, using a CEDAR detector, Hamamatsu PMTs R7400 of type U03, U04 and U06 were tested and U04 type turned out to be too inefficient for our purposes: the 2007 test beam output will drive the final choice between U03 and U06.

The RICH prototype has been exposed to a 200 GeV/c momentum negative beam, composed mainly of pions, between the end of October 2007 and the first two weeks of November 2007. The data analysis is in progress, but it has already confirmed the expectations: an event time resolution better than 100 ps, a Cherenkov ring resolution better than 60 μrad and a number of fired PMTs per event close to twenty.

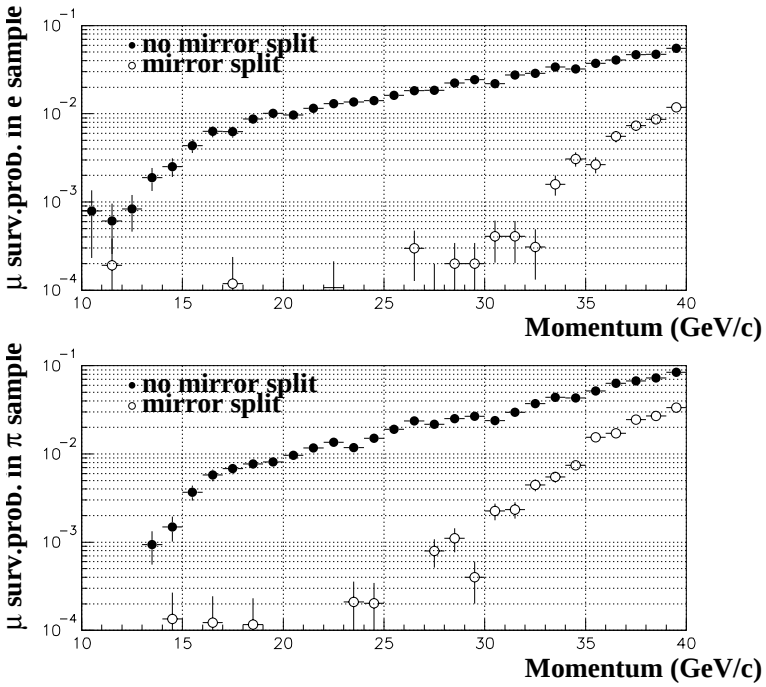

Figure 52: Comparison of the muon rejection performances with only one mirror (no split case) and two mirrors (split case).

In 2008 a further test beam with the same prototype is foreseen, adapting the upstream flange to accomodate about 400 PMTs; a beam of various momenta will be used to check the separation of various particles species as a function of momentum.

12.11 Cost Estimation

The cost of the materials for the construction of the RICH counter has been evaluated and is presented in Table 16.

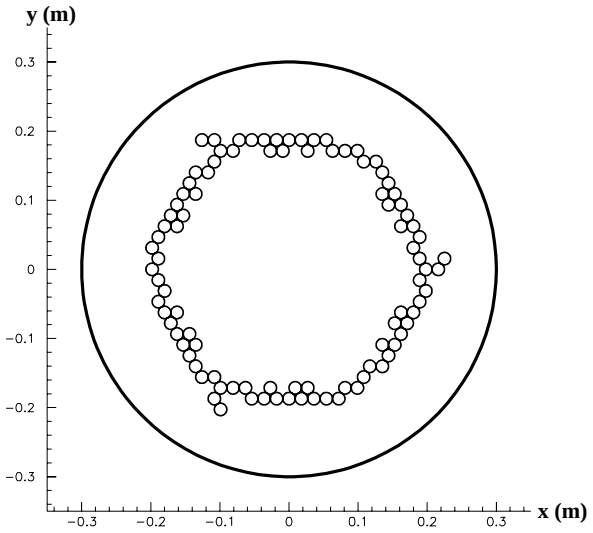

Figure 53: Upstream flange of the RICH prototype: the positions of the 96 PMTs are shown.

Item	Quantity	Unit prize (Euro)	sub total cost (Euro)
Vessel	1	-	200 k
Gas system	1	-	50 k
Vessel thermal isolation	1	-	50 k
T and P probes system	1	-	30 k
PM R7400U03 and base	2000	350	700 k
Mirrors (different shapes)	12	$\approx$ 20000	250 k
quartz windows	2000	7.5	15 k
PM mechanics	1	-	20 k
Mirrors mechanics	1	-	25 k
HV (two PM per channel)	1000	300	300 k
FE electronics	2000	40	80 k
TDC (Tell1 based)	2000	50	100 k
racks, LV, cables	-	-	60 k
TOTAL			1880 k

Table 16: Estimated cost of the RICH counter. At the indicative exchange rate of 1.6 CHF/Euro, the total cost amounts to 3008 kCHF.

13 Straw Tracker (STRAW)

To minimize the multiple scattering of the outgoing pion it is proposed to operate the magnetic spectrometer in vacuum upstream the decay region. This means that the decay and spectrometer regions are not separated and share a common vacuum volume. A straw tracker has been chosen as the most promising detectors to be operated in vacuum. In addition, the straw tracker could be designed without internal frames and flanges. The latter is rather important to diminish the background arising from the beam halo particle interactions. The proposed design of the straw detector is partially based on the experience accumulated during the production and exploitation of a similar straw trackers built for the COMPASS and ATLAS experiments. The main changes compared to SPSC-2005-013 11.6.2005 are:

- Single dipole with four chambers instead of six.
- Independent straw tubes: four layers in one view instead of two.
- New straw manufacturing process: ultrasonic welding.
- Improved straw connectivity scheme based on flex-rigid Kapton circuits.
- Results from the test beam in October 2007.

The straw tracker contains four chambers and each chamber has four views (x,y,u,v) as shown in Figure 54 and each view is rotated with respect to another by 135 degrees. Such chamber measures four coordinates of particle hits. The central part of the chamber has areas with different number of measured coordinates. As an example, Figure 55 shows the central part of a chamber (four views). To solve the left-right ambiguity, each of the views is made from four planes as shown in Figure 56 and each view contains 500 straws. All the views have identical design and contain straws with a maximum sensitive length of 2100 mm. The straws are separated from each other to guarantee the straw straightness. This is most important as the straw diameter changes with the difference in pressure between the inside and outside of the straws. The baseline for the detector gas is a mixture of CO_2(80%), Isobutan C_4H_10 (10%) and CF_4 (10%). This gas mixture was used in the test beam in October 2007.

The straw wall is 36 μm thick metalised Mylar. Two different coatings are understudy: the first option is a deposit of 50 nm of copper covered by 20 nm or 50 nm of gold. The second consists of 200 nm of aluminum, applied on both sides. A Mylar strip is formed into a straw

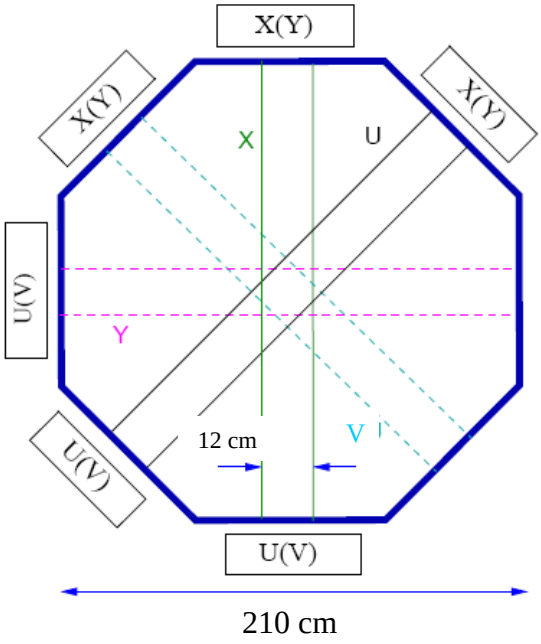

Figure 54: Schematic of the four-view chamber - (X,Y,U,V).

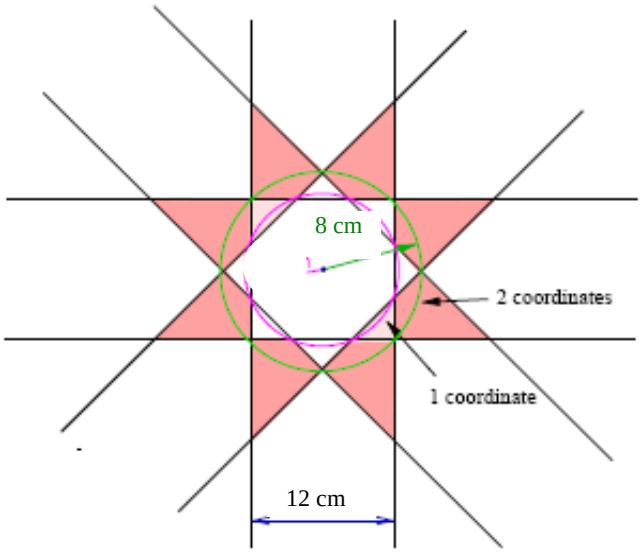

Figure 55: One and two co-ordinate regions.

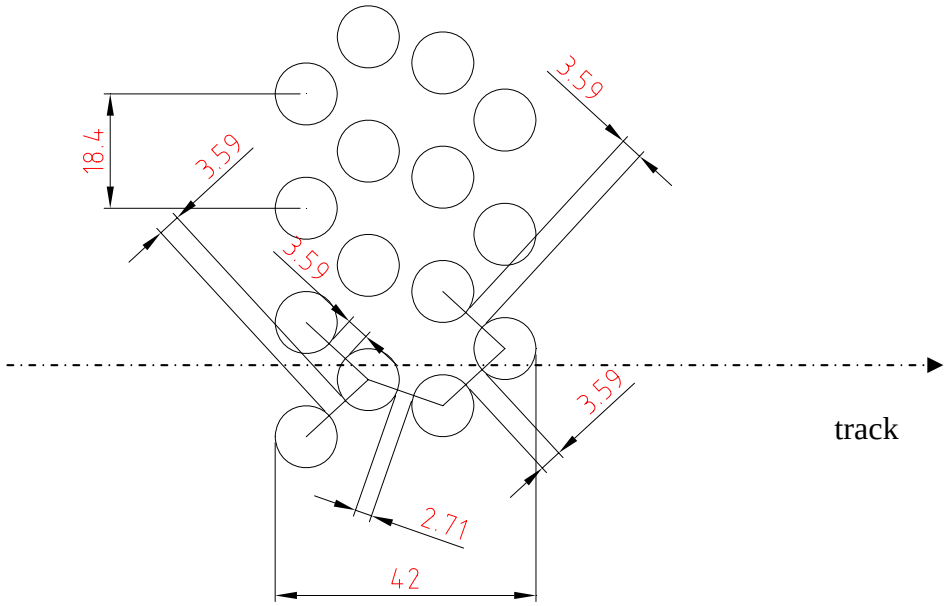

Figure 56: Layout with four layers of straws in one view.

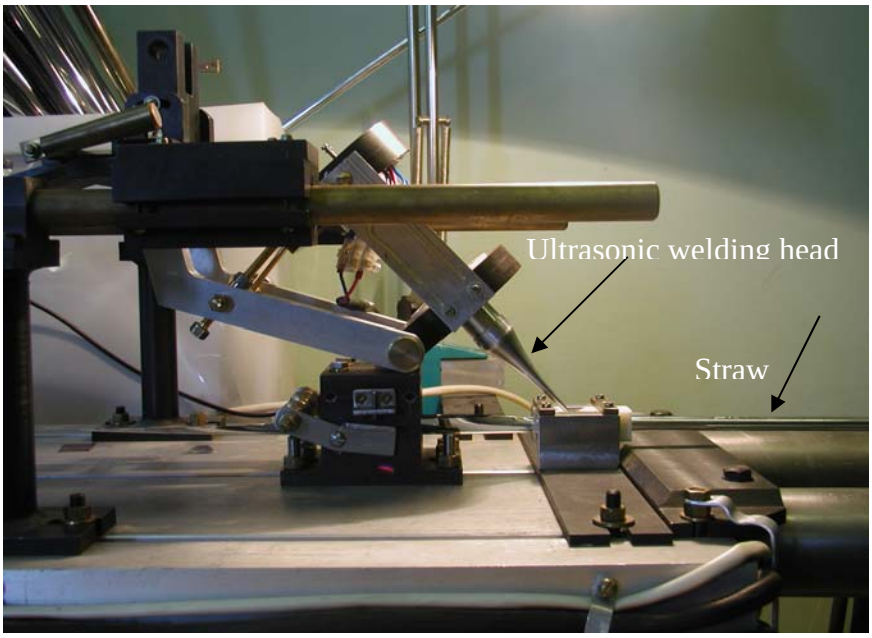

Figure 57: Ultrasonic welding machine for Mylar straws. The welding seam is straight and parallel to the straw axis.

using an ultrasonic welding machine developed for this purpose, as shown in Figure 57. This allows one to obtain a mechanically stable (no creep) tube as the welding seam is parallel to the straw axis. This is a very important improvement compared to the standard straw where two strips are wound together to form one tube. This new technique allows us to pretension the straws with 1 kg and guarantees constant tension in the straws over time. To study the effect of high-rate on the metal layers, high-intensity particle beams were aimed to the prototype during the October 2007 test beam run.

13.1 Prototype construction and beam test in October 2007

A 48-straw prototype was built in Dubna in the spring of 2007. A general view of the prototype is shown in Figure 58. The straws are fixed between an aluminum flange (also acting as vacuum seal) and an aluminum plate. Two intermediate straw partitions, not foreseen in the final detector, were used to support the straws. The prototype has eight layers with six straws per layer. Six of the layers were aluminised while the last two were gold-coated copper. The straw position was adjustment using a theodolite with respect to eight alignment points on the partitions and on the end-plates. The straw with the end-plug

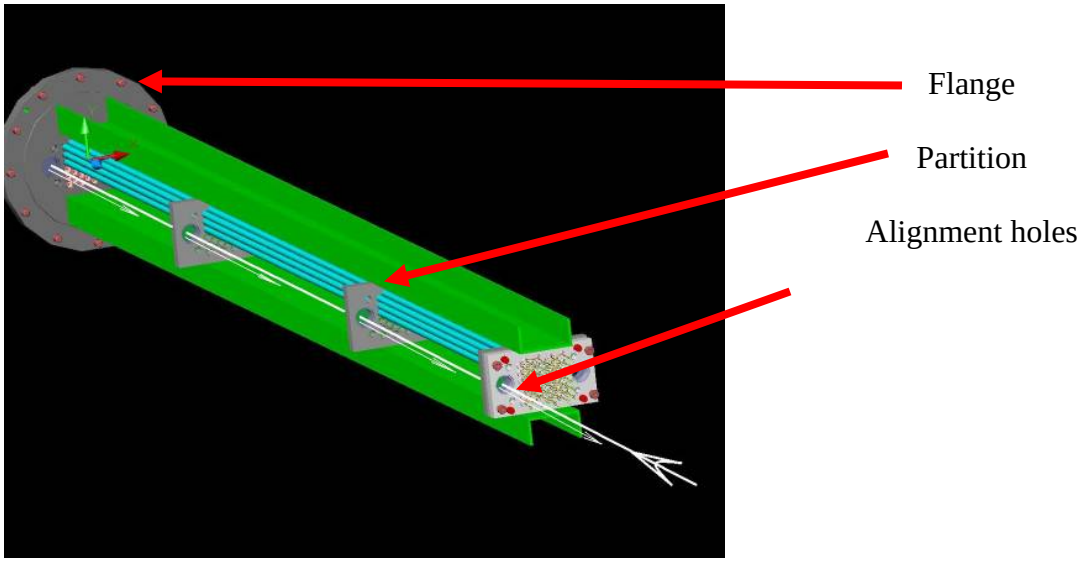

Figure 58: General view of the prototype.

is shown in Figure 59. A twister inside a plug was used for anode wire centring and a small cap was used for protection against HV discharges. A gas tube was used to connect the 48 straws in sequence. The fixation of the anode wire was made by soldering at both ends (crimping may be used later) and glued to the Ultem insulator. The gas tube was glued at the same time to provide the leak tightness.

The gas leak was measured in vacuum for each straw at an over pressure of 1.5 bar using N_2. The result is presented in Figure 60. The total gas leak from 48 straws was 0.1cc/min. It is important to notice that 27 straws have a leak of only 0.001 cc/min per straw. The straws were flushed with CO_2 at atmospheric pressure during the whole duration of the leak measurement. Before stopping the pump, the vacuum outside the straws reached 2.7x10-4 mbar. Then, after 180 minutes the increase in pressure was measured to be 1.45 mbar, which gives a gas leak in the prototype of 0.6 cc/min.

As mentioned earlier, the straws are separated from each other to guarantee the straw straightness (see Figure 61. This is most important as the straw diameter changes with the difference in pressure between the inside and outside of the straws. The gap between neighboring straws was measured to be 1.2±0.1 mm.

The cathode resistance was measured for both the aluminum and gold plated straws to be about 40 Ohm (Figure 62). Some straws have higher resistance due to a problem with the contact between the straws and brass plugs. The gold plated straws have a resistance of

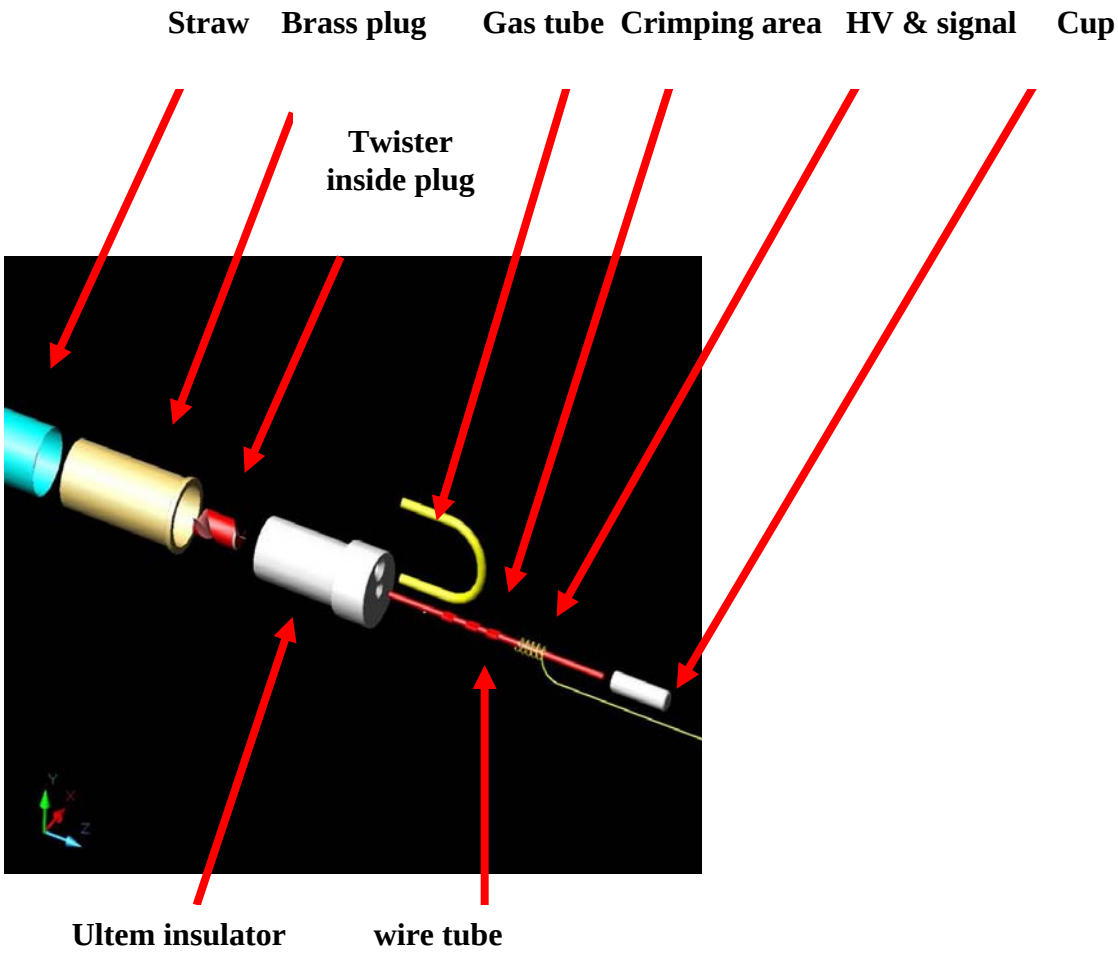

Figure 59: Details of the end-piece.

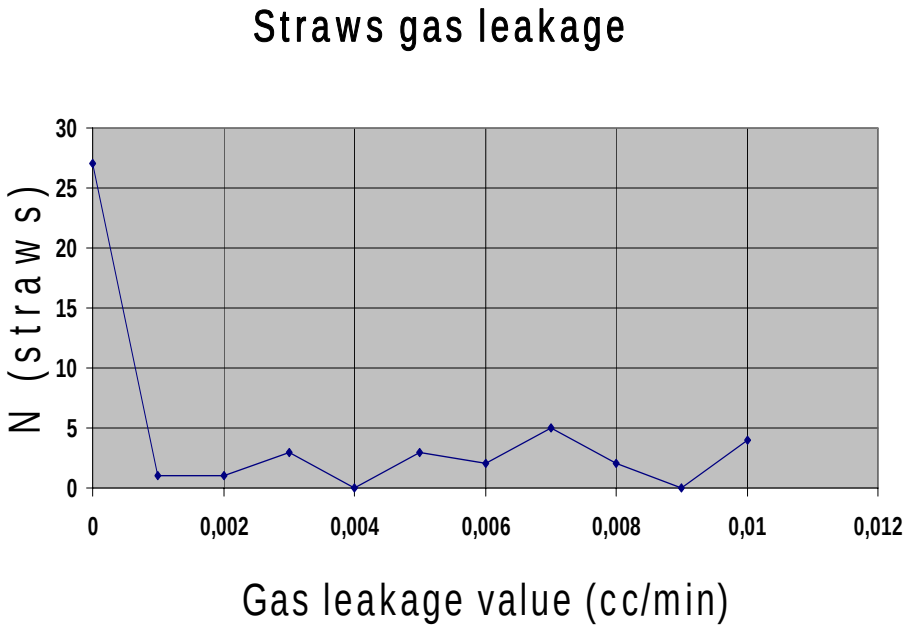

Figure 60: Straws leak measurement with $N_2$2 at an over pressure of 1.5 bar.

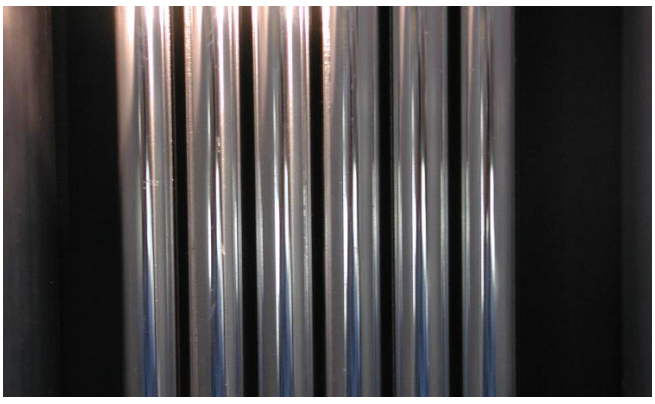

Figure 61: A prototype straw layer has a nominal gap between neighboring straws of 1.2 mm.

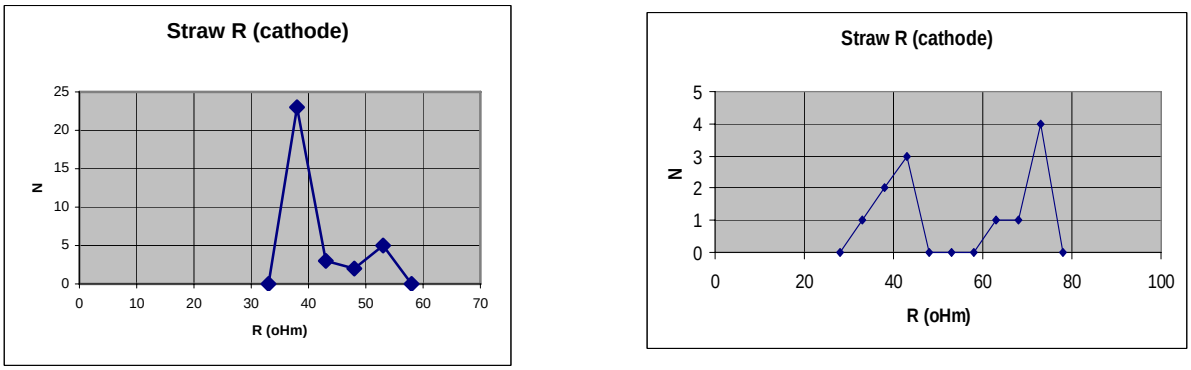

a) **b)**

Figure 62: Cathode resistance distribution: a) aluminum straws and b) gold plated straws.

40±10 Ohm and 70±10 Ohm due to the different gold thicknesses (50 nm and 20 nm). The copper thickness was 50 nm in both cases.

The anode wire tension for the 48 straws was measured and the results are presented in Figure 63. The tension is 80±10 gram except for four wires. Gold plated tungsten/rhenium wire with a diameter of 30 m was used for all the 48 straws (Luma, type 861). The elastic limit is 140 gram and the breakdown limit 190 gram.

A view of the Dubna cosmic ray test set-up is presented in Figure 64. An iron filter was used to remove muons with an energy below 0.5 GeV. For triggering, two layers of scintillators (The NA48 charged hodoscope) were used and each scintillator had a surface of 0.7 m^2. The time resolution had an r.m.s of about 2.5 ns.

The prototype was operated with a high voltage of 2.8 kV and a threshold of 5 fC for the cosmic muons run. The residual distribution with 6 hits per track is shown in Figure 65. To is calculated for each straw individually and the wire position is corrected for when the wires has an off-set above 100 μm. The r.m.s of the distribution is about 180 μ m and the σ is found to be 92 μm.

After the test with cosmic rays during the summer, the prototype was transported to CERN in September for the October 2007 test beam. The goal for the test beam was to study:

- The spatial resolution and efficiency for different high voltage and threshold settings.
- The operation of the prototype in vacuum.
- The survival of the aluminum and gold metal coatings under high rates.

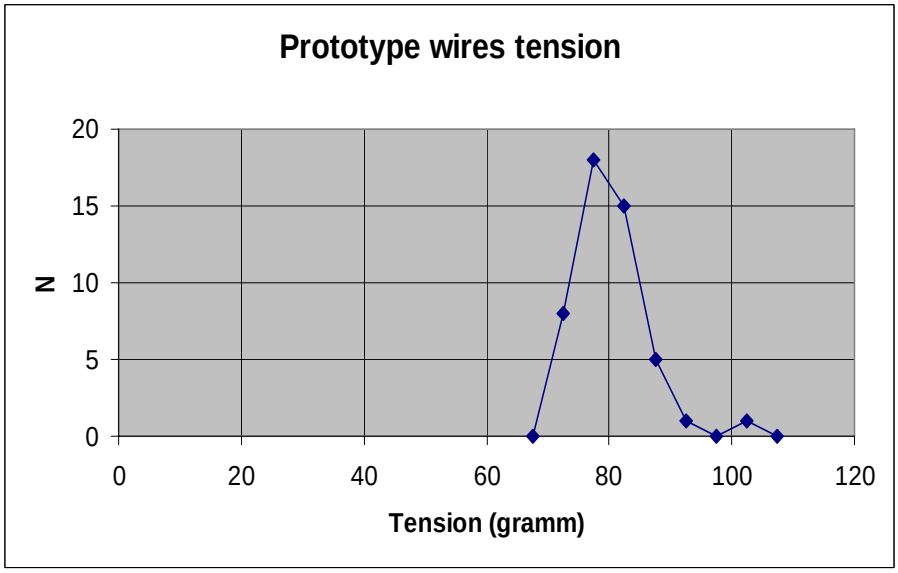

Figure 63: Distribution of the anode wire tension for the 48 straws.

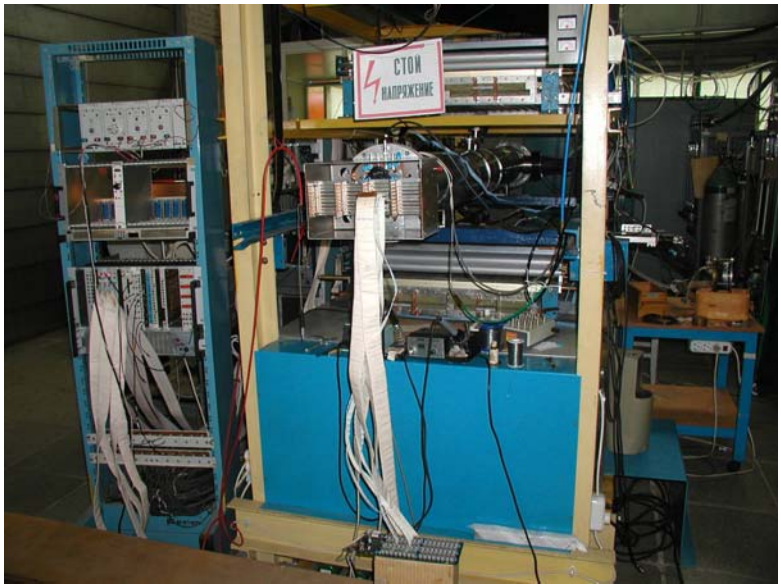

Figure 64: A view of Dubna comic ray test set-up.

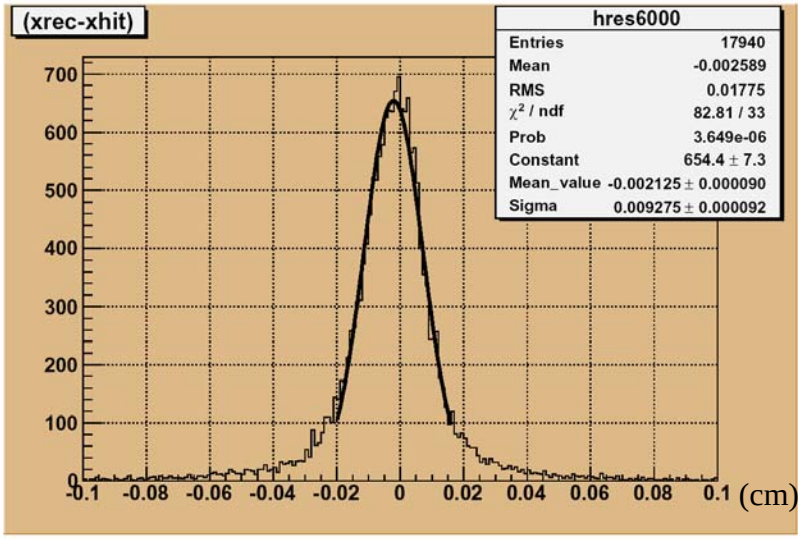

Figure 65: Residual distribution for cosmic rays with six hits per track.

In Figure 66 is shown the prototype as installed 15 cm from the nominal beam axis. The prototype was successfully operated in vacuum for two weeks and the first results on the space resolution (residuals) are shown in Figure 67. Events with 6 hits per track were used and the prototype was operated with a high voltage of 2.4 kV. The threshold was set to 6 fC. To is calculated for each straw individually and the positions of the wires were recalculated. The r.m.s of the residuals is about 88 μm and the σ from the 2 Gaussian's fit is 45 μm. The detailed analysis of the data is continuing.

A high rate run to study the effect on the cathode coating (aluminum and gold) was carried out using a pion beam. The maximum rate was about 500 kHz per straw (over a length of 2 cm) and the current 3-4 μA for a maximum gas gain of about 10^6. The high voltage was set to 2.8 kV and the prototype was operated at this rate for one hour without discharges or trips. The effect of the radiation on the straw metal layer will be studied once the prototype is removed from the experiment.

13.2 A new design of the straw elements

In parallel with the test of the straw prototype, a new design of the straw end-pieces and the electrical connection to the straws is under development. The main modification is the replacement of the soldered connections to the wire and straw by Kapton web circuits, as shown in Figure 68. The aim is to improve the quality and yield in the mass production and

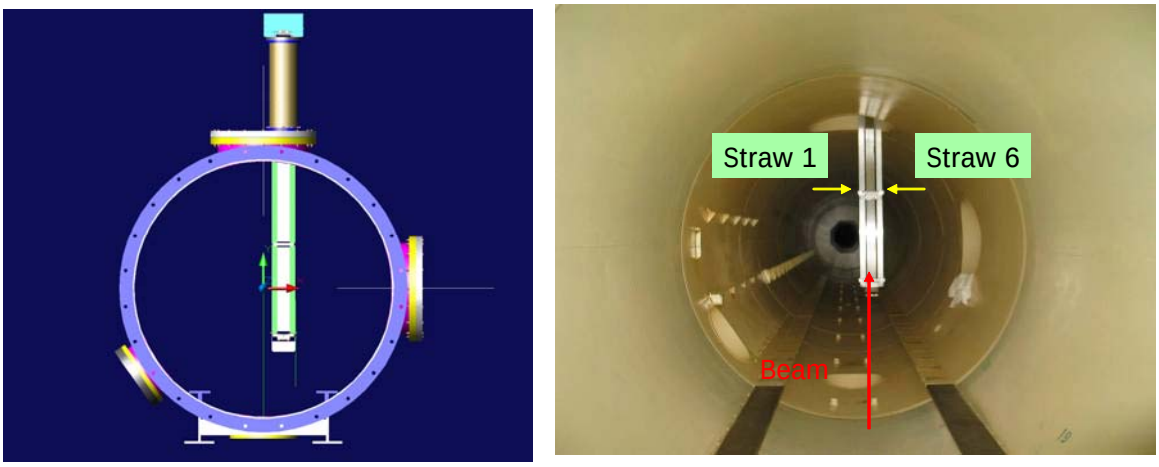

Figure 66: The 48-straw prototype installed in the 2.3 m in diameter vacuum tube.

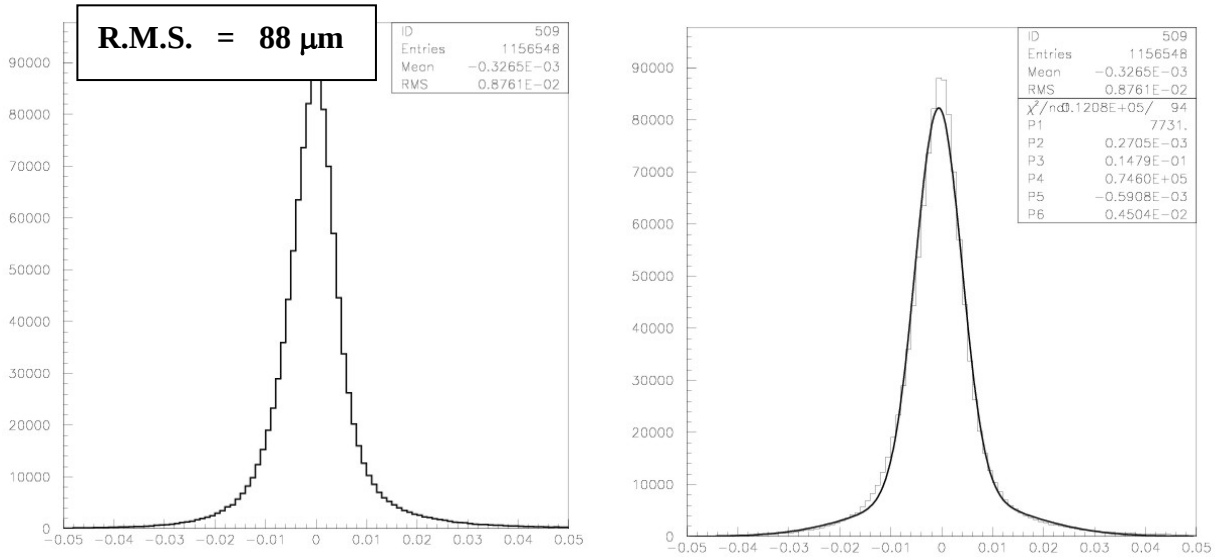

Figure 67: 16: Residual distribution a) from data taken in the 2007 test beam using muons and fitted by two Gaussians b).

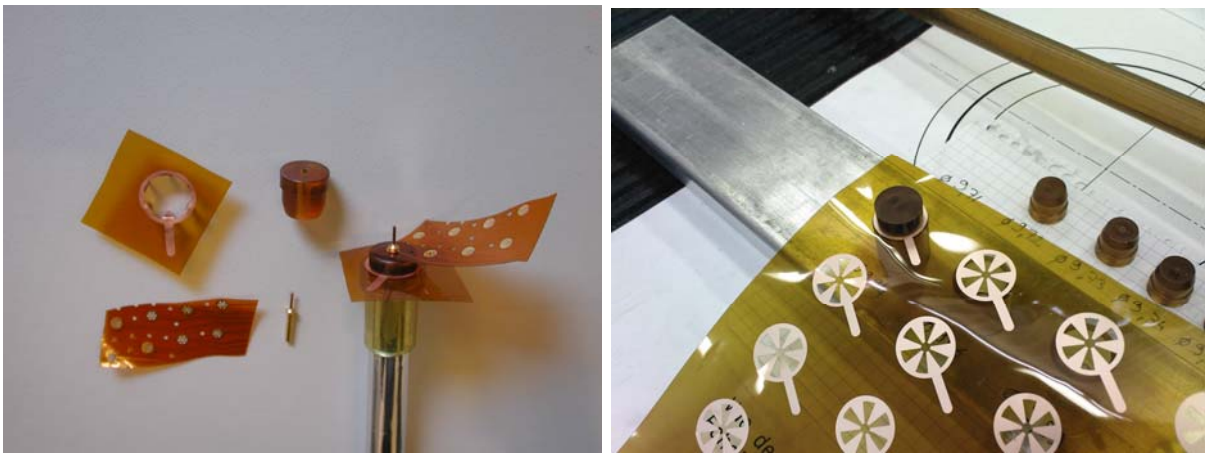

a) b)

Figure 68: a) Prototypes of the Kapton circuits and straw end-pieces for electrical connection to the straw and b) the Kapton circuit with the margaritas before the plugs are inserted.

to the simplicity the electrical connections to the straw and wire. In addition, the routing of the signals to the front-end electronics and the high voltage distribution is simplified. A new wire guide is also under study. I consist of a twister inserted into a six-sided piece (like a *nut*) as shown in Figure 69. The straw diameter has a spread due to the manufacturing process and these new wire guides can comply with this difference (9.7-10.0) mm.

13.3 Time scale and cost

Indicative time scale and cost are summarised in Figure 70. A preliminary project plan was worked out to show how the straw tracker construction can fit to the overall schedule of the proposed experiment.

Figure 69: The new wire guide in Ultem.

	Number	Unit cost (CHF)	2007(kCHF)	2008(kCHF)	2009(kCHF)	Total (kCHF)
Detector element						
Straws	8000	25	20	200		220
Straw end-pieces and crimped joints	24000	1.5	3.6	36		39.6
Wire (m)	19200	0.5	0.1	4.7	4.8	9.6
Tooling			5	50		55
Frames , mechanical support	16	20000		160	160	320
Prototypes				50		50
Electronics	8000					
Front end electronics						275
HV power supplies						250
Gas and cooling systems						250
Total						1470
Read-out electronics					750	750

Figure 70: Construction Cost Estimate.

14 Trigger and DAQ

The existing NA48 trigger electronics was designed more than 10 years ago using (then) new technology; the design was tailored to the specific needs of the direct CP violation measurement: in particular the part dealing with calorimetric information featured innovative and successful dead-time-free pipelining techniques, but overall the system provided trigger algorithms rather focused toward the detection of two pion final states. Such electronics can no longer be used for a new experiment, either because it is not suited to the new sub-detectors or, for those parts of the NA48 setup which will be kept, for reasons of insufficient performance with the higher beam flux and foremost lack of support. Moreover, for a large part of the electronics, notably the calorimetric trigger system, the design is strictly coupled to the front-end or digitizing hardware, which will also have to be rebuilt for the same reasons. It seems therefore that most of the existing trigger/DAQ system will have to be rebuilt.
The intensity of the K^+ beam for the new experiment will be roughly 30 times higher than the one due to the sum of the two charged beams used in NA48/2. The single-track rate for the NA48/2 experiment was in the MHz range, to be compared with a final trigger (and read-out) rate of order 10 kHz, as limited by the design of hardware components. For the new experiment a rate one order of magnitude higher is expected, originating from kaon decays in the vacuum tank and a muon halo from upstream decays; the global reduction factor by the trigger should be at least a factor 10 higher than in NA48.
The above considerations clear the way to considering the design of an appropriate trigger system without compromises driven by needs of re-using existing electronics. On the other hand, given the time scale for the experiment, it is clear that adopting solutions already developed for other experiments - wherever feasible - is a must.
For the design of the new experiment's trigger system one should keep a rather far-looking approach, allowing also:
- adaptation to emerging requirements as the experiment design finalizes;
- future upgrades of the read-out bandwidth to allow adjustments to possible higher intensities;
- a reconfiguration to adapt the system to further kaon physics programs.
Much more detailed information on all the issues discussed below can be found in a recent internal note of NA62 which describes the present status of the trigger and data aquisition design [31].

The purpose of the trigger system is to reduce the rate to a manageable level, rejecting as

much as possible all main decay modes of the K^+ and beam backgrounds while affecting in a minimal way the $K^+ \to \pi^+ \nu\overline{\nu}$ signal.

In view of the difficult task of the offline analysis, which will have to exploit strong and redundant cuts to suppress backgrounds, special care has to be taken in using trigger cuts which should ideally not introduce any correlation between different sub-detectors, so that sets of cuts can be developed offline which are known to be effectively independent.

A satisfactory compromise has to be found between the simplicity of the trigger and the need to effectively cut down the very high rate.

In this respect, the best approach seems to be one in which the trigger cuts are performed as much as possible in software, using a system of commercial processors connected with high speed data links which process the actual sub-detector event data. This scheme, which is being adopted by most modern particle physics experiments, presents several advantages over the traditional approach of a hardware trigger tailored to the specific reaction under study.

Two of the main advantages of a software-based approach are flexibility - since the optimisation of the trigger algorithms can be decoupled from their implementation in the trigger infrastructure - and scalability - since by replacing commodity processors and links with new, more powerful, ones appearing on the market, the system capability in terms of data throughput and trigger versatility can be increased without any major redesign, therefore allowing a longer lifespan for the system.

These two points are particularly important for a rare decay experiment, in which the optimisation of the trigger can be a lengthy and delicate issue, making a big difference in the quality of the final result, and in which the capability of the sub-detectors to stand high particle rates should be well complemented by the capability of the trigger system of allowing the highest bandwidth. The fact that the events of interest are very rare does not mean, unfortunately, that a small set of data has to be collected, since very selective cuts cannot be performed safely except when the full information from the detector (in terms of granularity and calibration) is exploited, which means in the offline analysis.

The cost is also an important factor, since the need for development (and maintenance) of experiment-specific electronics is kept to a minimum. The control software of the system is in this case also more user-friendly and easily maintained than for a specific custom hardware system.

When the above concept is brought to its extremes one has the scheme of a completely "triggerless" readout, in which the sub-detectors are read-out continuously, following some

strobe signal which could even be a simple periodic clock. The appeal of such a scheme lies not only in the fact that the above issues of flexibility and scalability are maximized, but also in that it allows having a single path for event data also serving for trigger purposes, in contrast to the traditional approach in which a separate and parallel "trigger branch" is required.
In the case of a high-flux fixed target experiment with a debunched beam, there is no intrinsic time strobe signal to indicate the possible occurrence of an interesting event, and continuous digitisation at the frequency of an experiment clock suited to detector sampling leads to rates which are way beyond the capabilities of reasonable data aquisition systems. This means that a low level hardware trigger will be anyway required, but one would like this Level 0 trigger to be as simple as possible, and just sufficient to reduce the rate to a level which allows complete readout of the sub-detector data into PCs, where further trigger processing (possibly multi-level) is performed.

We plan to use a multi-level trigger system in which only the first level (L0) is implemented in hardware, and consists in rather simple conditions, mostly simple tight coincidences of detectors with excellent online time resolutions, some of them possibly providing minimal hit-pattern information. The complete sub-detector data would be read-out at this L0 trigger rate, possibly after online calibration and data compaction, to buffer memories, most likely PC memory banks, through high-speed point-to-point data-links.
The following trigger stages would be performed in software by a farm of processors interconnected through a high performance switching network, reconstructing and analyzing either data from a single sub-detector (L1) or the complete event data after event building (L2). Each of these trigger levels might be itself implemented as multi-level software processes to optimize the performance. Figure 71 shows a simplified block diagram of the proposed scheme and figure 72 indicates the common electronics.
Both L1 and L2 might be performed in the same processor array or in different ones, depending on how the topology of the switching network is optimized for throughput. We envisage to have a first layer of CPUs receiving the data from sub-detectors (or parts of them) via dedicated links, and performing further "local" computations on event fragments to provide informations to a central L1 trigger decision processor, before event building, while the following part of CPU farm is used for L2 trigger based on algorithms working on complete events.
Events sitting in PC memories and surviving all trigger stages will be logged to disks and sent through links to the Computing Centre for subsequent archiving in Central Data Recording,

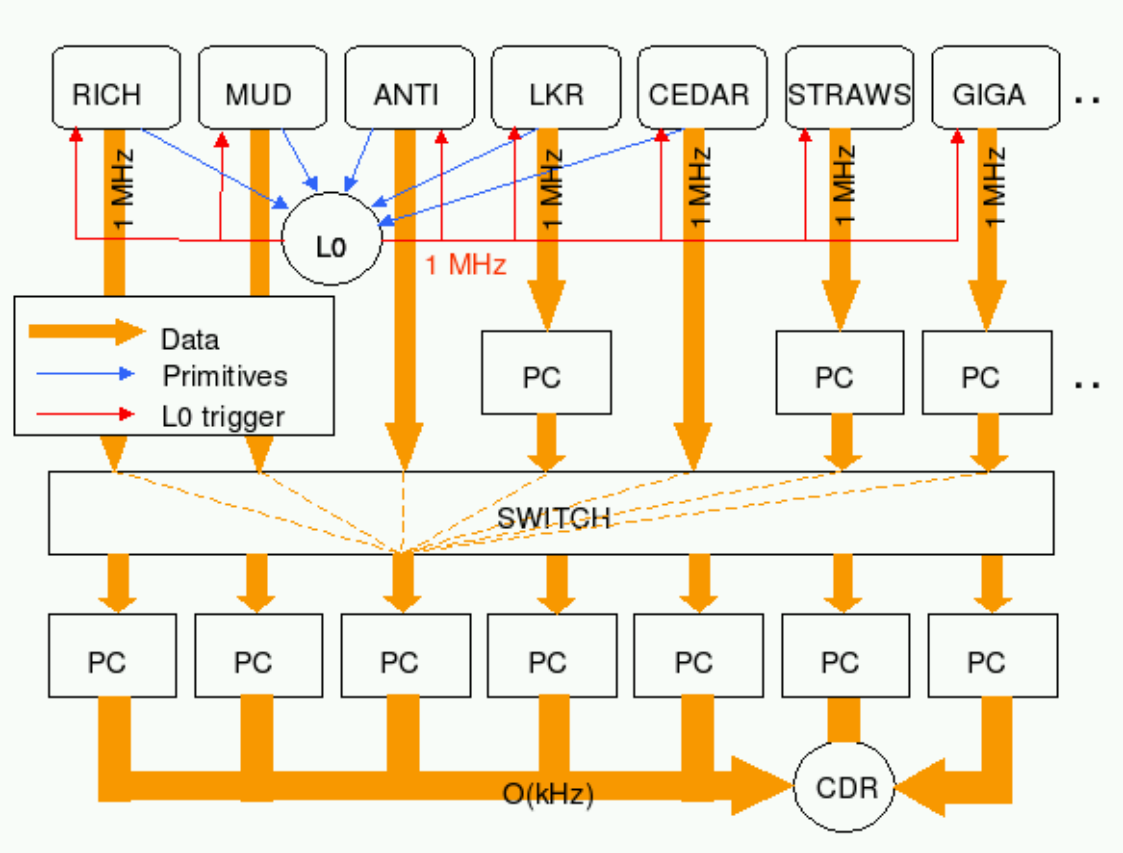

Figure 71: Simplified sketch of the NA62 trigger/DAQ.

as done for NA48. Further processing for either data reduction or monitoring might take place there, if required, before tape logging, again as was done in NA48.
An important issue, concerning the wish to keep the development of experiment-specific electronics to a minimum, is the effort which we plan to make toward adopting common electronics for different sub-detectors as much as possible. It seems that, apart from special cases obviously requiring *ad hoc* solutions (as is the case of the Gigatracker), most other sub-detectors could profit from the use of some flexible common digitisation and hardware processing board, maybe exploiting in part systems developed for other experiments.

For this experiment, the rate in the detector will be due to K^+ decays and muons from the beam halo, integrated over the surface of the detector. All kaons decaying between the final collimator and the detector contribute to such rate, even if only the upstream region will be used as fiducial region for the signal. We expect about 11 MHz of kaon decays occurring upstream of the main detectors. Such decays occur without any significant time structure due to slow-extracted nature of the SPS beam; this implies that there is no minimum time

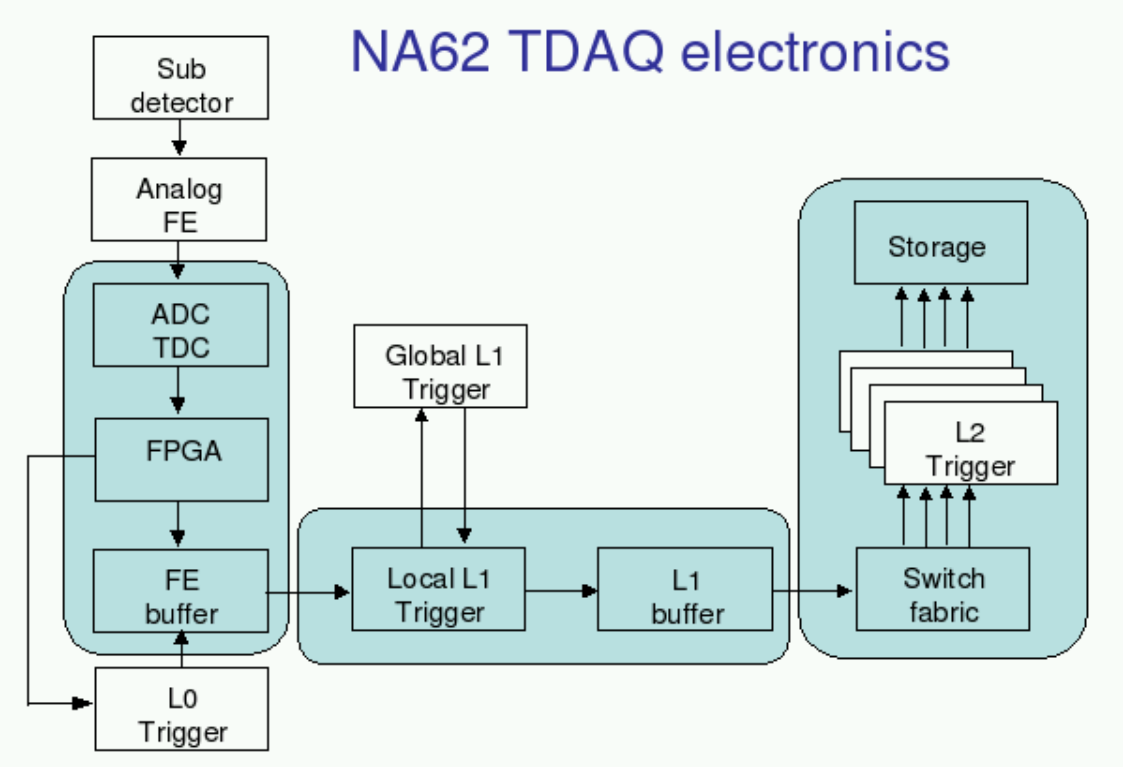

Figure 72: Conceptual scheme of the NA62 electronics. Blue items are those which are not subdetector-specific.

interval between decays, and also that there is no intrinsic time reference signal to indicate the possible presence of an interesting event occurring at any time (in contrast to collider experiments or experiments with bunched or micro-bunched beams). The rate indicated above assumes an effective spill length of 3s for a 4.8s flat top, as suggested by the NA48/2 experience.

The total number of channels for the experiment can be roughly estimated as 55,000 (pixels) + 13,500 (Liquid Krypton calorimeter - LKR) + 8,000 (straws) + 2,000 (RICH) + 2,500 (LAVs) + at most a few thousands for the rest = less than 100,000 in total. The occupancy is very low for the interesting events; for most of the channels the information is time-like and therefore intrinsically reduced by the front-end TDCs.

The working approach is to reduce the rate to below 1 MHz in L0 and read all sub-detectors at this rate.

The most crucial figure is the average data bandwidth requirement for read-out, which determines the number of front-end PCs, those directly connected to the front-end, depending on the link capacity used. At a given trigger rate this depends on the event data size, which

is another delicate issue for this particular experiment. The quality of the experimental result of the experiment will depend on how well one will be able to suppress backgrounds at a very high level; in final offline analysis this task would profit by the use of all sub-detector information available, meaning that for the small final event sample one would like to have the complete detailed detector information.

Several sub-detectors will only provide (possibly multiple) time information, and only need to be equipped with TDCs, in such a way providing a self-defined autonomous data rate bounded by the sub-detector hit rate, and further reduced by reading them only at the (lower) trigger rate. For other sub-detectors in which both time and pulse-height information is required, continuous signal sampling with flash ADCs is a more effective approach with respect to using two (time and charge) measurement branches; in this case there is no hit self-detection, the triggerless data rate is prohibitive and also the triggered one can be very large depending on the number of channels being read and the zero-suppression scheme.

For the present NA48 electromagnetic liquid Krypton calorimeter, with 13500 channels sampled at 40 MHz, even assuming a new digitisation scheme in which the sample information is compressed to 8 bits (*e.g.* exploiting the reduced dynamic range of photon energies, since NA48 adopted a non-linear 10 bit encoding corresponding to about 14 effective bits), at the same 40 MHz sampling frequency results in a 540 GB/s raw data rate and about 100 GB/s for a 1 MHz trigger rate assuming 8 samples are readout as in the most recent NA48 data taking periods.

Such data rate could be easily reduced by a significant factor by applying zero suppression, the possibility of not doing this at all (or at least not until the data has been transferred to PCs) and keeping the whole sub-detector information is being considered. The first reason for evaluating this is that zero suppression is inherently a difficult task, in that to avoid compromising the excellent energy resolution it has to be performed by a system which has an overall view of the whole sub-detector at some level, which is easy in software but requires some degree of interconnectivity among front-end read-out boards when performed there. Secondly, for this specific experiment the electro-magnetic calorimeter is mostly (but not exclusively) used as a veto, and one would like to avoid any chance of suppressing possibly significant information from it at an early stage. Still, even if hardware zero suppression is not performed before read-out, lossless data compression implemented in hardware would most likely reduce the above data rate by a significant factor, which has to be evaluated with realistic conditions and algorithms.

With respect to the above data rate from the electromagnetic calorimeter, the other sub-

detectors are expected to be less demanding, either because of the limited number of channels, or because of the intrinsic data sparsification. As an example, a single silicon pixel station with 18K channels, despite the huge particle flux (1 GHit/s), considering a "large" (large with respect to the expected sub-nanosecond time resolution) read-out window of 50 ns and 4 bytes of hit time and channel information, delivers about 1 GHz $\times$ 50 ns $\times$ 1 MHz $\times$ 4 bytes $\simeq$ 200 MB/s, for a 1 MHz trigger rate. Data rates from most other sub-detectors are estimated to be significantly lower than this.

The size of the non zero-suppressed electromagnetic calorimeter data block would be about 110 kB per event, and an upper bound for the event data size could be estimated as 150 kB. The total data volume written to permanent storage for a single burst depends on the data logging rate capability. In this respect it is important to note that, quite differently from collider experiments, this experiment will have a duty cycle of about 30% (dictated by the machine extraction, and this leaves a significant amount of time for off-spill data streaming. Lately, NA48 used to log to tape about 5×10^4 events per spill, corresponding to an average 370 MB/spill, written to tape in the Computing Centre over the full 16.8 spill period. Such data rate was obviously limited by the experiment read-out bandwidth and not by the data logging capability.

For the unrealistically conservative event size of 150 kB (15 times that in NA48), even a 100 kHz final trigger rate (*i.e.* an unrealistically low trigger rate reduction of just a factor 10 on top of L0) would correspond to 15 GB of data for the entire spill. This shows that buffer memory requirements are not a big issue. On the other hand, a data logging rate as that for LHC experiments, around 100 MB/s (it was $\sim$ 30 MB/s for NA48) would correspond to a final event rate in the kHz range for the above large event size. From this point of view, the product $f_S f_R$ of event size and trigger rate reduction achieved by software triggers with respect to L0 should therefore be of order

$$f_R \times f_S \gtrsim 1500 \times \frac{\mathrm{L0\,rate}}{1\,\mathrm{MHz}} \times \frac{\mathrm{L0event\,size}}{150\,\mathrm{kB}} \times \frac{100\,\mathrm{MB/s}}{\mathrm{Tape\,logging\,rate}}$$

meaning *e.g.* a software trigger rate reduction by a factor 50 for a 10 kB event size and 200 MB/s tape logging rate at design conditions.

The requirements in terms of computing power depend strongly on the hierarchical way in which the algorithms are implemented. Sophisticated high-level trigger algorithms for LHC experiments working on complete reconstructed events are benchmarked to perform in (few) ms on modern CPUs. NA62 events will be significantly smaller and simpler, with a vastly inferior detector occupancy. An educated guess of $\sim$ 1 ms overall computing time per event (as a weighted average of software trigger levels involving algorithms with very different level

of complexity and the use of different parts of the event data) would require order ~ 100 of today CPUs, a small number by todays' standards (CPU performance is of course expected to increase by the time the experiment starts, but so are the computing requirements posed by the experiment). Little insight on the above numbers can be obtained from real measurements on existing data and algorithms, since the existing NA48 reconstruction software is definitely not optimized for online applications.

The L0 trigger will of course require a positive signal in the RICH corresponding to at least one track crossing it. Such signal must have very good online timing properties, allowing tight coincidences with veto systems. Hit multiplicity information can be easily provided too, which could help in reducing the rate from $\pi^+\pi^+\pi^-$ decays, but this is a minor component to the total rate and its impact is not expected to be significant. The online use of more refined RICH information, such as ring radius, could in principle help in muon rejection: this is considered impractical because of the difficulty of performing pattern recognition online and the fact that a momentum measurement input (*e.g.* from the spectrometer) would also be required, and as such not pursued.

A large fraction of K^+ decays contain a muon in the final state, and so the use of a muon veto in the L0 trigger will be essential; this of course requires an appropriate online time resolution to limit the random vetoing, and will get rid of the muon halo as well. As the online time resolution of the main muon veto detector will not be enough to allow a tight veto coincidence window with good rejection power, a faster segmented plane is foreseen for trigger vetoing purposes.

Besides $\mu^+\nu$, the next large decay mode contributing to the rate is $\pi^+\pi^0$, which can be reduced somewhat by using the large-angle photon vetos (LAV), but in a more substantial way by exploiting the electromagnetic calorimeter. Cluster counting at the trigger level would be useful in this context, but since a signal event has at most one cluster in the electromagnetic calorimeter, simpler conditions not requiring a complex (hardware) trigger processor could be used at L0. In NA48 a dedicated pipelined trigger system was used which continuously computed the first three energy moments and performed cluster counting working on mono-dimensional projections with a 4 cm (2 cells width) granularity. While a new hardware system with those capabilities (or more) would allow a stronger rate reduction at L0, for the present purpose it seems that a fast computation of quantities which do not require clustering algorithms could be enough. Examples are the total energy deposit over the full detector as well as over quadrants; these quantities could be continuously computed online in the FPGAs which will follow the digitisation stage to handle tasks such as online

calibration, pedestal subtraction and data compression. A pipelined summation tree is all that is required, and one can envisage that energy sums can be available with short latency. The use of small angle photon vetos and charged veto counters could also be foreseen, to help reducing further the rate from multi-body final states, but their additional impact on rate reduction is minimal.

With a muon veto trigger system with an adequate online time resolution, most of the trigger rate will be dominated by kaon decays, and the inclusion of the CEDAR in the trigger will not be required, avoiding some difficulties due to the location of this sub-detector being far upstream with respect to the rest of the detector. On the other hand it should be kept in mind that for a 10 MHz muon hit rate a coincidence window of 5 ns already corresponds to 5% dead time due to random vetoing, and one should not exclude that the kaon tagging signal from the CEDAR is used in the L0 trigger to help rejecting halo muons.

A central hardware L0 unit should take care of synchronizing the various sub-detector signals participating to L0, and the pattern (and its time history) of such signals should be recorded and made available into the event data. Without very strict constraints due to buffer memories, the maximum time latency of the L0 trigger is defined to be 1 ms, allowing ample time for its formation and delivery to distant sub-detectors.

For a rare decay experiment such as this one it should be clear that a significant fraction of the trigger bandwidth should be reserved to collecting down-scaled control triggers, with far less stringent conditions, which will be required for the offline study of correlations among different cuts. Such trigger down-scaling should be done both in the central hardware L0 system and (with ease) in the following higher-level software triggers.

Calibration triggers should also be collected of course, and a peculiarity of this experiment lies in the need for special monitoring triggers, which should be recorded continuously in order to allow an accurate offline check of the live-state of the sub-detectors and their read-out chain: this is a crucial issue, since a very small undetected inefficiency in just part of the system (such as a part of the veto system) could jeopardize the result.

Finally, ancillary (down-scaled) triggers will also be implemented in order to collect significant samples of less rare K^+ decay modes for other physics measurements: this point requires further study, but at first sight it seems that allowing a fraction of higher track-multiplicity events, corresponding to decay modes with 3 charged tracks in the acceptance, would be the most interesting possibility, with less interference with the signal trigger.

Rough MonteCarlo simulations have been performed to estimate the rate reduction which can be expected for L0 by using simple cuts using minimal correlation among detectors.

K decay rate	1.0	
>1 hodoscope hit	0.65	64% $K_{\mu 2}$, 21% $K_{\pi 2}$
Muon veto	0.22	58% $K_{\pi 2}$, 16% $K_{\pi 3}$, 12% K_{e3}
Large angle photon vetos	0.14	56% $K_{\pi 2}$, 26% $K_{\pi 3}$, 11% K_{e3}
RICH track multiplicity < 2	0.11	-80% of $K_{\pi 3}$
EM energy < 50 GeV	0.04	-65% of $K_{\pi 2}$
No EM opposite quadrants	0.03	-95% of $K_{\pi 2}$
No EM opposite quadrants and E< 50 GeV	0.02	-96% of $K_{\pi 2}$
< 2 particles in EM	0.02	-99% of $K_{\pi 2}$

Table 17: Expected rate reduction with some L0 cuts. All cuts in the upper part of the table are applied in cascade, while the lower part of the table shows the rate reduction (with respect to the total K decay rate) with only a single cut applied on top of all those in the upper part. Muon halo from upstream decays is not included.

Event rates were evaluated by normalizing to a 11 MHz kaon decay rate, including all major decay modes, in the region between the last collimator (the acceptance drops rapidly to zero for decays upstream the final collimator, even when just single-track event fragments are considered) and the LKR calorimeter.

Table 17 shows the relative data reduction which can be obtained with some of the cuts which might be performed in a rather simple hardware L0 trigger system. This is shown graphically in Figure 73.

In the above estimates the cuts have been simulated in a very crude way, taking into account the EM shower size as an effective radius of 10 cm and an energy threshold of 2 GeV; since the hadronic shower produced by the π^+ in the signal can extend over large distances in the calorimeter, a simple quadrant cut can be rather inefficient in some regions, and a better approach would be a check on the number of quadrants hit when the calorimeter is subdivided along two orthogonal lines either top-bottom and left-right, or along the bisectors of the former, requiring that at least in one of such sub-divisions there are less than 2 quadrants being hit. The EM energy cut at 50 GeV is of course compatible with the cut on π^+ momentum which is foreseen to suppress background.

The above estimates indicate that the rate could be reduced to below 1 MHz without actual cluster counting in the EM calorimeter, therefore allowing to consider a rather simpler L0 hardware processor; real (bi-dimensional) cluster counting would further cut the rate by

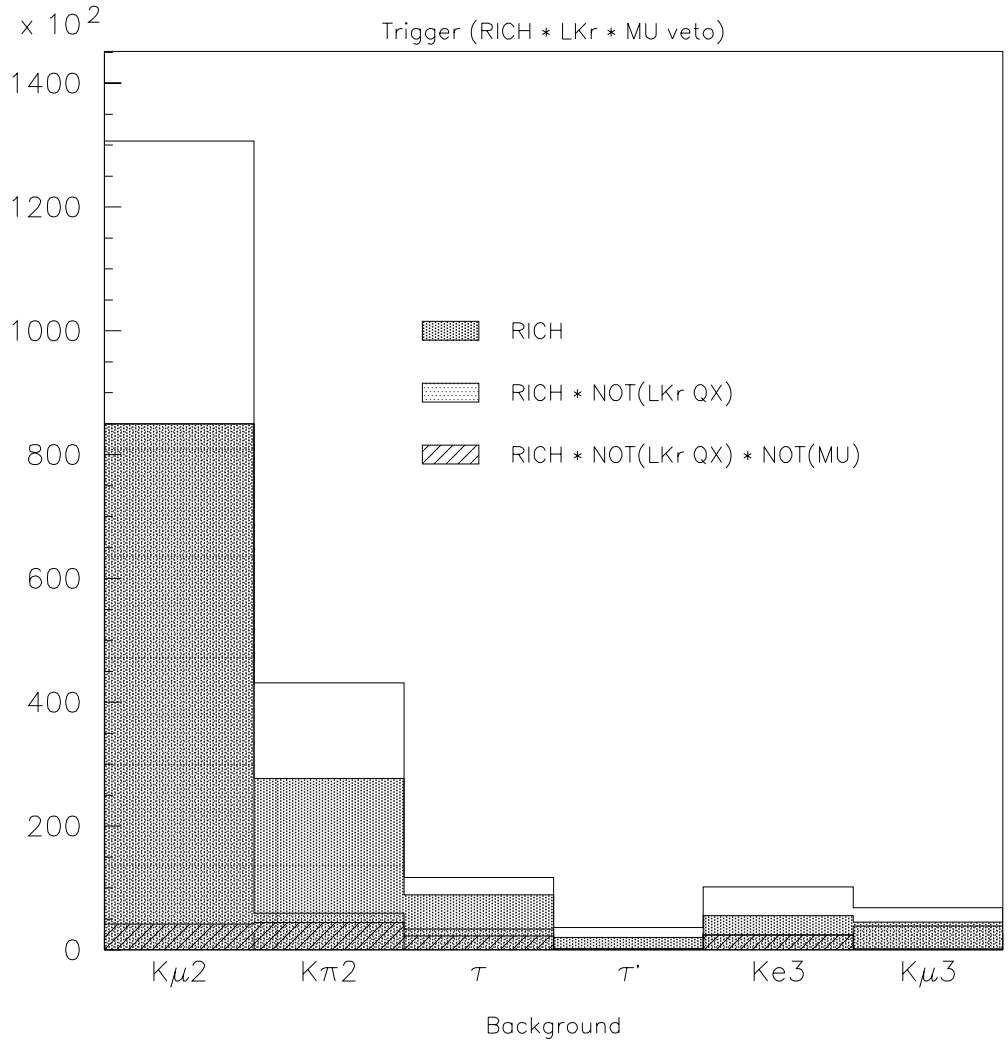

Figure 73: Cumulative reduction of different decay modes with some L0 cuts. The "LKR" cut is the "$<$ 2 EM quadrants" in Table 17.

maybe a factor 2 with respect to the above simple-minded cuts. Moreover it should be noted that the above cuts are examples of "local" computations which do not require exchange of information among different parts of the sub-detector, but rather just combination of information computed on sub-sections of it.

The use of the NA48 scintillating-fibre hodoscope embedded inside the LKR calorimeter was considered as an alternative to the LKR calorimeter for providing simple L0 conditions such as those discussed above. The advantage would be that only 32 channels rather than 13K need to be processed online for this purpose; unfortunately the neutral hodoscope (besides

having an intrinsic jitter due to $\sim$ 1m long counters) has a high inefficiency at energies below 15 GeV, resulting in the rate being tripled with respect to the corresponding condition as implemented by the LKR calorimeter, which is clearly a superior device. Moreover two of the neutral hodoscope channels are not working and would require re-opening the calorimeter to be fixed; taking moreover into account the fact that a LKR calorimeter capable of generating online some trigger primitives offers a large potential for other more refined cuts, and that the digital electronics for it has to be rebuilt no matter what, it seems that using it in the trigger is a profitable choice.
The upper multiplicity cut on the RICH is seen to be a rather marginal addition in terms of rate reduction.
Of course all the above assumes 100% veto efficiency (which even for fast sub-detectors means neglecting time tails in their response). The effect of a reduced online veto efficiency can be very important on the rate, the dependence on the inefficiency ϵ being crudely estimated to be $R(\epsilon) \sim R(0)[1 + 21\epsilon]$.
More details can be found in [31].
The above discussion by no means exhausts the L0 trigger studies, but was just meant to check that the above assumptions of a L0 trigger rate below 1 MHz is reasonably within reach with the use of a few sub-detectors and without requiring a too complex hardware trigger system. Further study is required to actually identify the best set of trigger primitives which are required to be computed online from the L0 electromagnetic calorimeter system, which will impact on the design of its read-out system.

The algorithms to be used in higher level software triggers require further study which is strictly linked to both the chosen L0 algorithms and the offline analysis strategy. Nevertheless, it is clear that by being able to cross-correlate sub-detector information, with the full power of software algorithms, much stronger data reduction factors can be achieved in a rather easy way.

Along the lines discussed above, since the time of the original proposal the collaboration started exploring existing solutions on which the development of an integrated trigger and data-aquisition system could be based to limit development efforts.
Three main areas were identified in which sinergy with LHC experiments and future developments can be easily exploited: the first is the clock, control and trigger distribution system, for which the TTC system [32] adopted by all LHC experiments seems a natural choice. The "40 MHz" frequency matches that of the experiment-wide clock used in NA48

and could be adopted in NA62 as well. The TTC capability of transmitting a (synchronous) trigger signal and a limited amount of data looks attractive to limit the number of signal distribution networks to the front-end systems, and the baseline solution therefore foresees synchronous transmission of L0 trigger (after re-synchronisation in the central L0 processor), complemented by 8-bits of trigger type word. The use of the TTC would require a detailed assessment of the availability of modules and components on the timescale of the experiment, or possibly the re-building of some of those: synergy with LHC experiments and their future upgrades is expected to be strong on this item. Another concern is linked to the stability and jitter of the TTC clock, which is of course crucial for high-precision time-measuring devices: local clock regeneration on front-end modules (using existing devices) is mandatory, and the use of locally generated (synced) high-stability clock for special applications is also possible. Laboratory measurements on this point are being carried on at present.

A second piece of existing equipment present in the baseline design is the data-aquisition and trigger board TELL1, developed by LHCb [33]. This is a general-purpose 9U-size board with on board PC, ample buffer RAM memory, FPGAs and 4 Gigabit ethernet links, on which up to 4 custom mezzanine boards can be plugged. The data throughput capabilities are 24 Gb/s input and 4 Gb/s. This board is a good candidate for a common standard hardware on which the read-out of many NA62 sub-detectors can be based, to enforce common design. LHCb developed a 16 channel 10-bit 40 MHz FADC board and a 12 Gb/s digital optical receiver board. A third kind of mezzanine board has been developed by the NA62 Pisa group using the CERN-designed HPTDC chip [34]: 128 TDC channels per board are present, for a total of 512 channels on each TELL1 board; the design time resolution is 100 ps. The card is presently under test.

The TELL1-based TDC-board would perform digitisation and data storage, and in the case of sub-detectors participating in the L0 trigger it would also compute the L0 trigger primitives. A scheme is considered in which such primitives are asynchronously computed and timestamped to be transmitted from one board to the next via GbE links before reaching the central L0 trigger processor, which should re-synchronize and merge them with those from other sub-detectors to finally issue a L0 trigger if all conditions match in time.

The above solution in principle could be used for the read-out of (at least) all TDC-based sub-detectors, *e.g.* RICH, spectrometer, muon veto (excluding the Gigatracker because of engineering constraints). The present core cost estimate for this solution is about 5K CHF per TELL1 board and 600 CHF per mezzanine board (15 CHF/channel), excluding crates and cables; the entire system would be housed in 5 boards for the RICH and 16 for the entire

spectrometer.
A design for the readout of the CEDAR based on the TELL1 was also presented [35], for which 1 GHz FADC mezzanine cards would be developed.
The possibility of using the same TELL1 board with different mezzanine cards for the read-out of other (FADC-based) systems, is also being considered; the possibility of a new upgraded TELL1 board design increasing both computational power and data bandwidth is also followed; this might be a joint development interesting for LHC experiments upgrades or future HEP experiments.
The third area in which sinergy with solutions existing now or being developed for the future is very likely is that of the high-speed links connecting the front-end systems to the commercial PCs in the trigger/DAQ farm. Some commercial solutions were explored, which offer obvious advantages among which also the uniformity with the internal network fabric of the farm, *e.g.* Myrinet and 10-Gbit ethernet. Considering the fact that our application would be a very simple one in terms of the capabilities of the above links (practically requiring unidirectional point-to-point links with very trivial protocol), even where cost considerations are favourable, it turns out that - for the commercial solutions explored so far - the integration of the transceiver device on the custom side of the front-end electronics requires a non-negligible financial and engineering effort, which might be comparable to that of implementing a custom link.
The design of prototype custom high-speed links with PCI-Express interface, on-board latency memory and some computing power is underway in Roma Tor Vergata.
Due to the number of channels and – more importantly – the use of FADCs and the desire of avoiding zero suppression, the read-out and trigger system for the LKR calorimeter should probably be most conveniently based on a dedicated solution; one possible scheme for a parallel pipelined trigger processor, based on 40 MHz 10/12-bit FADCs, commercial FPGAs and memories mounted on 9U boards, acting as memory buffers for trigger latency and computation nodes for L0 primitives is being developed in Roma Tor Vergata The possibility of using a suitably modified version of the digitizers developed at CERN for the ALICE TPC is also being considered as an alternative. Given the sheer amount of data of a non-zero suppressed LKR calorimeter, a scheme in which the read-out of this sub-detector to PCs is not performed after L0, but only after L1 is also being considered: this would of course require that the front-end system for this device is capable of more powerful (L1) trigger computations, requiring full communication between the different boards over which the LKR data is subdivided.

While each sub-detector group is expected to contribute to the read-out of the system it is responsible for, the involvement in the trigger and data aquisition system is mostly going on in Pisa (general design, development of TDC board, TELL1 firmware), Perugia (L0 trigger for the RICH), Mainz (read-out of the straw spectrometer), CERN and Roma Tor Vergata (L0 trigger and read-out of the LKR calorimeter).
The implementation of the global online TDAQ farm will be a common effort of the experiment.

References

[1] V. Bolotov and V. Duk, Pion program for the future rare decay experiments, NA62 Internal Note, NA62-07-04.

[2] V. Cirigliano and I. Rosell, arXiv:0707.4464.

[3] A. Masiero, P. Paradisi and R. Petronzio, Phys. Rev. **D74** (2006) 011701.

[4] W.-M. Yao *et al.*, J. Phys. **G33** (2006) 1.

[5] L. Fiorini, PoS (HEP2005) 288 (2005).

[6] V. Kozhuharov, PoS (KAON) 049 (2007).

[7] F. Ambrosino *et al.*, arXiv:0707.4623.

[8] A. Ceccucci, Presentation of the P-326 proposal at the SPSC open session

[9] G. Anelli et al., "Proposal to Measure the Rare Decay $K^+ \to \pi^+ \nu\bar{\nu}$", CERN-SPSC-2005-013, SPSC-P-326, 11/06/2005.

[10] G. Cosmo, S. Giani, N. Hoimyr et al., "GEANT 4: an object-oriented toolkit for simulation in HEP",

[11] M. Scarpa, The P326 Gigatracker, Proceedings TIME05, Zurich, 3-5 October 2005.

[12] P. Riedler, "Pixel Detectors and Sensors - Gigatracker for P326" ELEC course, CERN 2005.

[13] N. Doble, Beam Working Group, Jan. 30th, 2007.

[14] P. Riedler, PhD thesis, Vienna 1998, CERN-THESIS-2000-002.

[15] M. Fiorini, F. Osmic, F. Petrucci and P. Riedler, NA62 Internal note 2007, in preparation.

[16] P. Riedler et al., Nucl. Instrum. Methods Phys. Res., A 572 (2007) 128-131.

[17] L. Gonella, et al., Total ionizing dose effects in 130-nm commercial CMOS technologies for HEP expeiments, Nucl. Instrum. Methods Phys. Res., A (2007), doi:10.1016/j.nima.2007.07.068.

[18] F. Gaccio and G. Cervelli, Radiation-induced edge effects in deep submicron CMOS transistors, IEEE Trans. Nucl. Sci., 52, No. 6, pp. 2413-2420, Dec. 2005.

[19] M. Kuhn, TS/CV/DC CFD-2006-06 (EDMS No. 732531).

[20] F. Anghinolfi, P. Jarron, F. Krummenacher, E. Usenko and M.C.S. Williams, NINO, An Ultra-Fast, Low Power, Front-End Amplifier Discriminator for the Time-of-Flight Detector in Alice Experiment.

[21] P. Moreira, et al., The GBT, a proposed Architecture for Multi-Gbps Data Transmission in High Energy Physics, Proceedings of TWEPP-07 Topical Workshop on Electronics for Particle Physics.

[22] Advanced or Micro Telecom Computing Architecture

[23] E. Ramberg et al., IEEE Trans. Nucl. Sci. **51** (2004) 2201

[24] A. Aloiso et al., Nucl. Instrum. Meth. A**482** (2002) 363

[25] The OPAL Collaboration, Nucl. Instrum. Meth. A**305** (1991) 275

[26] F. Ambrosino et al., arXiv 0711:3398

[27] V. Fanti et al., Nucl. Instrum. Meth. A**574** (2007) 433

[28] G. J. Feldman and R. D. Cousins, Phys. Rev. D **57** (1998) 3873.

[29] J. Conrad, O. Botner, A. Hallgren and C. Perez de los Heros, Phys. Rev. D **67**, 012002 (2003).

[30] A. Moraux, Cryogenics Control System - NA48 Integration Project, Presentation to the Collaboration Meeting, 12 July, 2007.

[31] M. Sozzi - A concept for the NA62 trigger and data aquisition - NA62 Internal Note NA62-07-03, November 2007.

[32] The Trigger, Timing and Control system for the LHC: `http://ttc.web.cern.ch/TTC/intro.html`.

[33] G. Haefeli *et al.* – "TELL1: specification for a common read out board for LHCb" – LHCb 2003-007 note, October 2003.

[34] HPTDC, J. Christiansen et al., Digital Microelectronics Group, CERN.

[35] B. Hallgren – "CEDAR readout using the LHCb TELL1 and 1 GHz ADC mezzanine board" – NA48 Note 05-02, May 2002.